UNIVERSITÀ
DEGLI STUDI
DI PADOVA

Università degli Studi di Padova

DIPARTIMENTO DI FISICA E ASTRONOMIA "GALILEO GALILEI"
Corso di Laurea Magistrale in Fisica

Confocal Microscopy with Sensorless Adaptive Optics

Candidato:
Luca Rizzotto
Matricola 1057839

Relatore:
Stefano Bonora

Correlatore:
Fabio Mammano

Anno Accademico 2013–2014

ACKNOWLEDGEMENTS

Vorrei ringraziare innanzitutto il mio relatore Dr. Stefano Bonora per avermi guidato e aiutato durante tutto il periodo di lavoro su questa tesi, e per aver messo a mia disposizione tutto il suo laboratorio dove ho avuto modo di sperimentare e imparare molte cose nuove ed interessanti. Ringrazio poi il mio correlatore Prof. Fabio Mammano, il Prof. Mario Bortolozzi e il mio controrelatore Prof. Matteo Pierno per la loro disponibilità ed il loro incoraggiamento a completare nel migliore dei modi questa tesi.

Ringrazio inoltre tutti i miei compagni e compagne di corso, nessuno escluso, coi quali ho condiviso molti momenti di studio, divertimento e crescita personale sotto tanti aspetti. In particolare ringrazio i miei compagni di laboratorio Federico, Damiano e Luca, coi quali ho scherzato ma anche lavorato sodo, e Alice che coi suoi preziosi appunti mi ha permesso di passare esami altrimenti impossibili.

Un grazie va poi ai miei amici di sempre, quelli con cui esco la sera a bere una birra, per le discussioni e lo svago indispensabili a rendere la vita universitaria un po' meno stressante.

Infine desidero ringraziare tutti i miei parenti e gli amici di famiglia, i miei nonni, i miei zii e i miei cugini, che sono stati sempre presenti nei momenti più importanti della mia vita.

A Giulia, il mio amore, mia instancabile sostenitrice.
A mia sorella Alice, persona importantissima, con la quale condivido i miei momenti di follia.
A Mamma e Papà, semplicemente insostituibili, per i quali un grazie non basta e a cui dedico questa tesi.

CONTENTS

INTRODUCTION

Every real optical system is in some way affected by aberrations, due to the single optical components and their alignment, or more frequently to the medium in which light waves propagate between the sample and the objective. These aberrations are a limit in the performances of the system, because they cause a loss of image quality.

The role of Adaptive Optics is to remove the aberrations from the system or at least to set them under a certain threshold, using wavefront correctors (which are in most of the cases deformable mirrors) modelled in such a way that the aberrated wavefront becomes almost plane passing through them. This idea was first proposed by H. W. Babcock in 1953 [1], but in those years it was impossible to make the technique practical (in 1970, P. Anderson used this idea in his science fiction novel *Tau Zero*). The first practical developments were done during the Cold War by the US military (the purpose was to track Soviet satellites), but only after 1990, with the development of computer technology, Adaptive Optics became possible and commonly used.

A conventional (linear) Adaptive Optics system consists of three principal subsystems [2,3,5]:

- a *wavefront sensor* to detect the optical disturbance;
- a *wavefront corrector*, usually a deformable (or adaptive) mirror, to correct the aberrations;
- a *control unit*, usually a computer, to decode the sensor information for the active mirror.

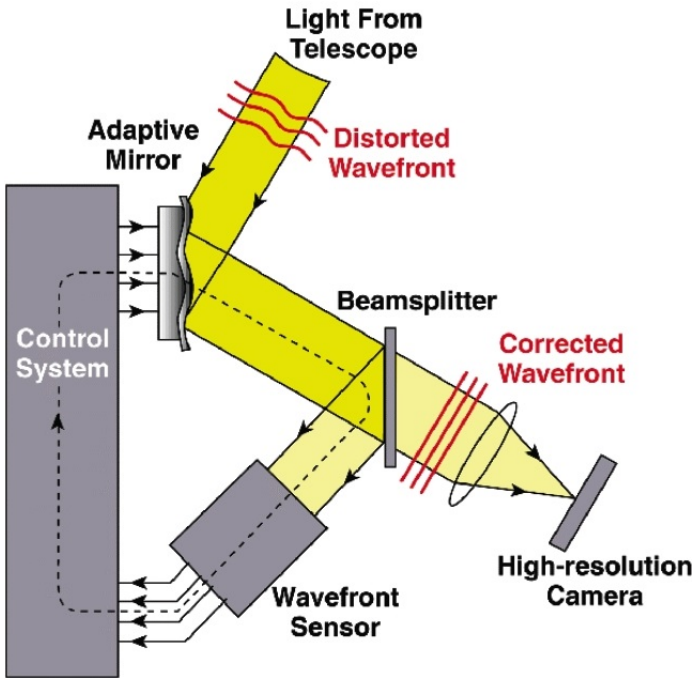

Figure 1: Scheme of a typical Adaptive Optics system with closed loop control

The first deformable mirrors were employed in astronomical telescopes in order to correct distortions of light wavefronts coming from stars and passing through atmospherical turbulences. These turbulences spread out light coming from point-like sources that are imaged as blurred blobs in the image plane. In this problem the source of aberration (i.e. the atmosphere) is rapidly time varying and the correction must be done in fractions of second. For this reason classical methods in Adaptive Optics includes another device called *wavefront sensor* employed to reconstruct directly the light wavefront in the system's pupil plane.

A very simple and commonly used *wavefront sensor* is the Shack-Hartmann *wavefront sensor*: it consists of an array of lenses of the same focal length. Each lens is focused onto a photon sensor, typically a CCD array. The local tilt of the wavefront across each lens can then be calculated from the position of the focal spot on the photon sensor. Any phase aberration can be approximated by a set of discrete tilts. All of these tilts can thus be measured in order to reconstruct the whole wavefront.

After reaching the *wavefront sensor*, the shape of the wavefront is known and sent to a computer or another control unit (e.g. FPGA) which immediately deforms in the appropriate way the deformable device, so it's possible to perform a real time correction.

Over the past few years lots of *deformable devices* and *wavefront sensors* have been developed, differing in technology, shape and price. This fact favoured the diffusion of Adaptive Optics in many other fields of research, concerning for example optical communications, laser focusing, beam shaping, optical tweezers and microscopy.

In optical microscopy [7], even working with *in-vivo* samples, aberrations are usually slowly time varying and this have allowed to develop alternative ways to correct light wavefronts *without* using a *wavefront sensor*, also known as *wavefront sensorless* methods. Algorithms employed in *sensorless* Adaptive Optics are based on parameters derivable from the image plane of the system and the correction process is appreciably slower than a *wavefront sensor* based one, but it has some advantages too. Firstly, without the *wavefront sensor* the complexity of the optical system is dramatically reduced (i.e. the system will be more compact and less expensive). Secondly, the most common *wavefront sensors* are intended to work with point-like sources, or at least with a guide star, and this is impossible to do in a microscope, where samples are closed to the objective and usually present a three-dimensional nature: this could lead to ambiguous *wavefront sensor* readings and thus to an incorrect aberration correction.

The fundamental element of *sensorless* Adaptive Optics, first conceived by Muller and Buffington in 1974 [13], is the concept of *Imaging Sharpness Metric*: this is a function dependent only on the irradiance of the light in the image plane, that reaches its global extremum (maximum or minimum) when the quality of the image reaches its maximum, that is, when all the aberrations are removed from the system.

A collection of aberrated images is then taken, with aberrations inducted by the deformable device, and the correct deformation (i.e. the

one which gives the best image quality) is found through an appropriate algorithm that aims to find the global extremum of the *Imaging Sharpness Metric*.

In the last few years, *wavefront sensorless* Adaptive Optics have been implemented in several different applications: widefield microscopy [30], confocal fluorescence and reflection microscopy [28,38], confocal scanning ophthalmoscopy [56], two-photon fluorescence microscopy [14,26,36,39,40,41], optical coherence tomography (OCT) with *in vivo* samples [37], maximisation of harmonic generation with ultra-intense laser pulses [35], intracavity aberration correction in lasers [42], optical tweezers[43] and coupling laser light into an optical fibre [44].

The purposes of this thesis are:

- to study some *imaging sharpness metrics* that can be found in literature, in order to understand their proprieties and their link with the possible mathematical representations of the aberrations;

- to find and use a good and fast algorithm to perform *sensorless* aberration correction;

- to compare our prototype of deformable lens piezoelectrically actuated with some deformable mirrors, to demonstrate that the deformable lens is a good *wavefront corrector*;

- to simplify the adaptive system, using deformable lenses that can be added to the system without using a beam splitter (which is needed when working with deformable mirrors) and without the *wavefront sensor*;

- to apply Adaptive Optics in a Confocal Fluorescence Microscope, using the *sensorless* techniques developed.

The method developed here can be applied in many other fields, including widefield microscopy, two-photons microscopy, optical coherence tomography (OCT) for retinal imaging and endoscopy. Furthermore, the piezoelectric deformable lens can be used together with a focus tunable deformable lens [58] in order to perform z-stack in thick samples, without moving the sample itself.

At the beginning of this work some simulations were performed (with MATLAB R2011b, *The MathWorks*) to simulate imaging process and *sensorless* aberration correction with different algorithms employing different *Imaging Sharpness Metrics* and different mathematical ways to describe the aberrations. After this first part, the same algorithms were tested in a simple experimental setup, ideated in particular to compare *sensorless* aberration correction with *closed loop* correction using a Shack-Hartmann *wavefront sensor*. Furthermore, several deformable devices were used and compared. In the last part, *sensorless* Adaptive Optics has been employed in a Confocal Fluorescence Microscope.

1

IMAGING SYSTEMS AND ABERRATIONS

1.1 SOURCES OF ABERRATIONS

In an ideal imaging system, according to geometrical optics, rays coming from a point-like source and passing through the system are focused to another point in its image plane. This means that a spherical wavefront emerging from a point-like source is phase-delayed from the system in such a way that after passing through it the wavefront emerges as a converging spherical wavefront with its center placed in the image plane of the system.

Aberrations are deviations from this ideal process: imperfections, misalignment or other factors in a real system can cause a non-spherical shape of the emerging wavefront, and thus a point-like source isn't imaged as a point on the image plane, but rather as a blob, whose dimension and shape could vary with the magnitude and nature of the aberration.

When imaging an extended object, aberrations manifest themselves as a blur in the image of the object, so the imaging process causes a loss of resolution and information.

In astronomical ground-based telescopes aberrations arises from atmospherical turbulence, as mentioned in the introduction of this thesis. Though space telescopes don't have this problem, actually their objective diameters are strongly limited (e.g. Hubble Space Telescope has a maximum diameter of 2.4 meters), and big ground-based telescopes can reach better resolutions than space ones if accountered with Adaptive Optics.

In optical microscopy the main sources of aberration are clearly different from the astronomical case and can be summarized as follows [7,21]:

- refractive index mismatch in media between the sample and the objective lens;
- sample induced aberrations due to structures with different refractive index within the sample;
- sample holder aberrations due to imperfections on the coverslip or another structure that holds the sample;
- Imperfections in the optical system such as misalignment or imperfections in the components of the system.

In the following paragraphs of this chapter we will see how to represent in a correct mathematical way this aberrations, that is the first important step to remove them from the system.

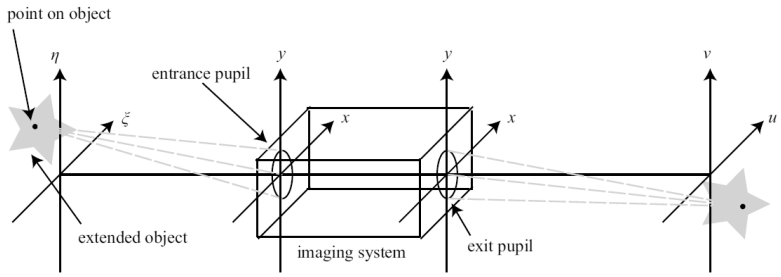

Figure 2: Main features of a simple imaging system.

Aberrations can be expressed mathematically as a *wavefront function* $W(x,y)$ measured in waves (or an optical phase $\Phi(x,y)$ measured in radians, $\Phi(x,y) = 2\pi W(x,y)$) introduced into the pupil of the objective lens. $W(x,y)$ represents the optical path difference between the physical wavefront of the system and a reference sphere or plane (i.e. the wavefront of the same system, but aberration-free).

The complex *Pupil Function* of the system is given by [8,30]

$$\mathcal{P}(r,\theta) = P(r)e^{i\Phi(x,y)} \tag{1}$$

where $P(r) = 1$ in the unit circle, 0 elsewhere.

In an optical system working with a spatially incoherent light, the *image irradiance* $I(u,v)$ can be described by the convolution of the *object irradiance* $I_0(\eta,\xi)$ with the *point spread function* (PSF) $|h(u,v)|^2$ of the system [8,30]:

$$I(u,v) = \iint |h(u-\eta, v-\xi)|^2 I_0(\eta,\xi)\,d\eta\,d\xi = |h(u,v)|^2 \otimes I_0(u,v) \tag{2}$$

The PSF describes the response of an incoherent imaging system to a point source, and it's mathematically equivalent to the modulus squared of the *amplitude point spread function* $h(u,v)$. Using the scalar approximation to diffraction theory, the field in the focus of the objective lens can be simply expressed as the Fourier trasform of the pupil function, thus we can write [8]:

$$\begin{aligned} h(u,v) &= \frac{1}{\lambda z}\iint \mathcal{P}(x,y)e^{-i\frac{2\pi}{\lambda z}(ux+vy)}\,dx\,dy \\ &= \frac{1}{\lambda z}\mathcal{F}(\mathcal{P}(x,y))_{f_x=\frac{u}{\lambda z}, f_y=\frac{v}{\lambda z}} \end{aligned} \tag{3}$$

where z is the image distance and $\mathcal{F}$ is the Fourier transform operation.

With these formulas, computer simulations of the imaging process with a chosen aberration is quite simple and it's described in the next chapter. In the next paragraph we will introduce some smart ways to represent an aberrated wavefront $W(x,y)$.

If we want to accurately describe what kind of aberrations affect our system, it's useful to express the shape of the wavefront as a complete and orthogonal series of polynomials. There is more than a way to express this series, everyone with different utilities and mathematical properties.

In the following paragraphs we will introduce two cbases that can be used to represent aberrations (i.e. Zernike polynomials and Lukosz polynomials), exploring their definitions and properties.

1.3.1 *Zernike polynomials*

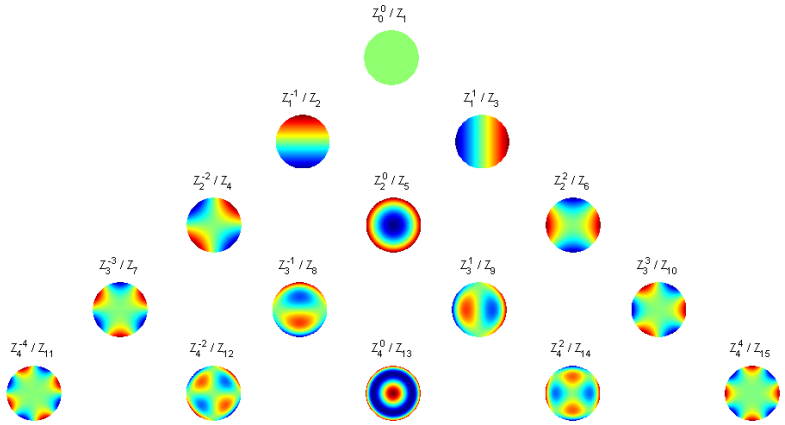

Figure 3: First 15 Zernike polynomials (dual indexation is shown).

Zernike polynomials [9] are a set of functions that are orthogonal on the unit circle, commonly used to describe wavefronts in optical systems with circular aperture. Calling these polynomials $Z_i(r,\theta)$ (or $Z_n^m(r,\theta)$, for the relation between the two notations see Figure 3). In polar coordinates the function $W(r,\theta)$ describing the wavefront can be expressed as

$$W(r,\theta) = \sum_{i=1}^{\infty} c_i Z_i(r,\theta) \tag{4}$$

Using Noll's normalization for Zernike polynomials [10], each $Z_i(r,\theta)$ has a mean value of zero and a variance of one, and they can be expressed as:

$$Z_n^m(r,\theta) = \begin{cases} \sqrt{n+1}R_n^m(r)\mathrm{sqrt2cos}(m\theta) & \text{for } m > 0 \\ \sqrt{n+1}R_n^{|m|}(r)\mathrm{sqrt2sin}(|m|\theta) & \text{for } m < 0 \\ \sqrt{n+1}R_n^0(r) & \text{for } m = 0 \end{cases}$$

where n, m are integers satisfying $|m| \leqslant n$ and $(m-n) = \text{even}$. $R_n^m(r)$ are the radial components of the polynomials defined as:

$$R_n^m(r) = \sum_{k=0}^{\frac{n-m}{2}} \frac{(-1)^k (n-k)!}{k![\frac{n+m}{2}-k]![\frac{n-m}{2}-k]!} r^{(n-2k)}$$

The orthogonality law satisfied by Zernike polynomials is given by:

$$\frac{1}{\pi}\iint P(r) Z_{i1} Z_{i2} r dr d\theta = \delta_{i1,i2} \tag{5}$$

where $\delta_{i1,i2}$ is the Kronecker delta and $P(r)$ ($= 1$ in the unit circle, 0 elsewhere) is the *pupil function*.

A remarkable consequence of this orthogonality law is that using Zernike polynomials the total wavefront variance can be calculated simply as [8]:

$$\begin{aligned}\sigma^2 &= \frac{1}{\pi}\iint P(r)[W(r,\theta)-\overline{W}]^2 r\,dr\,d\theta \\ &= \frac{1}{\pi}\iint P(r)[\sum_{i=2}^{\infty} c_i Z_i(r,\theta)]^2 r\,dr\,d\theta \\ &= \sum_{i=2}^{\infty} c_i^2\end{aligned} \tag{6}$$

where c_i are the same coefficients of Eq.4.

Note that the sum in the above equation begins at $i = 2$, because $\overline{W}$, that represents the mean value of $W(r,\theta)$, matches with the piston term (i.e., $i = 1$) in Eq.4.

We have found that the wavefront variance can be simply estimated from Zernike coefficients, and this can be used to estimate another interesting value called the *Strehl intensity* S of the wavefront. This is a quantity that can be used as a measure of the quality of optical image formation, and for *small* aberrations it's well known [54] that it doesn't depend on the form of the aberration, but only on its variance:

$$S \simeq 1-\sigma^2 = 1-\sum_{i=2}^{\infty} c_i^2 \tag{7}$$

From these considerations we can conclude that Zernike polynomials have got good properties to describe systems affected by small aberrations, giving a simple way to evaluate the *Sthrel intensity* of the wavefront.

1.3.2 *Lukosz polynomials*

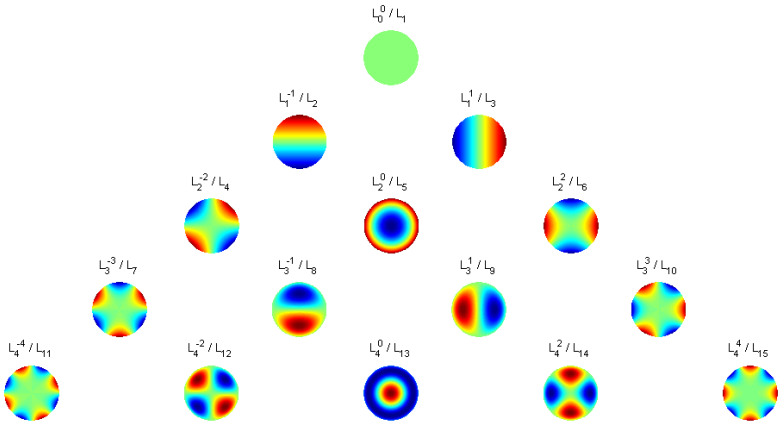

Figure 4: First 15 Lukosz polynomials (dual indexation is shown).

An alternative basis of polynomials that can be used to represent wavefront aberrations in optical systems with circular aperture is the

basis of Lukosz polynomials [11,12]. Calling them $L_i(r,\theta)$ we can write $W(r,\theta)$ as:

$$W(r,\theta) = \sum_{i=1}^{\infty} a_i L_i(r,\theta) \tag{8}$$

Like Zernike functions, Lukosz functions have two possible indexations (totally identical to Zernike ones) and they are expressed as the product of a radial function and an azimuthal function [16,30]:

$$L_n^m(r,\theta) = B_n^m(r) \times \begin{cases} \cos(m\theta) & \text{for } m \geqslant 0 \\ \sin(m\theta) & \text{for } m < 0 \end{cases}$$

with

$$B_n^m(r) = \begin{cases} \frac{1}{2\sqrt{n}}(R_n^0(r) - R_{n-2}^0(r)) & \text{for } n \neq m = 0 \\ \frac{1}{\sqrt{2n}}(R_n^m(r) - R_{n-2}^m(r)) & \text{for } n \neq m \neq 0 \\ \frac{1}{\sqrt{n}} R_n^n(r) & \text{for } n = m \neq 0 \\ 1 & \text{for } n = m = 0 \end{cases}$$

where n, m and $R_n^m(r)$ satisfy the same conditions of the Zernike case.

The orthogonality law satisfied by these polynomials is rather different from Zernike one (i.e. Eq.5), and this fact will be important in the results of this thesis. For simplicity, in the following equations we won't take into account the first 3 Lukosz polynomials (i.e. piston, tip and tilt) because they don't have effect on the image quality. The normalization of $B_n^m(r)$ in the previous equations permits to write the orthogonality law as [16,30]:

$$\frac{1}{\pi} \iint P(r)(\nabla L_{i1}) \cdot (\nabla L_{i2}) r dr d\theta = \delta_{i1,i2} \tag{9}$$

An interesting property of these polynomials is that they can be used to give a simple expression for the *rms spot radius* in image plane, defined as [12,16,55]:

$$\rho_{rms}^2 = \langle (\Delta x)^2 + (\Delta y)^2 \rangle \tag{10}$$

where $\Delta x, \Delta y$ are the so-called *transverse aberrations*, that are equal to

$$\Delta x = R\lambda \frac{\partial W(x,y)}{\partial x}$$
$$\Delta y = R\lambda \frac{\partial W(x,y)}{\partial y}$$

where λ is the wavelength, R is the radius of the reference sphere.

From Eqs.8-9 we can show that ρ_{rms}^2 is proportional to the sum of the squares of the Lukosz coefficients [12,16,30,55]:

$$\begin{aligned} \rho_{rms}^2 &= \langle (\Delta x)^2 + (\Delta y)^2 \rangle \\ &= (R\lambda)^2 \langle \left(\frac{\partial W(x,y)}{\partial x} \right)^2 + \left(\frac{\partial W(x,y)}{\partial y} \right)^2 \rangle \\ &= (R\lambda)^2 \langle |\nabla W(x,y)|^2 \rangle \\ &= (R\lambda)^2 \langle \nabla W(x,y) \cdot \nabla W(x,y) \rangle \\ &= (R\lambda)^2 \sum_{i=4}^{\infty} \sum_{j=4}^{\infty} a_i a_j \langle \nabla L_{i1}(x,y) \cdot \nabla L_{i2}(x,y) \rangle \end{aligned}$$

$$= \left(\frac{\lambda}{2\pi NA}\right)^2 \sum_{i=4}^{\infty}\sum_{j=4}^{\infty} a_i a_j \frac{1}{\pi}\iint P(r)\nabla L_{i1}(r,\theta)\cdot\nabla L_{i2}(r,\theta) r\,dr\,d\theta$$

In the last step, a change from Cartesian to polar coordinates has been performed. Now, using Eq.9 we finally find:

$$\rho^2_{rms} = \left(\frac{\lambda}{2\pi NA}\right)^2 \sum_{i=4}^{\infty} a_i^2 \tag{11}$$

where NA is the numerical aperture of the wave.

This property of Lukosz polynomials makes them a good basis to study systems affected by *large* aberrations [31]. In order to better understand this property, it's useful to take a geometrical optics view of the imaging process.

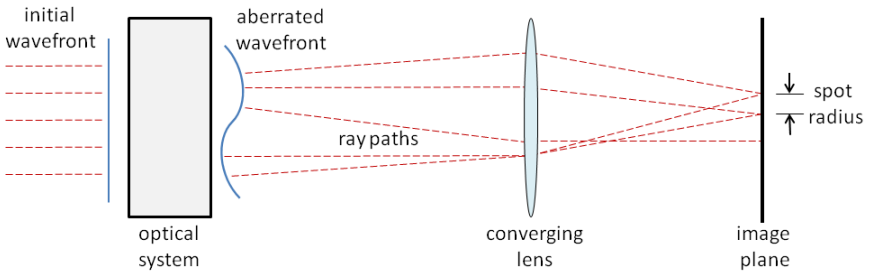

Figure 5: Paths of geometrical rays in presence of aberrations

Taking into account Figure 5 we see that, if the aberration is large, the spot radius in image plane (and so its rms) will be big enough to neglect diffraction effects in the study of the aberration. Furthermore the directions of the geometrical rays are described by the partial derivatives of the wavefront function $W(x,y)$, and this is why the equations written above includes them.

1.4 IMAGING SHARPNESS METRICS

In describing an imaging system, it's very useful to have an efficient way to measure the image quality. Well known optical quality criteria [21,55] are based on quantities derived directly from the wavefront, such as the PSF or the OTF (i.e. Optical Transfer Function: it describes how the spatial frequencies are transmitted from the object plane to the image plane and it can be found by Fourier transforming the PSF). However this kind of approach it's not possible if the wavefront is not accessible directly, or if a *wavefront sensor* isn't used.

A possible alternative is to find an *imaging sharpness metric* that is based on parameters extractable only from the image plane and gives a measurement of the quality of the image on the form of a scalar. This metric must have a well defined global extremum (maximum or minimum point) in correspondence of the best image quality (i.e. when all the aberrations are eliminated from the system), and it must vary quite rapidly beyond this extremum with monotonicity.

In literature several *imaging sharpness metrics* can be found [13,19,30]. Two *optimisation metrics* has already been introduced in the previous paragraphs: they are the *Strehl intensity* and the *rms spot radius*. Using

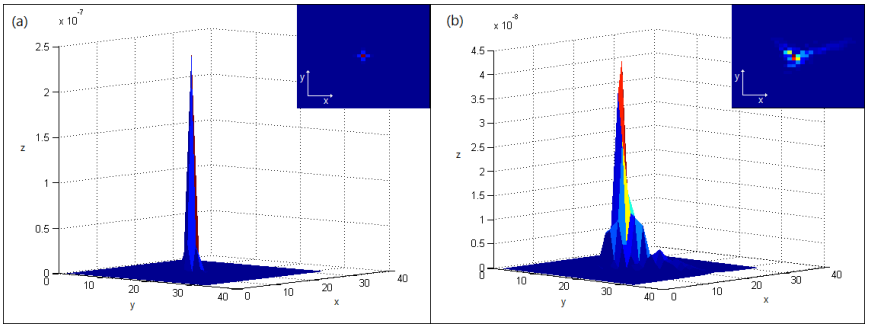

Figure 6: Simulated PSF in the image plane (a) in an aberration-free system and (b) in a system with aberrations (0.32 waves rms of the first 11 Zernike polynomials without piston, tip and tilt). Pupil diameter = 2.5 cm, λ = 633 nm, image distance $z = 25$ cm.

the appropriate basis of polynomials we have seen that they can be rewritten in a simple way, where the single modes describing the aberrations are independent each other. Thus, aberration correction can be performed one mode at a time, being the metric a N-dimensional function (with N = number of modes to be corrected) with a well defined global extremum (a maximum for the *Strehl intensity*, a minimum for the *rms spot radius*). Nevertheless, they work only with *point-like samples*, so they can't be considered *imaging sharpness metrics*, and we have also seen that these two quantities are good to describe only small and large aberrations respectively.

In the next paragraphs two *imaging sharpness metrics* will be introduced, one based on the irradiance in the image plane and one on its Fourier transform, which can be used with *extended samples*. As we will see in the next chapters of this thesis these two metrics were used and compared in simulated and experimental aberration corrections.

1.4.1 *Maréchal Criterion*

Once the *Strehl Intensity* is known, it's possible to estimate the quality of our optical system using the *Maréchal Criterion*. This criterion states that a system can be considered well corrected if

$$S \geqslant 0.8$$

This means that if the rms deviation from the flat wavefront is < 0.08 waves rms $\left(= \frac{\lambda}{14}\right)$, the wavefront can be considered flat.

1.4.2 *Irradiance Squared Metric*

This metric was first proposed by R. A. Muller and A. Buffington in 1974 [13], with a series of other similar metrics based on the irradiance in the image plane, for astronomical images atmospherically degraded. The *Irradiance Squared Metric* (IQ) is defined as:

$$IQ = \iint I(x,y)^2 dxdy \tag{12}$$

where $I(x,y)$ is the irradiance, as mentioned above.

In the original article is demonstrated that this metric is maximized when the wavefront distortions are zero, and this is a global max-

imum as requested for a good metric. Taking into account all the image plane, this metric is useful for large extended objects, while other metrics presented in the article by Muller and Buffington are intended to work with point-like sources, and that's not our case. Other metrics defined in the same article that we will compare with IQ metric in the simulations are

$$S_\beta = \iint I(x,y)^\beta \, dxdy, \qquad \beta = 3,4$$
$$S_5 = \iint I(x,y) \cdot \ln[I(x,y)] dxdy$$
$$S_6 = \iint I(x,y) \cdot (x^2 + y^2) dxdy$$

1.4.3 *Spectral Density Metric*

The *Spectral Density Metric* (SD) was proposed by D. Débarre, M. J. Booth and T. Wilson in 2007 [30]. This metric is based upon the low spacial frequency content of the image, but leads to correction for all spatial frequencies, and it's ideal for incoherent imaging systems. SD metric is defined as

$$SD = \int_{\xi=0}^{2\pi} \int_{m=M_1}^{M_2} S_J(m) m dm d\xi \tag{13}$$

where $S_J(m)$ is called *spectral density* of the image and can be calculated as follows. Applying the *Convolution Theorem* on Eq.2 we have

$$I(\mathbf{x}) = |h(\mathbf{x})|^2 \otimes I_0(\mathbf{x})$$
$$\mathcal{F}(I(\mathbf{x})) = \mathcal{F}(|h(\mathbf{x})|^2) \cdot \mathcal{F}(I_0(\mathbf{x}))$$

Multiplying the last equation by its complex conjugate and calling $S_J(\mathbf{m}) = |\mathcal{F}(I(\mathbf{x}))|^2$, $S_T(\mathbf{m}) = |\mathcal{F}(I_0(\mathbf{x}))|^2$ and $H(\mathbf{m}) = \mathcal{F}(|h(\mathbf{x})|^2)$ (i.e. the OTF), where $\mathbf{m}$ is the spatial frequency vector, we finally obtain

$$S_J(\mathbf{m}) = |H(\mathbf{m})|^2 \cdot S_T(\mathbf{m}) \tag{14}$$

SD metric defined in Eq.13 reaches its maximum in an aberration-free system, as for the IQ metric [30].

SD metric has got some other interesting properties. First of all, as it can be seen from its definition, the spatial frequencies considered in the integration can be selected. The bigger is the range of frequencies considered, the larger the aberration that can be corrected with this metric, as we will see in the simulations. It's better not to consider frequencies close to zero, because they are only weakly affected by aberrations and do not therefore contribute significantly to changes in the SD metric [16]. Furthermore, it's worth pointing out that the Fourier Trasform of the irradiance, evaluated at the origin, is equal to the mean value of the irradiance in the image plane:

$$\mathcal{F}(I(\mathbf{x}))|_{\mathbf{x}=0} =< I(\mathbf{x}) >$$

So excluding $\mathcal{F}(I(\mathbf{x}))|_{\mathbf{x}=0}$ from the SD metric evaluation makes the metric less sensitive to variations in the light intensity from the sample (which means variations in $< I(\mathbf{x}) >$).

Secondly, if we consider only low spatial frequencies and samples without noticeable periodicity in a predominant direction, Débarre, Booth and Wilson demonstrated [30] that SD metric can be simply expressed as a series of Lukosz coefficients, i.e.

$$SD \approx \frac{1}{q_1 + q_2 \sum_{i=4}^{\infty} a_i^2} \tag{15}$$

where q_1 and q_2 are two positive quantities which only depends on (M_1, M_2), so they can be considered constants once the spatial frequencies range is fixed.

Taking the inverse of this relation, the metric becomes a paraboloid in N-dimensions (being N the number of Lukosz modes considered), with a global minimum in correspondence of the aberration-free condition, and each mode can be corrected independently from the others:

$$SD^{-1} \approx q_1 + q_2 \sum_{i=4}^{\infty} a_i^2 \tag{16}$$

This fact is very important to speed up and simplify the aberration correction process, as we will show in the next chapters.

1.4.4 *Link between SD and IQ metrics*

An interesting thing to note is that, from *Parseval Theorem*, we can relate the IQ metric with the SD metric. Furthermore from this relation it can be seen that the IQ metric is a particular case of the SD metric [30].

Indeed a special case of *Parseval Theorem* states that if $g(x, y)$ is a square integrable complex-valued function on $\mathbb{R}$ with its first and second derivatives absolutely convergent, then

$$\int_{-\infty}^{+\infty}\int_{-\infty}^{+\infty} |g(x,y)|^2 dx dy = \int_{-\infty}^{+\infty}\int_{-\infty}^{+\infty} |G(f_x, f_y)|^2 df_x df_y$$

where $G(f_x, f_y) = \mathcal{F}(g(x, y))$.

In our case we can use this theorem to write

$$\int_{-\infty}^{+\infty}\int_{-\infty}^{+\infty} |I(x,y)|^2 dx dy = \int_{\xi=0}^{2\pi}\int_{m=0}^{+\infty} S_J(m) m dm d\xi \tag{17}$$

Eq.17 shows that IQ metric is equivalent to SD metric integrated over all the spatial frequencies from 0 to $+\infty$.

1.5 OPTIMISATION ALGORITHMS

After choosing a basis of polynomials to represent the aberrations and an *imaging sharpness metric*, we need an algorithm to find the global extremum of the metric and so to have all the informations required to perform a good aberration correction. Some considerations by D. Débarre, M. J. Booth and T. Wilson leads to the *Modes Correction Algorithm* [30], that is demonstrated to be good only under some conditions. A classical way to proceed is instead to use a search

algorithm to find the global extremum of the metric [17]. Both types of algorithms are presented in the next two paragraphs.

1.5.1 *Modes Correction Algorithm*

We've seen in Eq.16 that using Lukosz polynomials it's possible to express the SD metric as a paraboloid in N-dimensions, being N the number of Lukosz Modes used to describe the aberration (from now on, we will use for simplicity the name "SD metric" referring to the quantity defined in Eq.16, i.e. the reciprocal of the *spectral density*).
In practice, this means that we can perform an aberration correction for each Lukosz Mode independently [30]: for each dimension we must find the vertex of a parabola, which value represents the correction that must be applied to the deformable device to cancel out the aberration due to that Lukosz mode. This way to proceed will take a minimum of three points for each mode, i.e. $2N + 1$ image evaluations (being one of the images common for all the modes, if we take the corresponding coefficient equal to zero), to perform a complete aberration correction.

Let's outline this procedure:

1. Evaluate SD_0 = SD metric value of the image with the deformable device relaxed. This value will be taken only once and it will be used in the correction of all the modes (see Figure 7 (a)).

2. Select a *bias* b, i.e. a value that will be subtracted and summed to the coefficients of each mode. This value must be selected taking into account the size of the aberration that affects the system and, for the experimental application, the limits of the deformable device.

3. Choose a number N of modes to correct. This number is limited by the ability of the deformable device to reproduce high order modes.

4. Excluding piston, tip and tilt, that don't contribute to the aberration, reproduce with the deformable device the first Lukosz mode L_4 with a coefficient $-b$ (see Figure 7 (b)).
   Take SD_- = SD metric value of the resulting image.

5. Reproduce the same Lukosz mode L_4, this time with a coefficient $+b$ (see Figure 7 (c)).
   Take SD_+ = SD metric value of the resulting image.

6. We have now three values of the SD metric functions, that can be fitted with a parabola to find the value a_{corr} of the coefficient of L_4 that represents the vertex of the parabola (see Figure 7 (d)).

   It can also be estimated as:

$$a_{corr} = \frac{-b(SD_+ - SD_-)}{2SD_+ - 4SD_0 + 2SD_-} \tag{18}$$

7. Reproducing the Lukosz mode L_4 with the coefficient a_{corr} with the deformable device, the aberration due to this Lukosz mode will be removed from the system.

8 Applying the same procedure for all the other modes $L_5, L_6, ...L_N$ starting from the fourth point of this list, we can remove all the aberrations from the system.

Obviously N must be big enough to represent the real aberration of the system in a good way. The deformable devices we will use in the experimental part of this thesis are in able to reproduce $N = 15 \div 21$ Lukosz and Zernike modes.

Although this procedure is theoretically correct only for the SD metric and only expanding the aberration using Lukosz polynomials, it can't be excluded that it works in practice, within certain limits, also with Zernike polynomials or with the IQ metric (Eq.17 shows that IQ and SD metrics are strictly related). For the IQ metric the fitting function won't be a parabola, we can try to apply this method evaluating more metric values for each mode and fitting them with a polynomial of degree 3 or 4.

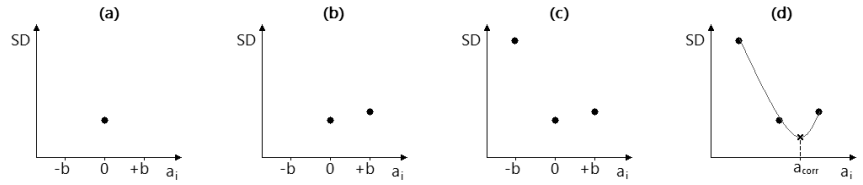

Figure 7: Steps of the Modes Correction Algorithm, where a_i is the coefficient of the i-th Lukosz mode L_i, SD the *Spectral Density metric.*

It is worth trying this alternatives because the *Modes Correction Algorithm* allows to do *sensorless* aberration correction faster than other algorithms commonly used in this field, such as the *Nelder-Mead Simplex Algorithm* that we will introduce in the next paragraph.

1.5.2 *Nelder-Mead Simplex Algorithm*

The *Nelder-Mead Algorithm* [17] (or Simplex Search Algorithm, Nelder and Mead, 1965) is one of the best known algorithms for multidimensional unconstrained optimization, which attempts to minimize a scalar-valued nonlinear function of N variables using only function values, without any derivative information: it can be used in problems where the function values are uncertain or subject to noise, even with discontinuous functions.

In order to define a Nelder-Mead method, we must specify 4 parameters (the values presented here are the standard ones):

- reflection $\rho = 1$,
- expansion $\chi = 2$,
- contraction $\gamma = \frac{1}{2}$,
- shrinkage $\sigma = \frac{1}{2}$.

At the beginning of the kth interation ($k \geqslant 0$) a non-degenerate simplex Δ_k with $n + 1$ vertices $x_i \in \mathbb{R}^n$ is given (e.g., in 2 dimensions a simplex is a triangle, in 3 a tetrahedron and so on). The kth interation by ordering and labelling these vertices $x_1^{(k)}$,...,$x_{n+1}^{(k)}$ such that

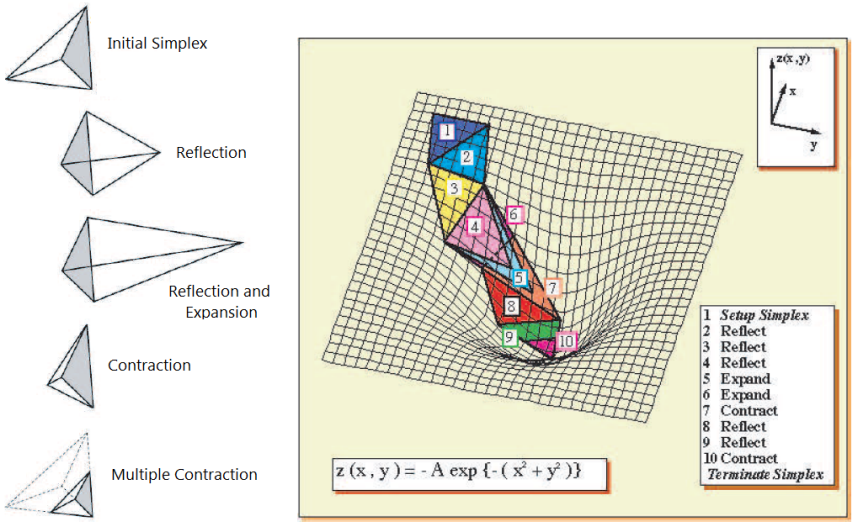

Figure 8: Operations through which the simplex moves within the search space

$$f_1^{(k)} \leqslant f_2^{(k)} \leqslant \ldots \leqslant f_{n+1}^{(k)}$$

with $f_i^{(k)} = f(x_i)^{(k)}$.

The kth iteration generates a set of $n+1$ vertices that define a new different simplex for the next iteration, $\Delta_{k+1} \neq \Delta_k$. Because we want to *minimize* f, we refer to $x_1^{(k)}$ as the *best* point, to $x_{n+1}^{(k)}$ as the *worst* point and to $x_n^{(k)}$ as the *next-worst* point. Similarly, we refer to f_1^k as the *best* function value and so on.

One iteration of the *Nelder-Mead Algorithm* can be performed as follows.

1 **Order**
Order the $n+1$ vertices to satisfy $f_1 \leqslant f_2 \leqslant \ldots \leqslant f_{n+1}$ using the tie-breaking rules given below.

2 **Reflect**
Compute the *reflection point* x_r from

$$x_r = \bar{x} + \rho(\bar{x} - x_{n+1}) = (1+\rho)\bar{x} - \rho x_{n+1}$$

where $\bar{x} = \sum_{i=1}^{n} \frac{x_i}{n}$. If $f_1 \leqslant f_r < f_n$ accept x_r and terminate the iteration.

3 **Expand**
If $f_r < f_1$ calculate the *expansion point* x_e as

$$x_e = \bar{x} + \chi(x_r - \bar{x}) = \bar{x} + \rho\chi(\bar{x} - x_{n+1}) = (1+\rho\chi)\bar{x} - \rho\chi x_{n+1}$$

and evaluate $f_e = f(x_e)$. If $f_e < f_r$ accept x_e and terminate the iteration, otherwise accept x_r and terminate the iteration.

4 **Contract**
If $f_r \geqslant f_n$ perform a contraction between $\bar{x}$ and the better between x_{n+1} and x_r.

a) **Outside**
If $f_n \leqslant f_r < f_{n+1}$ perform an outside contraction, calculating

$$x_c = \bar{x} + \gamma(x_r - \bar{x}) = \bar{x} + \gamma\rho(\bar{x} - x_{n+1}) = (1+\rho\gamma)\bar{x} - \rho\gamma x_{n+1}$$

and evaluate $f_c = f(x_c)$. If $f_c < f_{n+1}$ accept x_c and terminate the iteration, otherwise go to step 5.

b) **Inside**
If $f_r \geqslant f_{n+1}$ perform an inside contraction, calculating

$$x_{cc} = \bar{x} - \gamma(\bar{x} - x_{n+1}) = (1-\gamma)\bar{x} + \gamma x_{n+1}$$

and evaluate $f_{cc} = f(x_{cc})$. if $f_{cc} < f_{n+1}$ accept x_{cc} and terminate the iteration, otherwise go to step 5.

5 **Perform a shrink step**
Evaluate f at the n points $v_i = x_1 + \sigma(x_i - x_1)$; $i = 2, ..., n+1$.
The vertices of the simplex at the next iteration will be

$$x_1, v_2, ..., v_{n+1}$$

The main virtue of this algorithm is that if the problem is well defined (i.e. if the function f is a good metric) we are sure to find the right solution of it. The big limit is that *Nelder-Mead Algorithm* takes hundreds of iterations to converge to a good solution, and the time taken to perform an aberration correction is too much longer than that implied with the *Modes Correction Algorithm*: we'll see this fact in the simulations.

1.6 OPTIMUM MODES

Analytic functions such as Zernike and Lukosz polynomials are very useful to represent aberrations in an optical system. Nevertheless such functions can't be perfectly reproduced by real deformable devices and the approximation errors can affect the aberration correction process. These errors might become large if the number of actuators of the deformable device is small, and this can be the case for some of the devices we will use.
Starting from the *influence matrix* of the deformable device, it's possible to derive alternative modal basis sets which are the natural *optimum modes* of the device [16]. These *optimum modes* are perfectly reproducible by the device, thus avoiding the approximation errors.

1.6.1 *Influence Matrix*

The *influence matrix* $\mathbf{A}$ of a deformable device describes how the actuator commands affect its surface, as measured by a *wavefront sensor* [5]. It is usually determined at run time by setting one actuator at a time to a determined value (e.g. one unit) and then measuring the results with the *wavefront sensor*: each measure forms a column in the *influence matrix*. Calling $\mathbf{c}$ the *actuator commands vector* composed of n elements, and $\mathbf{\Phi}$ the *wavefront vector* containing the m wavefront measurements, $\mathbf{A}$ can be thought of as an $m \times n$ matrix which transforms $\mathbf{c}$ in $\mathbf{\Phi}$, that is:

$$\mathbf{\Phi} = \mathbf{A}\mathbf{c}$$

Once the *influence matrix* is known, we can take its inverse to determine the *actuator commands vector* $\mathbf{c}$ to be sent to the deformable device in order to obtain a desired *wavefront vector* $\mathbf{\Phi}$:

$$\mathbf{c} = \mathbf{A}^{-1}\mathbf{\Phi}$$

1.6.2 *Optimum Modes O1 and O2*

As previously mentioned, it's possible to derive the natural *optimum modes* of a deformable device from its *influence matrix*. This can be done using a *singular value decomposition* (SVD) algorithm. The derivation presented here is due to B. Wang and M. J. Booth, 2009. Applying the SVD algorithm to an $m \times n$ *influence matrix* $\mathbf{A}$, we obtain

$$\mathbf{A} = \mathbf{U}\mathbf{W}\mathbf{V}^{\mathbf{T}} \tag{19}$$

where $\mathbf{U}$ is an $m \times m$ matrix whose columns represents the orthogonal *optimum modes*, $\mathbf{W}$ is an $m \times n$ diagonal matrix with non-negative real numbers on the diagonal called *singular values* and $\mathbf{V}^{\mathbf{T}}$ is the transpose of an $n \times n$ unitary matrix that permits the conversion between $\mathbf{A}$ and $\mathbf{U}$. Using the modes contained in $\mathbf{U}$ we can express our *wavefront vector* $\mathbf{\Phi}$ simply as:

$$\mathbf{\Phi} = \mathbf{U}\mathbf{a}$$

where $\mathbf{a}$ is a vector whose m elements are the coefficients of the *optimum modes*. They are related to the *actuator commands vector* by

$$\mathbf{a} = \mathbf{W}\mathbf{V}^{\mathbf{T}}\mathbf{c}$$

Let's call u_i, u_j respectively the i-th and j-th columns of matrix $\mathbf{U}$. The orthogonality law used by the SVD algorithm is the same of Eq.5:

$$\langle u_i, u_j \rangle_1 = \frac{1}{\pi}\iint P(r) u_i u_j r dr d\theta = \delta_{i,j} \tag{20}$$

where where $\delta_{i,j}$ is the Kronecker delta.

We will refer to the *optimum modes* satisfying Eq.19 as O1 modes. If we want to express Eq.16 with these new modes, we need a modified algorithm which gives us a set of *optimum modes* that satisfy an orthogonality of the Eq.9 type, that is [16,30]

$$\langle u_i, u_j \rangle_2 = \frac{1}{\pi}\iint P(r)(\nabla u_i)\cdot(\nabla u_j) r dr d\theta = \delta_{i,j} \tag{21}$$

We will refer to the *optimum modes* satisfying Eq.20 as O2 modes. Let's see how the algorithm must be modified. Eq.19 and Eq.20 are related as follows

$$\langle u_i, u_j \rangle_2 = \langle \frac{\partial u_i}{\partial x}, \frac{\partial u_j}{\partial x} \rangle_1 + \langle \frac{\partial u_i}{\partial y}, \frac{\partial u_j}{\partial y} \rangle_1$$

If $\frac{\partial u_i}{\partial x}$ and $\frac{\partial u_i}{\partial y}$ are concatenated to give a single vector u_i' of twice the length, the previous equation can be rewritten as

$$\langle u_i, u_j \rangle_2 = \langle u_i', u_j' \rangle_1$$

From these considerations follows that we must take partial derivatives of the columns of the matrix $\mathbf{A}$ before applying the SVD algorithm. We thus obtain a $2m \times n$ matrix $\mathbf{A}'$:

$$\mathbf{A} = \begin{pmatrix} p_{11} & \dots & p_{1n} \\ p_{21} & \dots & p_{2n} \\ \vdots & \vdots & \vdots \\ p_{m1} & \dots & p_{mn} \end{pmatrix} \qquad \mathbf{A}' = \begin{pmatrix} \partial_x(p_{11}) & \dots & \partial_x(p_{1n}) \\ \partial_x(p_{21}) & \dots & \partial_x(p_{2n}) \\ \vdots & \vdots & \vdots \\ \partial_x(p_{m1}) & \dots & \partial_x(p_{mn}) \\ \partial_y(p_{11}) & \dots & \partial_y(p_{1n}) \\ \partial_y(p_{21}) & \dots & \partial_y(p_{2n}) \\ \vdots & \vdots & \vdots \\ \partial_y(p_{m1}) & \dots & \partial_y(p_{mn}) \end{pmatrix}$$

The standard SVD algorithm can now be applied to $\mathbf{A}'$ resulting in

$$\mathbf{A}' = \mathbf{U}'\mathbf{W}'\mathbf{V}'^{\mathbf{T}}$$

and O2 modes can finally be calculated as

$$\mathbf{U_2} = \mathbf{A}\mathbf{V}'\mathbf{W}'^{-1} \tag{22}$$

Both O1 and O2 modes are a complete representation of the deformable device aberration in a finite set of modes.
The only difference between them is the orthogonality law.

These modes are very useful, because in the experimental part of this thesis are used deformable lenses with only 16 and 18 actuators: as we will see, with this kind of devices the *optimum modes* can be reproduced better than theoretical modes such as Zernike and Lukosz ones.

1.7 CLOSED LOOP CONTROL SYSTEM

In this last paragraph a conventional Adaptive Optics system with a closed loop control will be discussed (Figure 9) [5].

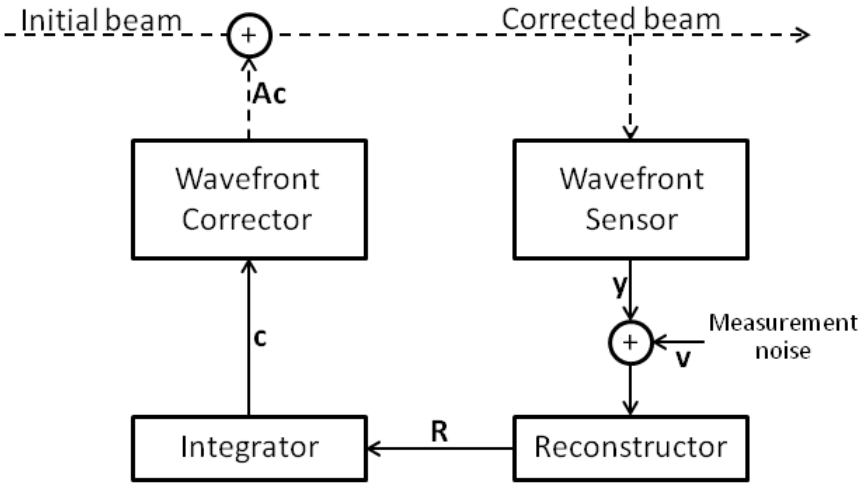

Figure 9: Basic diagram of a conventional Adaptive Optics system with a closed loop control. The dashed arrows represent optical signals, while the solid ones represent electrical signals.

Generally, these control systems incorporates an *integrator* to induce memory in the system, otherwise the information about the previous aberrations would be lost.

A state space representation of the system can thus be written as

$$\begin{cases} \mathbf{\Phi}_{k+1} = \mathbf{\Phi}_k + \mathbf{A}\mathbf{c}_k \\ \mathbf{y}_k = \mathbf{\Phi}_k + \mathbf{v}_k \end{cases}$$

where $\mathbf{\Phi}$ is the vector of wavefront aberrations, $\mathbf{A}$ is the *influence matrix* of the deformable device, $\mathbf{c}$ is the *actuator commands vector*, $\mathbf{v}$ is the vector of measurement noise, $\mathbf{y}$ is the vector of measured aberrations and k is the sample time index.

In a discrete time system, the *integrator* for the command vector $\mathbf{c}$ can be implemented as

$$\mathbf{c}_k = -\mathbf{R}\mathbf{y}_k + \mathbf{c}_{k-1}$$

where $\mathbf{R}$ is a matrix that must be determined, called *reconstructor*.

If we want to correct the aberrations, we must find an $\mathbf{R}$ such that $\mathbf{\Phi}_{k+1} = 0$. This can be done by determining the inverse of the *influence matrix*, so that the *actuator commands vector* is given by (setting $\mathbf{c}_{k-1} = 0$)

$$\mathbf{c}_k = -\mathbf{R}\mathbf{y}_k = -\mathbf{A}^{-1}\mathbf{y}_k \simeq -\mathbf{A}^{-1}\mathbf{\Phi}_k$$

and then we find

$$\mathbf{\Phi}_{k+1} = \mathbf{\Phi}_k + \mathbf{A}\mathbf{c}_k = \mathbf{\Phi}_k - \mathbf{A}\mathbf{A}^{-1}\mathbf{\Phi}_k = \mathbf{\Phi}_k - \mathbf{\Phi}_k = 0$$

Since the *influence matrix* usually isn't a square matrix, its inverse must be determined by least squares techniques. The simplest solution to this problem is the Moore-Penrose pseudo inverse, given by

$$\mathbf{R} = \tilde{\mathbf{A}}^{-1} = [\mathbf{A}^T\mathbf{A}]^{-1}\mathbf{A}^T$$

Nevertheless, the *piston* term in the *influence matrix* can cause it to be singular. There is a simple trick that can be used to compensate for the *piston* term, which consists in adding a row of *ones* to the bottom of $\mathbf{A}$: in this way the singularity is removed.

Another easy (and more numerically reliable) way to estimate $\tilde{\mathbf{A}}^{-1}$ is a *singular value decomposition* (SVD), already explained in paragraph 1.6.2. If we apply the algorithm on $\mathbf{A}$ we find

$$\mathbf{A} = \mathbf{U}\mathbf{W}\mathbf{V}^T$$

and then

$$\mathbf{R} = \tilde{\mathbf{A}}^{-1} = \mathbf{V}\mathbf{W}^{-1}\mathbf{U}^T$$

Once $\mathbf{R}$ is known, it's thus possible to implement a closed loop control system.

2

SIMULATIONS

The simulations presented in this chapter were performed with MATLAB (R2001b, *The MathWorks*).

2.1 COMMON PARAMETERS

In all the simulations we are going to perform, some of the parameters defining the optical system are fixed.
Let's list them:

- the source of illumination is supposed to be incoherent, and this is easy to model using the equations described in paragraph 1.2;
- the system has got a circular pupil with a diameter $D = 2.5$ cm;
- the light that goes through the system is monochromatic, with wavelength $\lambda = 633$ nm;
- the distance from the pupil to the image plane is $z = 25\text{cm}$.

Furthermore, the first 3 Zernike and Lukosz polynomials (i.e. piston, tip and tilt) aren't used to simulate system's aberrations.
In Figure 10 an imaging simulation is shown, using the parameters listed above.

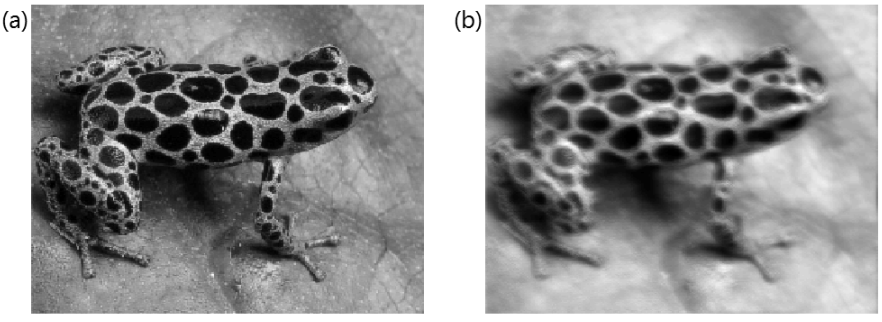

Figure 10: The same sample convolved (a) with an aberration-free PSF and (b) with an aberrated PSF (0.32 waves rms of the first 11 Zernike polynomials without piston, tip and tilt). The PSFs are those shown in Figure 6

2.2.1 *Muller and Buffington metrics*

A simulation to compare the sharpness metrics listed in paragraph 1.4.2 was performed. They are all very simple to estimate starting from the irradiance in the image plane.
A (fixed) random combination of 8 Zernike polynomials ($Z_i, i = 4, ..., 10, 13$) was used to simulate the aberration. Then the value of each Zernike coefficient was changed in order to change the amplitude of the aberrated wavefront without changing its shape. In this way we can see how the sharpness metrics vary with the aberration amplitude. The results are shown in Figure 11.

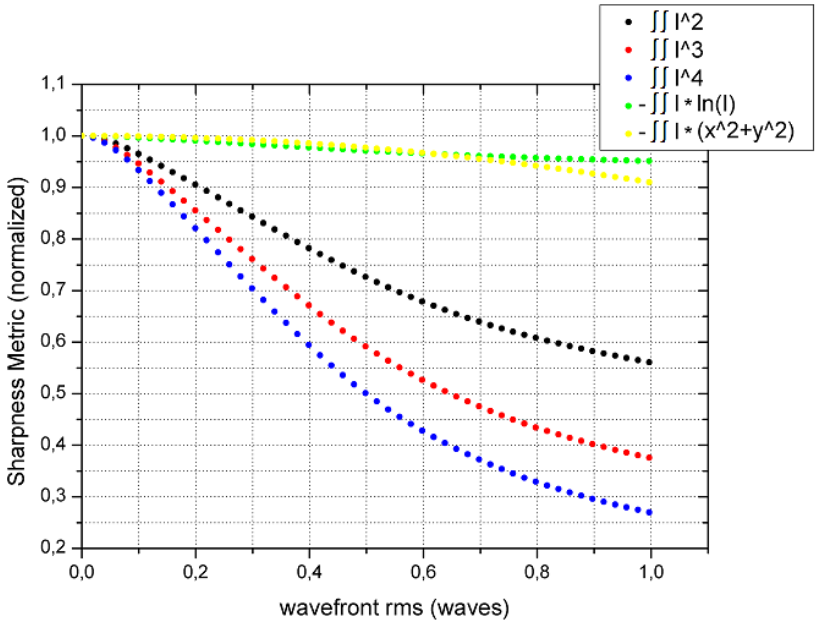

Figure 11: Comparison of the irradiance-based metrics (Muller and Buffington) listed in paragraph 1.4.2. Each metric is normalised with respect to its maximum value. The x-axis contains the rms of the aberrated wavefront expressed in waves.

We can see that all the metrics present a maximum when the wavefront rms is zero, as expected. The metrics IQ, S_3 and S_4 (previously defined in paragraph 1.4.2) have also a good behaviour beyond the maximum: they vary quite rapidly so they are easy to fit. On the contrary, S_5 and S_6 metrics aren't so good because they vary very slowly with increasing aberration amplitudes: we would need a greater number of metric evaluations to find their maximum with a fit.

An important thing that must be taken into account is that these irradiance-based metrics are strongly sensitive to light variations. The amount of light from one image to the next may vary due to the deformations introduced by the deformable device (in particular by the defocus mode) or to the light from the environment. This problem can be avoided adding a normalisation to the IQ metric, that is

$$IQ = \frac{\iint I(x,y)^2 dxdy}{\left(\iint I(x,y) dxdy\right)^2} \tag{23}$$

Finally, in 2003 Fienup and Miller showed that S_3 and S_4 metrics are well suited to bright features on dark background, while IQ metric is good for a larger set of image properties.
From now on we will use the IQ metric defined in equation 23.

2.2.2 *Properties of IQ metric and SD metric*

Using the the definition of the IQ metric in Eq.23, the same random combination of Zernike polynomials of the previous paragraph was used to create the aberration, and then the IQ metric was plotted against the aberration amplitude. Then a (fixed) random combination of Lukosz polynomials ($L_i, i = 4, ..., 10, 13$) was used to perform the same simulation. The results are shown in Figure 12.

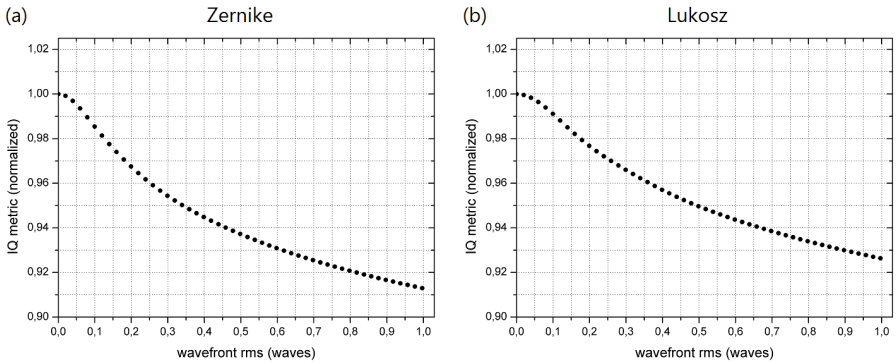

Figure 12: IQ metric defined on Eq.23 against the rms of the aberrated wavefront (in waves). The metric is normalised with respect to its maximum value. The polynomials used to generate the aberration are (a) Zernike and (b) Lukosz ones.

As expected, the new IQ metric (Eq.23) varies less rapidly than the previous one (Eq.12), but preserves the same shape and properties.

We are now interested in comparing this metric with the SD metric. Using the same combination of polynomials to generate the aberrations, three simulations were performed, changing the range of integration of the spatial frequencies each time (i.e. M_1 and M_2 in Eq.13, which in the simulations can vary from 0 to 1). This is shown in Figures 13 and 14.

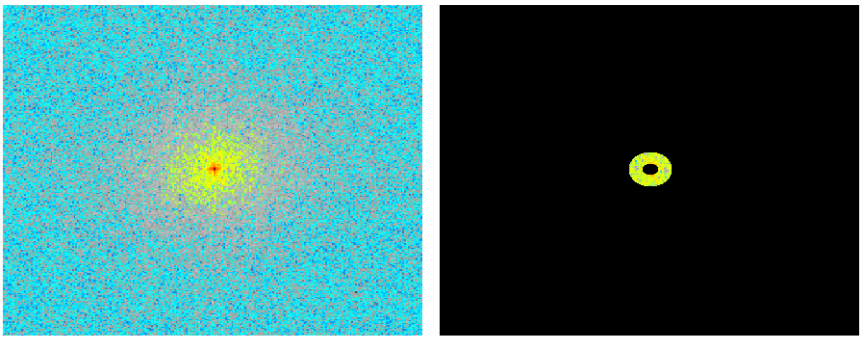

Figure 13: (left) Forurier Transform of Figure 10 (a) and (right) the same Fourier Transform where only spatial frequencies in the range $(0.03, 0.1)$ were selected. The maximum range of spatial frequencies is $(0, 1)$.

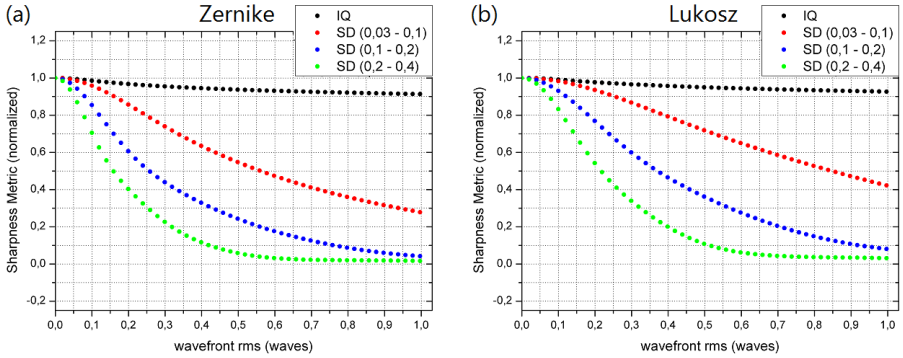

Figure 14: Imaging sharpness metrics against the rms of the aberrated wavefront (in waves). The metrics are normalised with respect to their maximum value. The polynomials used to generate the aberration are (a) Zernike and (b) Lukosz ones. For the SD metrics, the range of integration of the spatial frequencies (M_1, M_2) is indicated on the top right of the graphs.

From Figure 14 we can see that SD metrics have a maximum when the wavefront is flat and they varies more rapidly beyond this maximum than IQ metric. Furthermore, the higher the spatial frequencies used in the SD metric are, the more rapid the decay of the metric beyond its maximum is. This property is very interesting because changing the range of integration (M_1, M_2) it's possible to correct different types of aberrations: low frequencies ranges are useful to correct large aberrations, while high frequencies ranges are useful to correct small ones.

We can also verify Eq.16: if we choose the range (M_1, M_2) in the low spatial frequencies, the reciprocal of the SD metric should be a parabola [30].

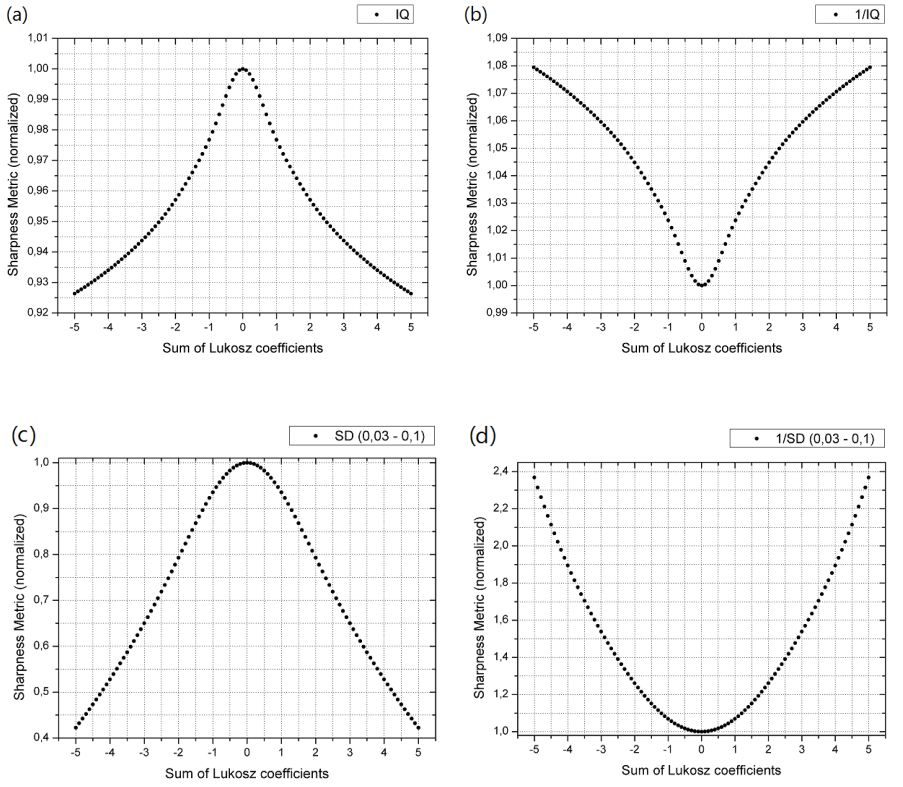

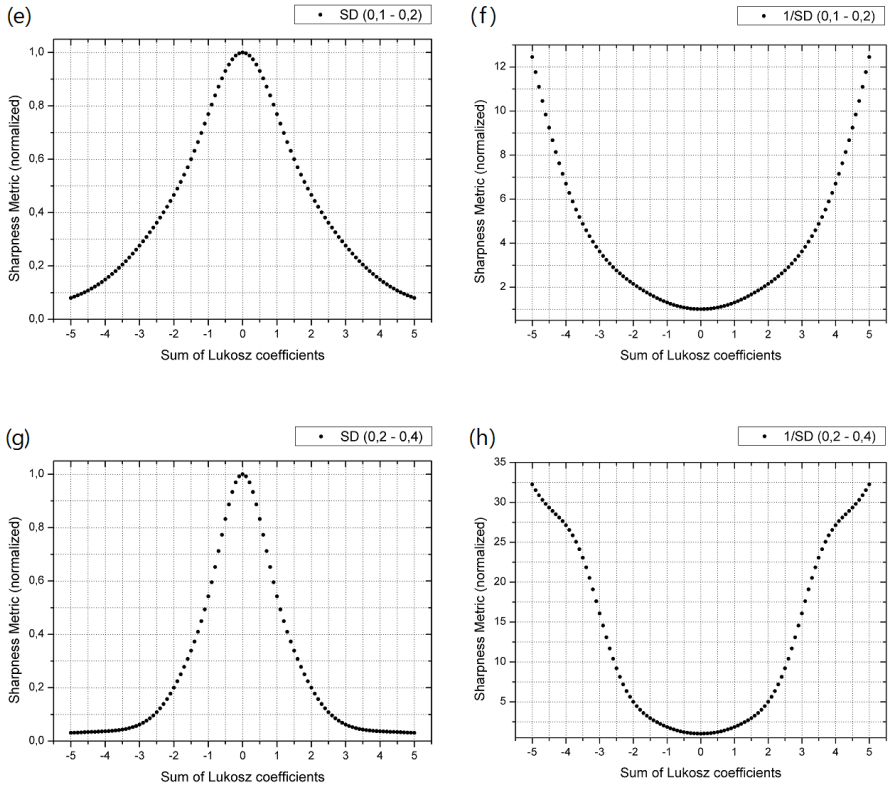

Figure 15: Imaging sharpness metrics and their reciprocals. The x-axis contains the sum of the Lukosz coefficients that together form the aberration: in this way we can plot also the negative values to point out the geometry of the functions (a sum of Lukosz coefficients equal to 5 (or -5) corresponds to a wavefront rms $\simeq 1$ waves). The metrics are normalised with respect to their global extremum. Lukosz polynomials were used to generate the aberration. IQ metric and its reciprocal are shown in (a,b) while SD metric and its reciprocal are represented taking into consideration three different ranges of spatial frequencies: (c,d) from 0.03 to 0.1, (e,f) from 0.1 to 0.2 and (g,h) from 0.2 to 0.4.

The reciprocals of the metrics are shown in Figure 15. The aberration is generated using Lukosz polynomials, as required in Eq.16.
We can see that the reciprocal of the IQ metric doesn't have any interesting property (it has the same characteristics of the IQ metric itself), while the reciprocal of the SD metric presents the shape that we expected. In greater detail, the reciprocal of the SD metric is clearly a parabola for low spatial frequencies (Figure 15 (d)) and it gradually lose this shape taking into account higher spatial frequencies (Figure 15 (f,h)). If we want to take advantage of Eq.16, then we must work with low spatial frequencies $(M_1, M_2) = (0.03, 0.1)$.

The reciprocal of the SD metric with $(M_1, M_2) = (0.03, 0.1)$ was also taken, using Zernike polynomials. The result, in Figure 16, shows that with Zernike polynomials we still find a parabolic shape (at least approximately).

Finally, the *Parseval Theorem* (outlined in paragraph 1.4.4) was verified. For this purpose, the IQ metric and the SD metric (integrated over all the spatial frequencies) were plotted on the same graph, both for Zernike and Lukosz polynomials. Figure 17 shows that Eq.17 is perfectly satisfied: the *Parseval Theorem* has been verified.

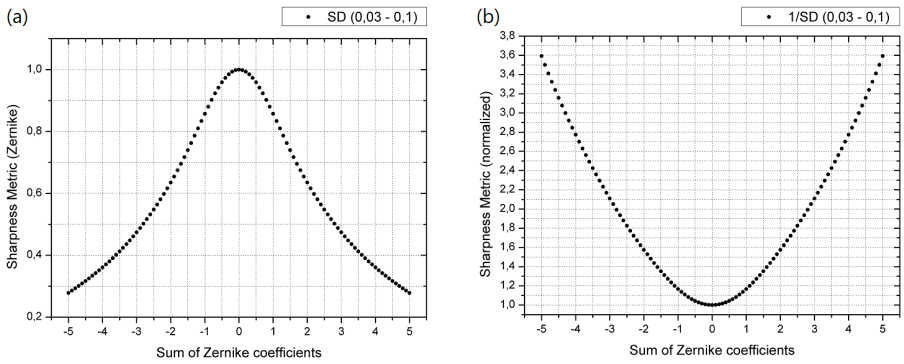

Figure 16: (a) SD metric with $(M_1, M_2) = (0.03, 0.1)$ and (b) its reciprocal against the sum of Zernike coefficients. A sum of Zernike coefficients equal to 5 (or -5) corresponds to a wavefront rms $\simeq 1$ waves.

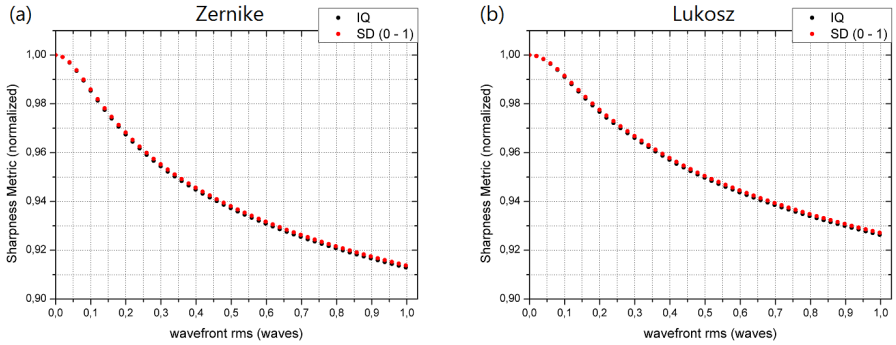

Figure 17: IQ metric and SD metric with $(M_1, M_2) = (0, 1)$ overlapped to verify the *Parseval Theorem*. The aberration is made up of a random combination of (a) Zernike and (b) Lukosz polynomials.

2.3 ABERRATION CORRECTION

We are now ready to simulate the aberration correction using the optimisation algorithms explained in the previous chapter. A lot of simulations were performed using the *Modes Correction Algorithm* in order to understand its potentialities and limits. Then the *Nelder-Mead Simplex Algorithm* was used with the S_3 metric [22] to compare the two methods.

2.3.1 *Aberration correction using the Modes Correction Algorithm*

The *Modes Correction Algorithm* was tested in the simulated optical system using both IQ metric and SD metric, first with Zernike polynomials and then with Lukosz ones. The aberrations consist of a random combination of eight polynomials (Z_i or $L_i, i = 4, ..., 10, 13$) with total amplitude fixed. The same polynomials are used to correct the aberration: after choosing a *bias* b, the algorithm can be applied, requiring a total of $2N + 1 = 17$ SD metric evaluations or $4N + 1 = 33$ IQ metric evaluations ($N = 8$ is the number of polynomials used in the correction process) to perform a complete aberration correction. Indeed, if we use the inverse of the SD metric with $(M_1, M_2) = (0.03, 0.1)$ the functions we have to fit in the algorithm

will be parabolas and each parabola needs only 3 points to be completely defined, while for the IQ metric there isn't a simple function thus it's necessary to use a polinomial of degree 4 (or more) to fit it, that is, we have to estimate at least 5 points per mode.

30 corrections of random aberrations were performed for each value of the initial wavefront rms, and then the mean and the standard deviation of the wavefront rms after the correction were calculated. The results are shown in Figure 18.

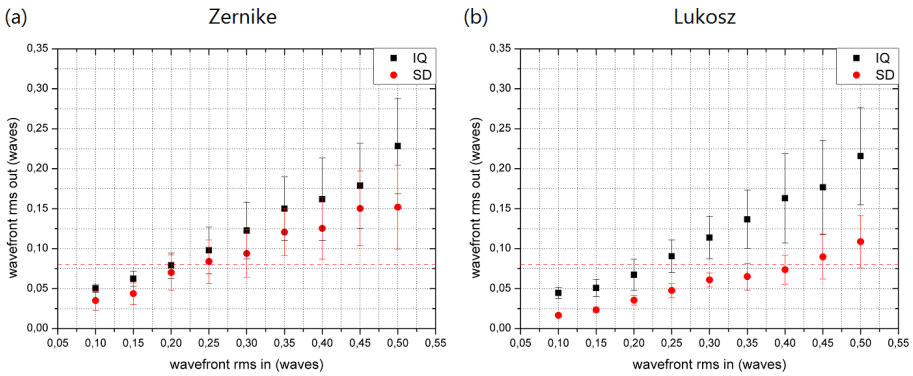

Figure 18: Initial wavefront rms against wavefront rms after the correction. The aberration corrections are performed with 5-points fits for the IQ metric (black squares) and with 3-points fits for the SD metric (red circles). Each point in the graphs represents a mean of 30 random aberration corrections. The red dashed lines represent the *Maréchal Criterion*. (a) Zernike polynomials and (b) Lukosz polynomials were used to generate the aberrations and also to correct them.

From the graphs in Figure 18 we can see that

- the IQ metric works in the same way with both Zernike and Lukosz polynomials, and the correction is good (according to *Maréchal Criterion*) for an initial wavefront rms up to 0.25 waves.
- the SD metric is better than the IQ one in both cases: working with Zernike polynomials, the correction is good for an initial wavefront rms up to 0.30 waves, while with Lukosz polynomials the correction is good for an initial wavefront rms up to 0.50 waves.

2.3.2 *Modes crosstalk in the Modes Correction Algorithm*

The results achieved in the previous paragraph are in agreement with Eq. 16 and the considerations advanced in the previous chapter: the SD metric used with Lukosz polynomials gives the best results. Nevertheless, even in the best configuration the algorithm doesn't correct completely wavefront aberrations with an rms greater than 0.5 waves (Figure 18). The principal cause of this fact is that each single mode correction is *not* totally independent from the others. We can verify this as follows:

- after choosing a polynomial basis, generate an aberration using only a certain mode (i.e. set the first polynomial coefficient c_4 to a certain value, for example 0.5, and the others to zero);

- perform an aberration correction of the first eight modes using the *Modes Correction Algorithm*;

- save the coefficients of each mode that the algorithm provides to correct the aberration;

- repeat this procedure for all the modes used in the correction.

If each single mode correction is independent from the others, the only component that could be different from zero must be the same used to generate the aberration.

The procedure described above was implemented using the SD metric with Zernike (Figure 19) and Lukosz (Figure 20) polynomials. The image in Figure 10 was used as sample.

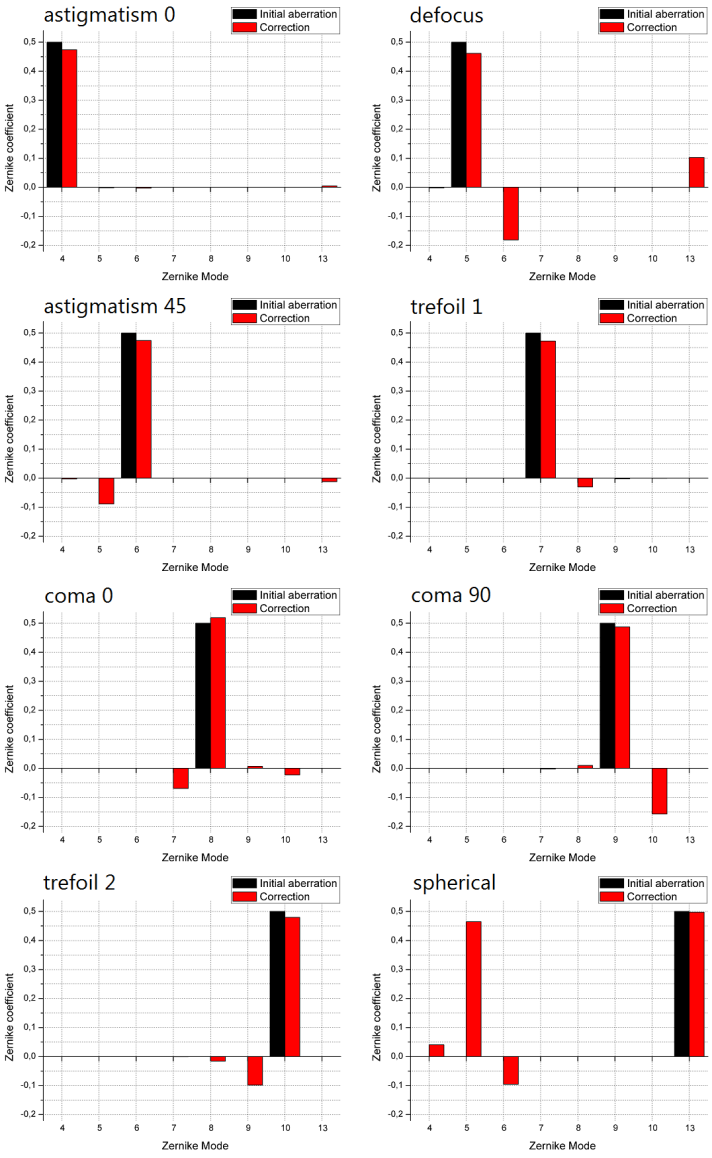

Figure 19: Crosstalks between each single Zernike mode and the other ones in the *Modes Correction Algorithm*. Black bars represent the Zernike coefficients of the initial aberrated wavefront, while red bars represent the Zernike coefficients (provided by the algorithm) of the wavefront that must be subtracted to the initial one in order to obtain a flat wavefront. The sample used in the simulations is that of Figure 10

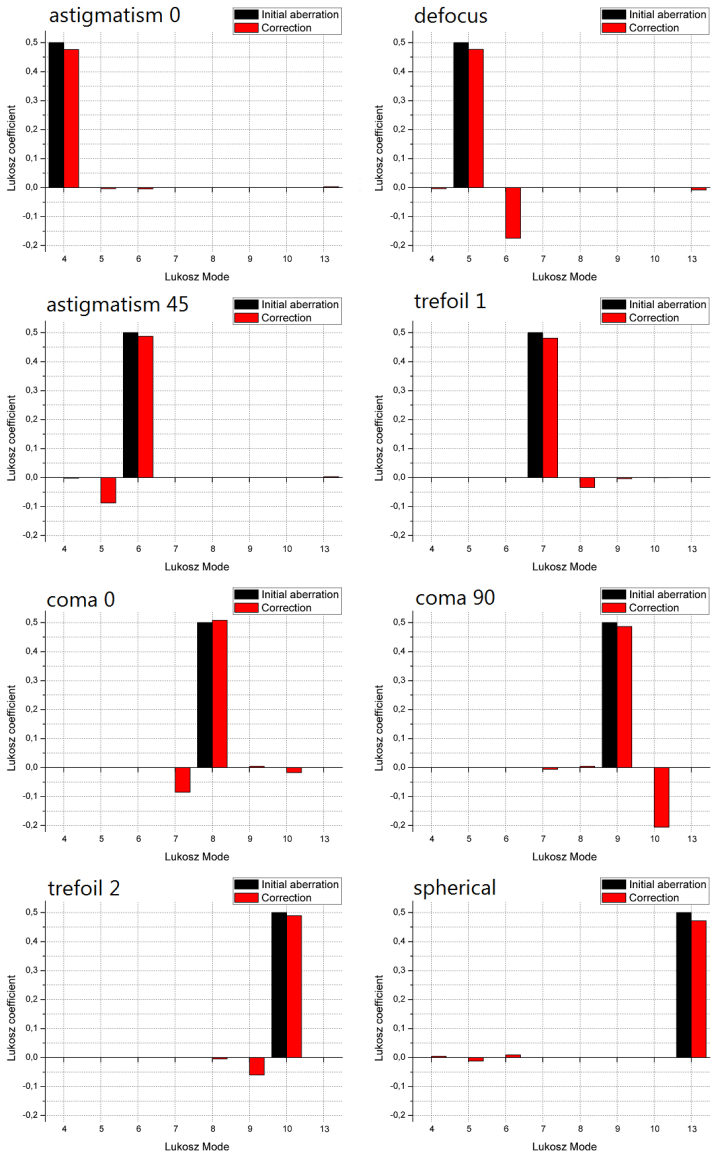

Figure 20: Crossstalks between each single Lukosz mode and the other ones in the *Modes Correction Algorithm*. Black bars represent the Lukosz coefficients of the initial aberrated wavefront, while red bars represent the Lukosz coefficients of the wavefront (provided by the algorithm) that must be subtracted to the initial one in order to obtain a flat wavefront. The sample used in the simulations is that of Figure 10

From these graphs we can see that effectively the modes aren't independent of each other: in some cases, the metric appears distorted and an ideal aberration correction can't be performed. Changing the sample in the simulations, the results are quite the same in terms of quantity, even if some modes interfere with the others in different ways than those shown in Figures 19 and 20. In our example, the most significant difference between Lukosz and Zernike polynomials is the crosstalk between *defocus* (mode 5) and *spherical aberration* (mode 13). Indeed, in the case of Zernike polynomials, from Figure 19 we can see a great crosstalk between these two modes, while using Lukosz polynomials (Figure 20) this crosstalk disappears. We can better understand this fact plotting the SD metric for a variable value of defocus, maintaining a fixed value of spherical aberration (Figure 21).

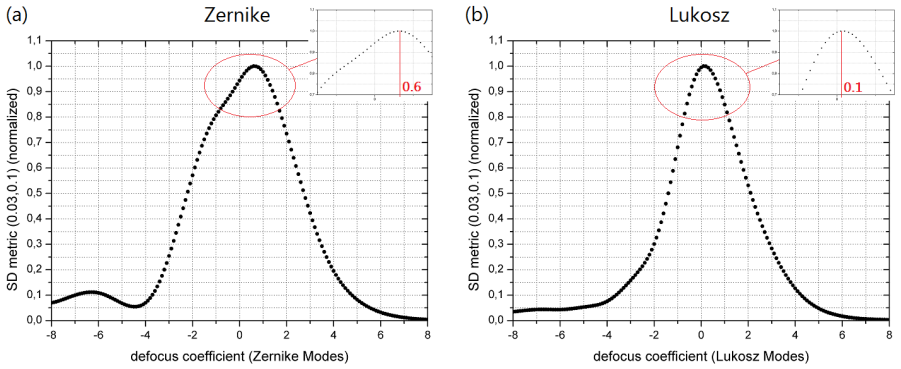

Figure 21: Simulation of defocus correction in presence of a fixed quantity of spherical aberration (0.5 waves rms) using the *Modes Correction Algorithm* with (a) Zernike polynomials and (b) Lukosz polynomials, both with the SD metric integrated in the spatial frequencies range $(M_1, M_2) = (0.03, 0.1)$. The squares on the top right of the graphs shows the correction coefficient a_{corr} that maximises the sharpness metric. The sample used in the simulations is that of Figure 10

It's clear that using Zernike polynomials the algorithm fails: we are expected to find a maximum of the SD metric when the defocus coefficient is zero, that is, when our system is free from defocus aberration. Nevertheless, we find a value of $c_{5,corr} \simeq 0.6$ ($= 0.34$ waves rms) with Zernike modes, $a_{5,corr} \simeq 0.1$ ($= 0.04$ waves rms) with Lukosz ones. Further errors emerge from other dependent modes, such as *coma* and *trefoil* (modes 9 and 10) or *defocus* and *astigmatism* (modes 5 and 6).

This explains why in Figure 18, using the SD metric, the *Modes Correction Algorithm* performs better with Lukosz modes than with Zernike ones, but the correction isn't perfect even if we use Lukosz modes.

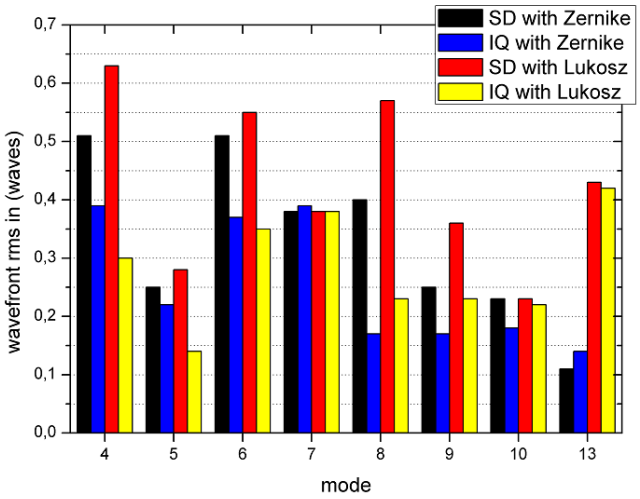

Figure 22: Maximum values of aberrations, composed of a single mode, that can be corrected by the *Modes Correction Algorithm*. The aberrations are expressed in waves. In the caption (top right of the graph) the metric and the polynomials used in the algorithm are specified.

The graph in Figure 22 shows the maximum aberrations, composed of a single mode, that can be corrected (according to *Maréchal Criterion*) using the *Modes Correction Algorithm*: the sample and the

modes in the simulations are the same of the previous ones, and both the metrics (SD and IQ) and the basis of polynomials (Lukosz and Zernike) were used. Once again, it can be seen that the best results are obtained with the SD metric (here in the range $(M_1, M_2) = (0.03, 0.1)$) using Lukosz polynomials. In particular, a big improvement can be noticed in the correction of the *spherical aberration* by moving from Zernike to Lukosz polynomials, for both the metrics.

2.3.3 *Bias dependence in the Modes Correction Algorithm*

Trying different values of the *bias* b, it can be noticed that if we are using the SD metric its value isn't so important (i.e. we must choose b reasonably large according with the amplitude of the aberration that affects the system, but without particular care), while if we are using the IQ metric the value of b must be chosen very carefully: in the first case we know *a priori* that the function is a parabola, and choosing a bias smaller than the aberration amplitude we might find the global extremum of the function with a lack of precision (but we will actually find it), while in the second case we are fitting our function with a more complex polynomial and if we choose a *bias* smaller (or much greater) than the aberration amplitude we won't find the correct global extremum.

In Figure 23 a *trefoil* aberration (Lukosz mode L_7) of initial rms value equal to 0.23 waves was corrected, for different values of the *bias*: from Figure 22 it can be seen that this mode can be well corrected up to ~ 0.38 waves rms with both the SD and the IQ metrics, therefore the dependence of the correction on the *bias* value can be highlighted.

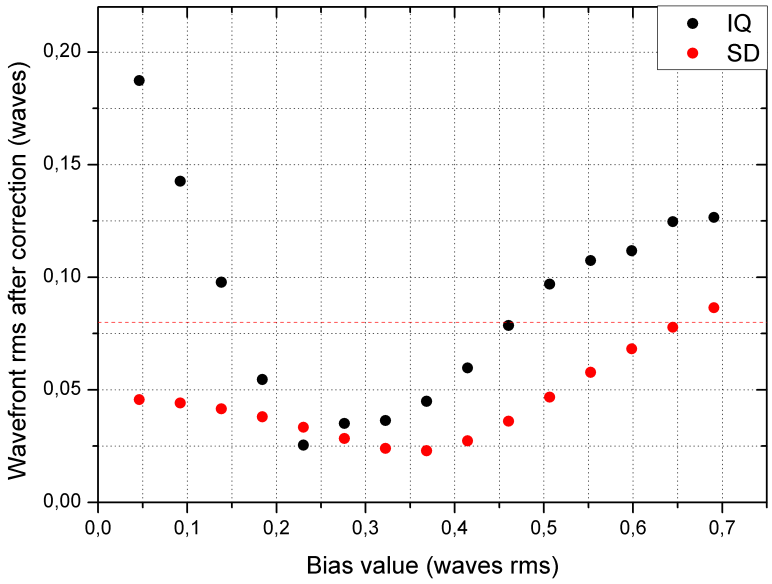

Figure 23: Trefoil aberration (Lukosz mode L_7, 0.23 waves rms) corrected with different values of the *bias* b (on x-axis). The y-axis contains the value of the wavefront rms after an iteration of the *Modes Correction Algorithm*. The red dots are obtained with the SD metric, while the black ones with the IQ metric. Finally, the red dashed line represents the *Maréchal Criterion*.

From Figure 23 we can conclude that, in the case of the IQ metric, the *bias* value must be chosen as close as possible to the value of

the initial wavefront rms value. This is true for the SD metric too, but the range of *bias* values which allows to reach a good aberration correction is larger.

2.3.4 *Multiple iterations of the Modes Correction Algorithm*

When the aberration is too large, one iteration of the *Modes Correction Algorithm* isn't sufficient to correct the aberration completely. Nevertheless the final rms value of the total aberration, in many cases, is smaller than the initial one. If this is the case, we can try to apply the algorithm to the final wavefront again, until reaching a value of the wavefront rms under the *Maréchal Criterion*.
These simulations were performed using Lukosz polynomials and the SD metric. Furthermore, it can be noticed that changing the order of correction of the modes leads to improvements in the correction: trying different combinations, also using the informations contained in Figure 20, and it can be found that the best order of correction for the eight Lukosz modes $L_i, i = 4, ..., 10, 13$ for the sample of Figure 10 is

$$4, 13, 7, 10, 8, 6, 5, 9.$$

We can easily understand why this combination is the best: if we first correct the modes that are independent from the others (i.e. modes 4 and 13), we'll reduce the total aberration before correcting the modes that are more dependent from the others (i.e. modes 5 and 9), so we have the best conditions to perform a good correction.

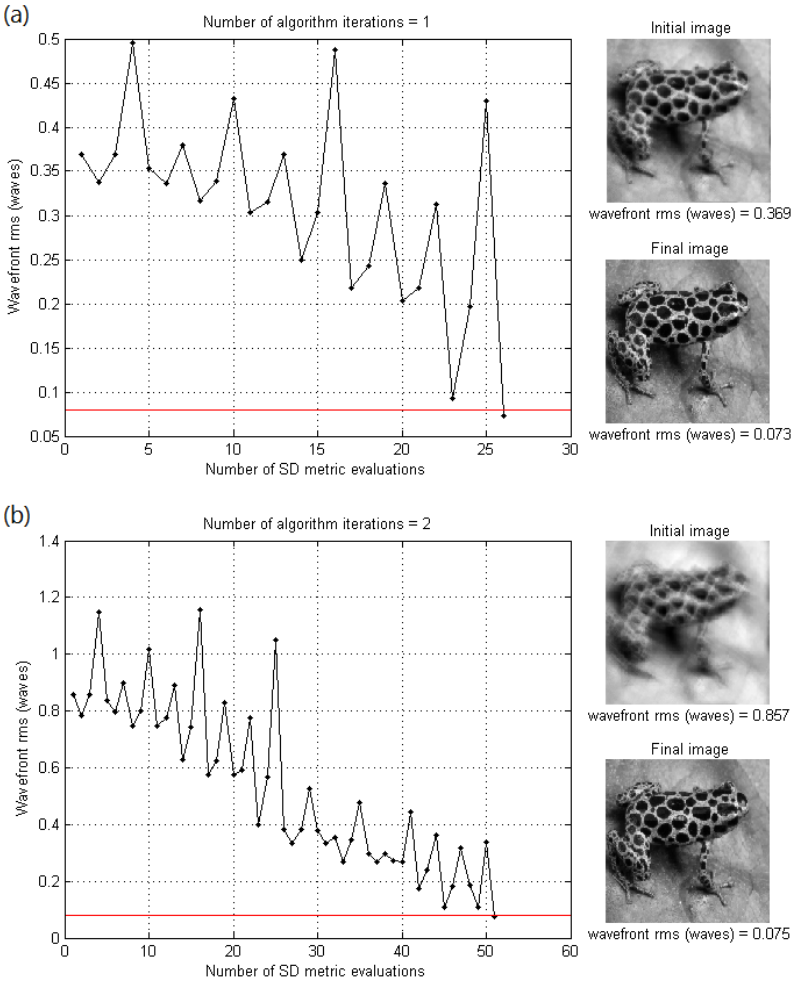

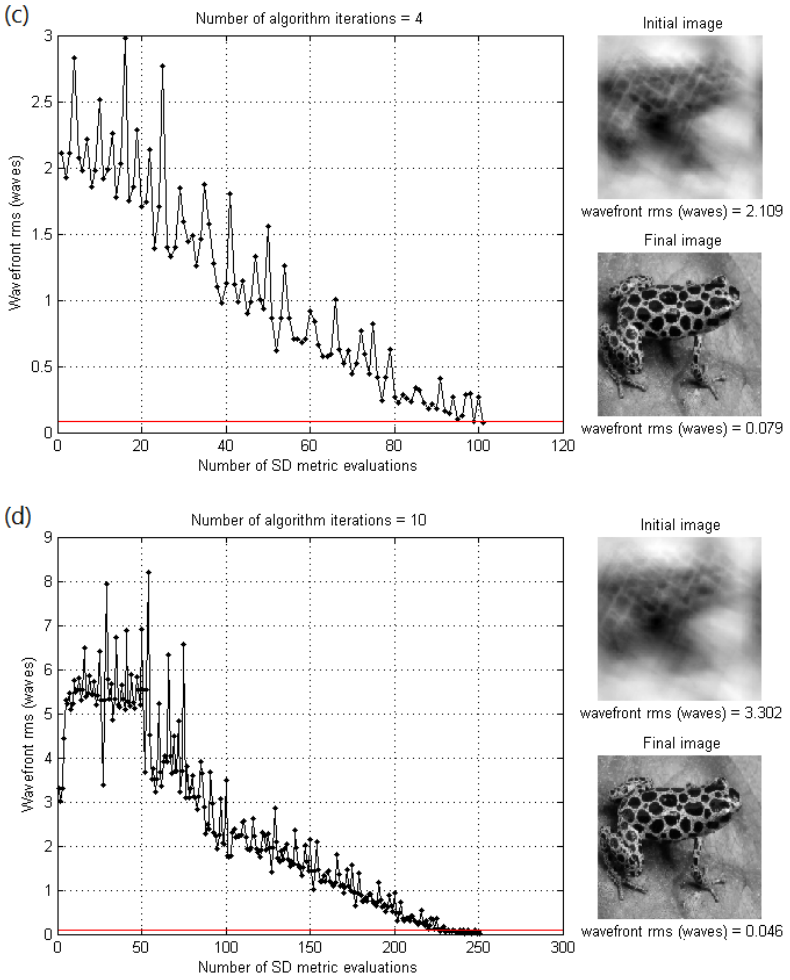

Figure 24: Aberration correction performed with (a) one, (b) two, (c) four and (d) ten iterations of the *Modes Correction Algorithm*. The initial aberration is composed of a random combination of the same Lukosz polynomials used in the correction. The metric used in the algorithm is the SD metric with $(M_1, M_2) = (0.03, 0.1)$. Each a_{corr} was evaluated with a three-points fit (i.e., every iteration requires $8 \cdot 2 + 1 = 17$ metric evaluations). The red line in the graphs represents the *Maréchal Criterion*.

Clearly, this sequence *depends* on the sample that we are using, and may vary for other samples (for example, modes 4 and 6, which are the two *astigmatism* aberrations, interfere with *defocus*, mode 5, in different amounts depending on the sample). Let's see some aberration corrections with multiple iterations of the *Modes Correction Algorithm* with the conditions outlined above (Figure 24).

If we want to take advantage of the procedure just outlined, we must apply the correction relative to a certain mode immediately after that the corresponding mode coefficient has been evaluated: this doesn't allow to take only $2N + 1$ metric measurements, because now the aberration will change at each single mode correction (i.e., every time we apply a correction to the wavefront), so we now need a total of $3N$ metric measurements.

Finally, Figure 24 (d) shows that, with ten iterations of the *Modes Correction Algorithm*, it's possible to correct aberrations larger than 3 waves rms: it will take a great number (~ 250) of metric evaluations, but in principle it can be done.

2.3.5 *Optimum modes used in the Modes Correction Algorithm*

In all the simulations which have been made so far, we haven't considered the fact that in a real optical system the deformable device has some limitations:

- the magnitude of its deformation is limited by its physical proprieties, such as its dimensions and materials (e.g., the breaking limits of the membrane in a membrane deformable mirror);
- Lukosz and Zernike modes can't be perfectly reproduced by real deformable devices: this is especially true for devices with a small number of actuators.

We also have seen that we can try to minimize the second of these limitations using the natural *optimum modes* of the device.

In this paragraph we will generate O1 and O2 *optimum modes* of two real deformable devices: a deformable mirror with 36 piezoelectric actuators and a deformable lens with 16 piezoelectric actuators (these devices will be described in detail in the next chapter).

Let's outline the simulation procedure. First of all, we need the *influence matrix* of the deformable device we want to use in our optical system. This matrix can be measured following the procedure outlined in paragraph 1.6.1 using a Shack-Hartmann *wavefront sensor* (the experimental setup of these measurements will be studied in Chapter 4).

The *singular value decomposition* of a matrix in MATLAB can be easily performed with the function svd(): thus O1 modes can be determined immediately performing the svd decomposition of the *influence matrix*. O2 modes needs some further work: you need first determine the partial derivatives of the *influence matrix* using the MATLAB function grad(), and then set the resulting matrices as delineated in paragraph 1.6.2 before applying the function svd(). In Figures 25 and 26 we can see the *influence matrix* of the deformable lens and mirror respectively, and their *optimum modes*.

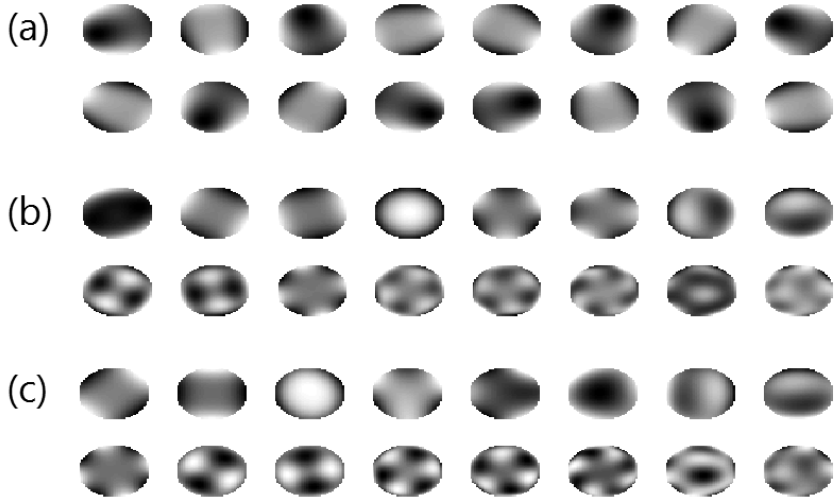

Figure 25: (a) *Influence matrix*, (b) O1 modes and (c) O2 modes of a deformable lens with 16 piezoelectric actuators. The *influence matrix* was evaluated using a Shack-Hartmann *wavefront sensor*. The deformable lens is controlled by an high voltage (+/- 125 V) driver (*Adaptica srl*, IO64).

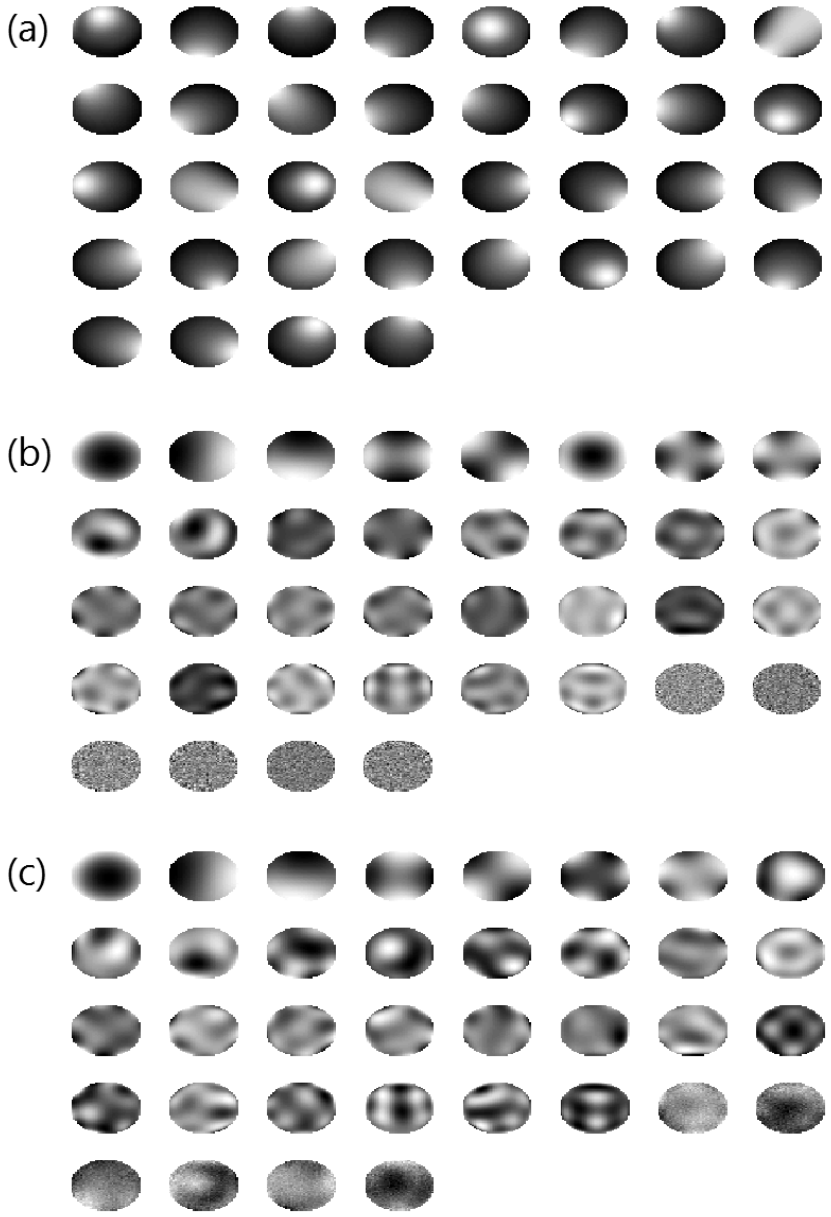

Figure 26: (a) *Influence matrix*, (b) O1 modes and (c) O2 modes of a deformable mirror with 36 piezoelectric actuators. The *influence matrix* was evaluated using a Shack-Hartmann *wavefront sensor*. The deformable lens is controlled by an high voltage (+/- 125 V) driver (Adaptica srl, IO64). All these devices will be described in detail in the next chapter.

Now we want to test these modes in an aberration correction simulation using the *Modes Correction Algorithm*. A random aberration were generated, using the first eight O1 modes, and then a random combination of eight Zernike modes ($Z_i, i = 4, ..., 10, 13$) was added, in such a way that the total aberration consisted of 70% O1 modes and 30% Zernike modes. Then the aberrated wavefront was normalised to a fixed initial rms value. Including Zernike modes enables us to simulate a more realistic initial aberration, because in this way we'll have aberrations that could and could not be corrected by the deformable device (as is usually the case in real optical systems). All the 16 O1 modes of the deformable lens were used in the *Modes Correction Algorithm* to perform the aberration correction, while for the deformable mirror only the first 30 O1 modes were used, because the last 6 *optimum modes* were actually noise (see Figure 26 (b) and (c)). The SD

metric with $(M_1, M_2) = (0.03, 0.1)$ was used, and a three-point fit for each mode to evaluate the correction coefficients. The same procedure was followed using O2 modes instead of O1 modes. The results are shown in the graphs in Figure 27.

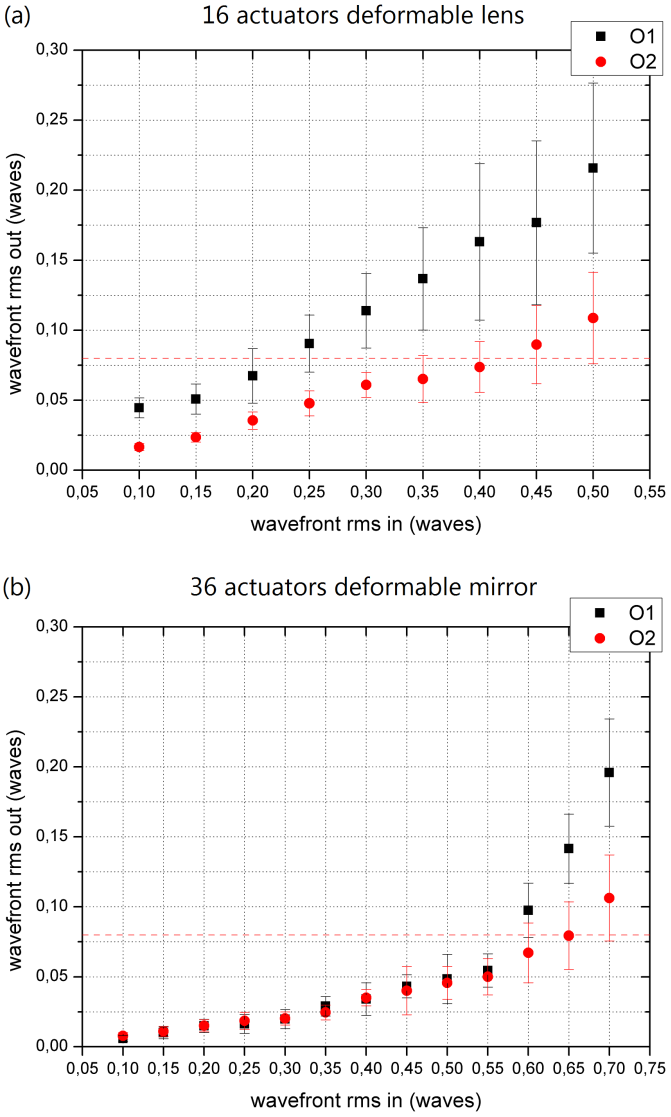

Figure 27: Aberration correction with the *Modes Correction Algorithm* and the SD metric integrated in the spatial frequencies range $(M_1, M_2) = (0.03, 0.1)$, using (a) O1 and O2 modes of the deformable lens in Figure 25 and (b) O1 and O2 modes of the deformable mirror in Figure 26. The sample used is that of Figure 10. The initial aberration consists of (*black squares*) 70% O1 modes (first eight) and 30% Zernike modes $(Z_i, i = 4, ..., 10, 13)$ or (*red circles*) 70% O2 modes (first eight) and 30% Zernike modes $(Z_i, i = 4, ..., 10, 13)$. For each inital wavefront rms value a total of 30 aberration corrections were performed (each one with a different random initial aberration). Each point in the graphs represents a mean of these 30 aberration corrections and the standard deviations of the wavefront rms after the correction are shown. The red dashed lines represent the *Maréchal Criterion*.

The results obtained in these simulations are in agreement with the theory: for a fixed initial wavefront rms, the algorithm performs better with O2 modes than with O1 modes in both the devices.
In the case of the deformable lens the difference between the two modes is quite broad, and the correction is good for an initial wavefront rms up to ~ 0.45 waves. In the case of the deformable mirror the

difference becomes to be noticeable only at large aberrations ($\geqslant 0.55$ waves rms) and the correction is good for an initial wavefront rms up to ~ 0.65 waves.

We conclude that the greater the number of actuators of our deformable device is, the larger the aberrations it can correct are. Furthermore, we could also apply more than one iteration of the algorithm in order to correct large aberrations. Nevertheless, the results might not be as good as those found in paragraph 2.3.4, because the residual aberration now consists mainly of a combination of Zernike modes that can't be completely corrected by our deformable devices, especially if they have a small number of actuators. We will see in the experimental part of this thesis how good Zernike, Lukosz, O1 and O2 modes can be reproduced by deformable devices with different features.

2.3.6 *Aberration correction using the Nelder-Mead Simplex Algorithm*

Finally, some aberration correction simulations were performed using the *Nelder-Mead Simplex Algorithm* outlined in paragraph 1.5.2.
A MATLAB function called fminsearch() was employed: this function uses the *Nelder-Mead Simplex Algorithm* to find the global minimum of a function of N variables (where $N = 8$, if we want to correct eight Zernike modes at the same time). The function used in the simulation is $-S_3$, where the minus sign is necessary because the function fminsearch() finds the global *minimum* of a given function and S_3 is one of the Muller and Buffington metrics that we rewrite here:

$$S_3 = \iint I(x,y)^3 \, dx dy$$

The choice of this sharpness metric is due to [22], where one of the results was a much faster convergence of S_3 metric compared to IQ and S_4 metrics in the *Nelder-Mead Simplex Algorithm*.
A random combination of eight Zernike polynomials ($Z_i, i = 4, ..., 10, 13$) was used to create the initial aberration, fixing their initial rms value. Furthermore, another random combination of the same eight Zernike polynomials was generated to initialize the algorithm (an initial simplex with eight vertex is required to initialize the Nelder-Mead algorithm), with a total rms value of $\sim 0.02 \div 0.05$ waves.

In Figure 28 three of these aberration corrections are shown, with increasing initial wavefront rms (0.2, 0.35 and 0.5 waves rms). We can see that, as expected, the correction of a large aberration requires more algorithm iterations (and thus more time) than a small one: 457 iterations were taken to fall below the Maréchal limit in the case of an initial wavefront of 0.2 waves rms, 724 iterations for an initial wavefront of 0.35 waves rms and 1075 iterations for an initial wavefront of 0.5 waves rms. This means that we have to take hundreds of metric measurements to correct the aberration (each iteration of the algorithm corresponds to a metric measurement), and in a real system this would take a lot of time. Furthermore, this time will increase rapidly if we want to correct more than eight Zernike modes. Thus, even if the aberration correction with the *Nelder-Mead Simplex Algorithm* is good, it can't compete with the *Modes Correction Algorithm*

in terms of time: we have seen that the same aberrations corrected in Figure 28 can be corrected with only $17 \div 24$ metric evaluations using the *Modes Correction Algorithm*, and correcting further modes would require only 2 or 3 other metric evaluations per mode. For this reason, we will use only the *Modes Correction Algorithm* in all of the experimental aberration corrections.

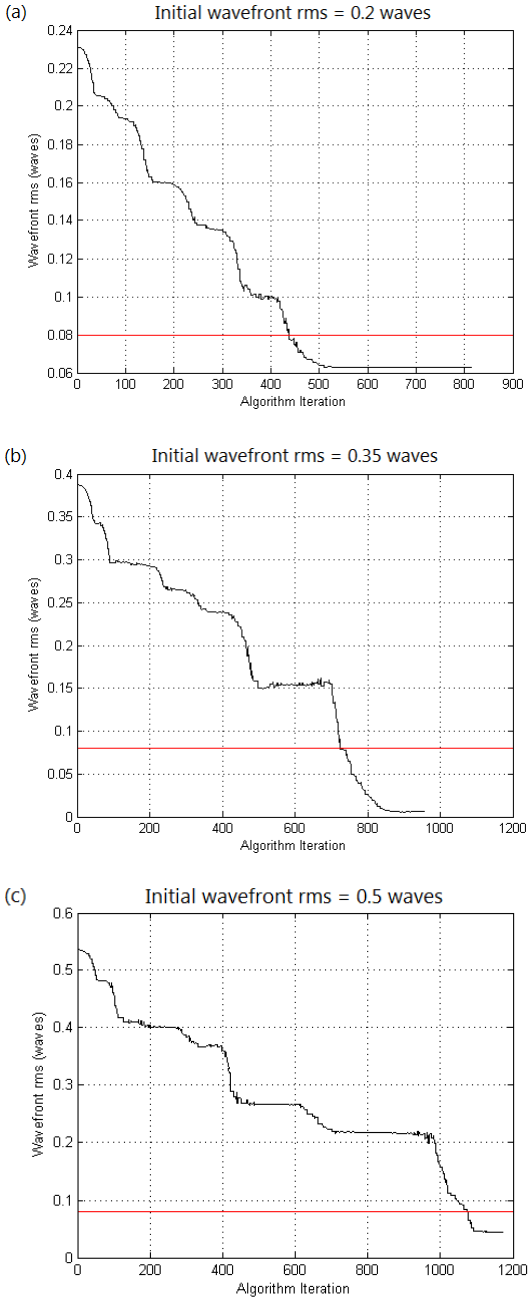

Figure 28: Aberration correction using the *Nelder-Mead Simplex Algorithm* with the S_3 metric. The inital wavefronts are combinations of the Zernike polynomials $Z_i, i = 4, ..., 10, 13$ with amplitude (a) 0.2, (b) 0.35 and (c) 0.5 waves rms. The x-axis contains the number of iterations of the algorithm. The red lines represent the *Maréchal Criterion*.

3

ADAPTIVE OPTICS DEVICES

In this chapter all the devices that are useful in an Adaptive Optics system are described. As we have already seen there are three principal subsystems in a typical Adaptive Optics systems: a *wavefront corrector*, a *wavefront sensor* and a control unit (i.e. a computer). We will start listing the principal deformable devices available as *wavefront correctors*, and then we will talk about the different ways to perform a wavefront measurement and the closed loop wavefront control [2,3,5,6].

3.1 WAVEFRONT CORRECTORS: DEFORMABLE MIRRORS

Deformable mirrors (DMs) are mirrors with a deformable surface, and they are the most frequently used *wavefront correctors*. They are good candidates as *wavefront correctors* because they can work with different types of light, they don't introduce chromatic aberration, they can be coated with extremely highly reflective coatings (this is important to avoid power loss in the system) and they can be represented as linear systems, so that the optical system can be controlled using the traditional linear control theory [5].

The principal parameters that characterize a deformable mirror are:

- The *number of actuators*, that determines the number of degrees of freedom of the DM (approximately one actuator corresponds to one degree of freedom). The bigger the number of actuators is, the higher the order of the aberrations that the DM can reproduce is (e.g., reasoning in terms of Zernike polynomials, a DM with a small number of actuators can reproduce less Zernike polynomials than a DM with a big number of actuators).

- The *distance between the actuator centres*, a.k.a. actuator pitch. DMs with a large actuator pitch and a big number of actuators are bulky and expensive.

- The *actuator stroke*, that is the maximum possible actuator displacement from a certain initial position (Typical values ranges from ± 1 to $\pm 10 \mu m$).

- The *Influence Matrix*, already explained in paragraph 1.6.1.

- The *actuator coupling*, that is, how much the movement of one actuator will displace its neighbours.

- The *response time*, that can vary from microseconds (e.g. MEMS mirrors) to tens of seconds (e.g. thermally controlled mirrors).

- The *hysteresis*, that can affect the mirror (e.g. DMs with piezoelectric actuators) or not (e.g. DMs electrostatically actuated). It is a residual positional error from previous actuator position commands, that limits the mirror ability to work in a predictable way.

There are several types of deformable mirrors. In the following paragraphs we will describe the most common ones and their features.

3.1.1 *Segmented DMs*

Segmented deformable mirrors are formed by independent flat mirror segments with piston and/or tip-tilt actuators. A segmented mirror with three degrees of freedom per segment(i.e., with piston, tip and tilt actuators) works rather better than one with less degrees of freedom.

Normally these mirrors have no cross-talk between actuators (as is instead the case for almost all the other types of deformable mirrors), but they suffer from diffraction on the segment edges and from light scattering due to the sharp edges of the segments and the gaps between the segments.

Their main advantage is that they can be very large, but they are also very expensive: they are usually used in big telescopes to correct piston, tip and tilt aberrations due to atmospherical turbulences, while higher order aberrations are corrected using other types of deformable mirrors.

3.1.2 *Continuous faceplate DMs*

Continuous faceplate deformable mirrors are made from a thin deformable reflective faceplate. Behind the faceplate they can have either force actuators (e.g. electromechanical or hydraulic) or displacement actuators (e.g. piezoelectric, magnetostrictive or thermal) that push and pull on the surface to deform it. The shapes that the mirror can assume depend on the combination of the forces applied to the faceplate, its boundary conditions (i.e. the way the faceplate is fixed to the mirror) and the geometry and the material of the faceplate: all these things contribute to the *influence matrix* of the DM.

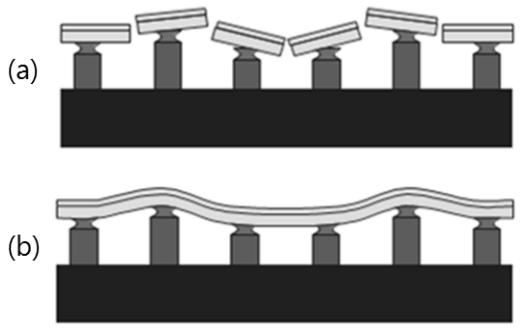

Figure 29: Simple schematic representations of (a) a segmented deformable mirror with piston, tip and tilt actuators and (b) a continuous faceplate mirror.

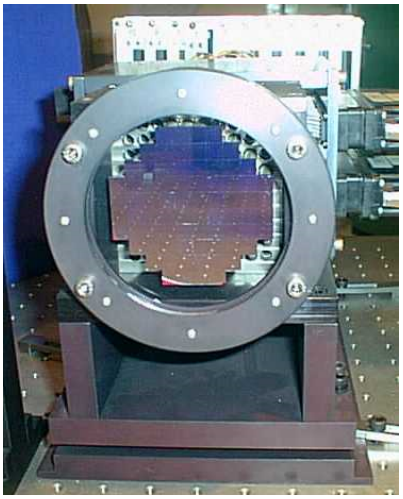

Figure 30: The 76-segmented deformable mirror NAOMI (William Herschel Telescope, UK) [57].

3.1.3 *Piezostack DMs*

The continuous faceplate DMs with displacement actuators usually use as faceplate a thin glass face-sheet with an high-reflection coating. The most common DM displacement actuators for DMs with a diameter larger than 2 cm are piezoelectric (and this is because they are the less expensive ones). The piezoelectric effect is essentially the creation of a strain-inducing stress under an applied electric field. Some materials exhibit a strong piezoelectric effect, such as the lead zirconate titanate $Pb(Zr,Ti)O_3$, commonly called PZT. The PZT is made in the form of a ceramic that is initially isotropic with randomly oriented dipoles: to produce piezoelectric effects, it must bee poled, which is accomplished at a temperature of $\sim 150°C$ by applying a DC electric field to align the dipoles parallel to the field.

The main limit of piezoelectric actuators is that they suffer from hysteresis (from 10% to 20% for PZT): for this reason the actuator deformation isn't perfectly proportional to the electric field applied, but rather follows an hysteresis curve. This fact implies that, if a certain shape is reproduced with a piezoelectric DM and this shape is reached after several consecutive *command vectors* sent to the device, and after relaxing the DM we want to repeat the same shape, we have to send exactly the same *command vectors* in the same order to the DM. Furthermore, if we send a command to the DM and then we send the inverse command, its shape won't be the same of the initial one, because of the hysteresis. The software which controls these devices must thus be realized with particular care of these properties in order to work in a correct way. An example of the effects of hysteresis in these actuators will be shown for a deformable lens with piezoelectric actuators in paragraph 3.3.1.

Finally, another commonly used material to build actuators is the lead magnesium niobate $Pb(Mg_{1/3},Nb_{2/3})O_3$, called PMN. This is an electrostrictive material (electrostriction is a property of all dielectrics without piezoelectric effects, in which the strain is proportional to the square of the applied electric field) with a huge dielectric constant, which doesn't need electric poling and doesn't suffer from

hysteresis (less than 1% at 25°C). Nevertheless, it is very sensitive to temperature variations.

3.1.4 *Bimorph DMs*

A *bimorph* is made from two thin layers of material bonded together, the relative sizes of which can be varied with a stimulus (e.g. temperature or voltage). We must distinct between bimorph actuators and bimorph mirrors.

Bimorph actuators employ two layers of piezoelectric material (such as PZT), or one piezoelectric and one inert layer (sometimes referred to as *unimorph*), to produce a controllable force. They are discrete devices that can be used in continuous faceplate or segmented DMs.

Bimorph DMs are devices in which the mirror faceplate itself is a continuous bimorph structure consisting of two layers, the shapes of which can be locally changed. When one or both the layers are made from piezoelectric material, the application of a voltage causes a change in size of the area under the electrodes and a consequent bending of the faceplate. The actuators of the DM are formed by a pattern of electrodes on the surface of the bimorph, and the construction of this type of devices is much simpler than that of discrete-actuator DMs.

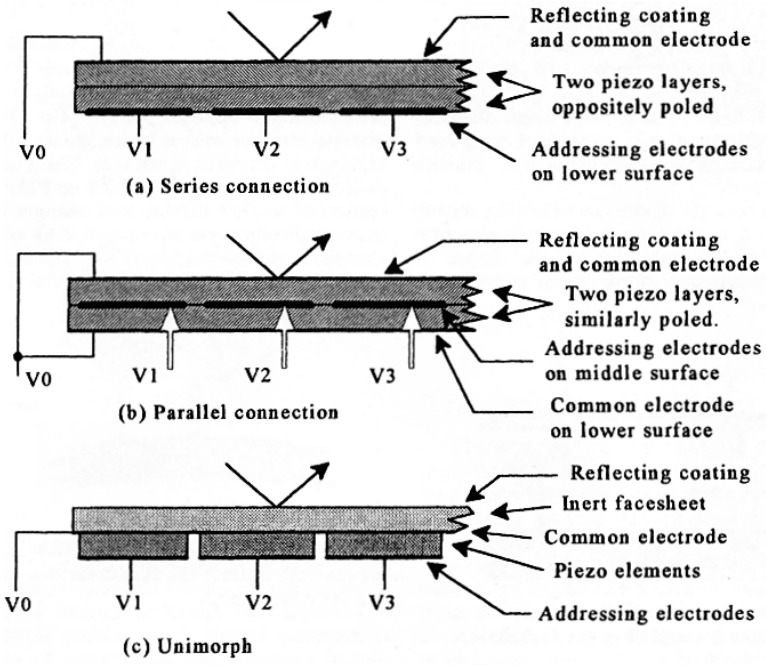

Figure 31: Simple schematic representation of three different possible configurations for a bimorph DM [2].

There are several possible bimorph configurations (Figure 31): in all of them an array of controlling voltages is applied to a pattern of electrodes placed on one of the layers, using a continuous electrode as the common element. Furthermore, the dimensions of the electrodes must be large with respect to the thickness of the layers to have a useful effect (tipically $\geqslant 4$ times): this limits the spatial resolution and the maximum number of actuators of a practical bimorph DM ($\#_{\text{actuators}} \leqslant 100$). Despite this, bimorph DMs have two significant

advantages: their performance matches very well with a *curvature sensor* (so there is no need of complex reconstruction circuitry to convert the curvature *wavefront sensor* signals into actuator commands) and, unlike other *wavefront correctors*, they can be configured to remove tip-tilt aberrations as well as higher order aberrations.

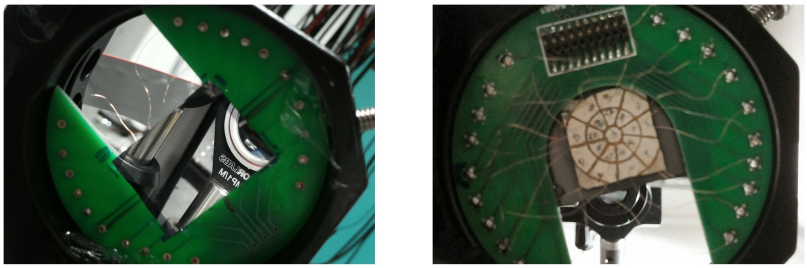

Figure 32: A deformable bimorph mirror with 19 piezoelectric actuators used in the experimental part of this thesis. The faceplate (left) is a sheet of silicon with a thin layer (~ 200μm) of Ag. (right) The piezoelectric actuators are visible.

3.1.5 *Membrane DMs*

The continuous faceplate DMs with force actuators are usually formed by a thin conductive and reflective membrane stretched over a solid flat frame. This membrane can be stretched with the electrodes positioned under it by electrostatic pressure.

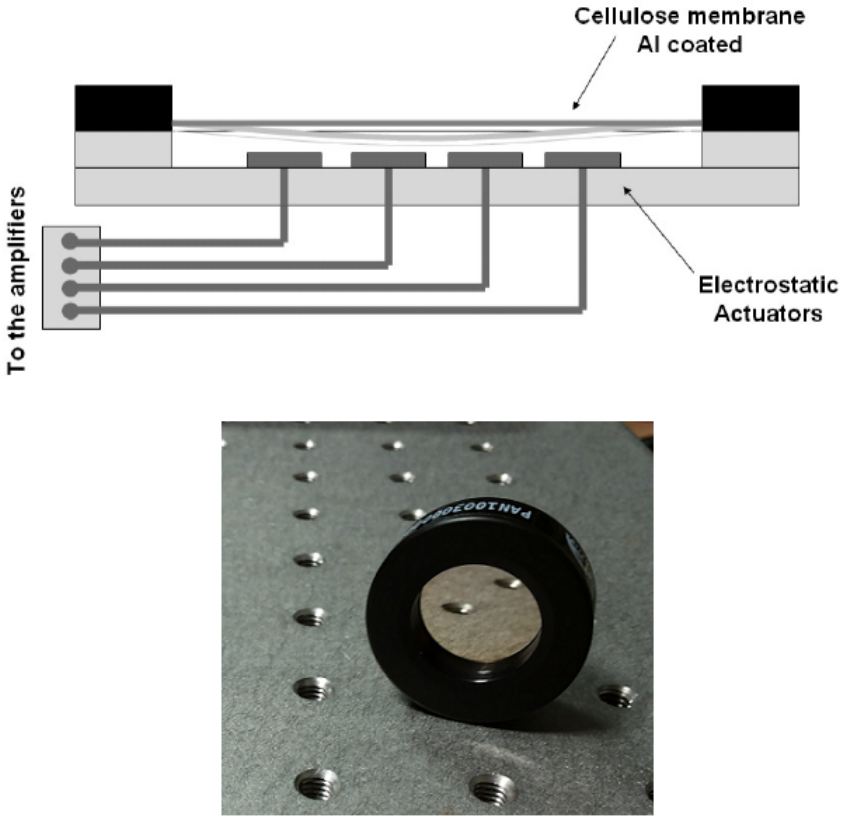

Figure 33: (Top) Simple schematic representation of a membrane DM and (bottom) a membrane DM with 32 electrodes used in the experimental part of this thesis.

The electrostatic pressure P_i exerted on the membrane by the i-th electrode is proportional to the square of the voltage V_i applied on it, that is:

$$P_i = \frac{\epsilon_0}{2}\left(\frac{V_i}{d}\right)^2 \tag{24}$$

where ϵ_0 is the vacuum permittivity and d is the distance between the membrane and the electrodes.

From Eq. 24 is clear that a certain voltage V_i and its negative produce the same deformation on the DM: electrostatic pressure is only attractive. If we want to reproduce positive and negative aberrations, we thus must initially set our DM in the so-called *bias position*, that is, the initial electrostatic pressure of the mirror must be half of the maximum electrostatic pressure that can be applied on it: this can be done setting all the electrodes to a voltage equal to $V_{i,max}/\sqrt{2}$. In this way we can generate both positive and negative aberration, remembering that the relation between the control commands (voltage) and the deformation (electrostatic pressure) is quadratic as described in Eq.24.

3.1.6 *MEMs (micro-electro-mechanical system) DMs*

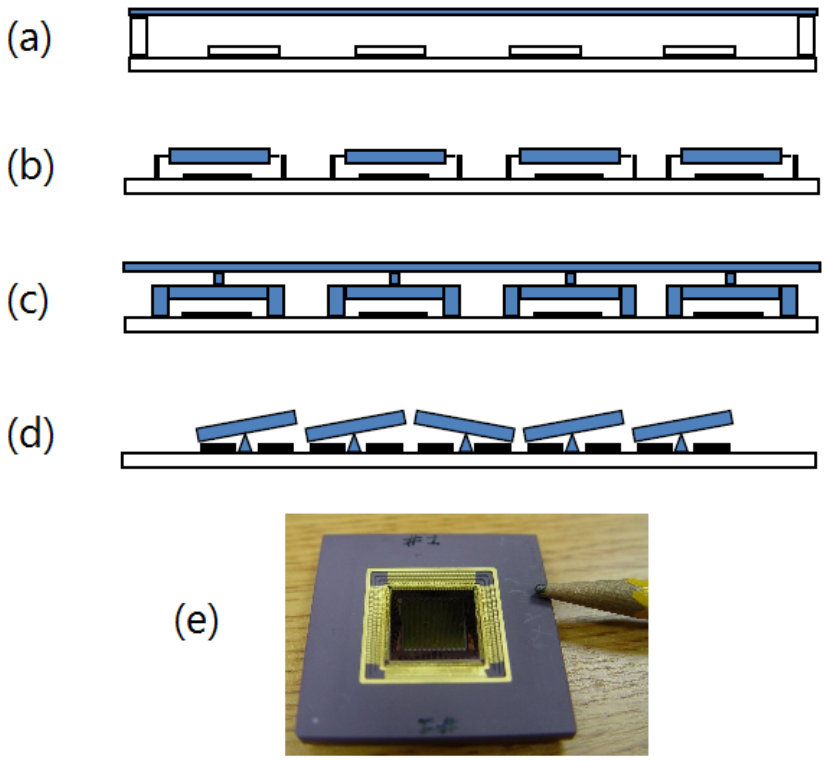

Figure 34: Four different types of MEMs deformable mirrors are shown. (a) Delft University (OKO): array of electrodes under a continue metallic membrane. (b) JPL, SY Tech., AFIT: micromachined segmented surface with an array of microlenses that improves the detection efficiency. (c) Boston University: micromachined surface connected to a membrane continuous mirror. (d) Texas Instruments: micromachined segmented surface with tip-tilt actuators only, used in digital light processing (DLP) televisions. (e) A 1024 actuators MEMs DM (Boston Micromachines).

MEMs deformable mirrors [45,46,47] are a quite new class of cheap DMs. This devices are derived from the membrane DM concept and can be made with hundreds of actuators, high bandwidths and low hysteresis, and fit into a microchip. They are actuated with electrostatic forces between a thin common electrode membrane that acts also as mirror surface and the electrodes. Modern CMOS microchip manufacturing techniques are used to produce this devices.

MEMs devices have the same basic structures as continuous faceplate DMs or segmented DMs except that:

- they can have diameters of about 1 cm;
- they can have hundreds of actuators, typically more than 300;
- the voltage needed for a stroke of few microns is only $\sim$ 15 V with very low current;

The possibility to integrate this DMs directly with driver circuitry opens up a wide range of uses for Adaptive Optics in medical applications and communications (e.g. A.O. imaging in severe environments and tactical laser weapons).

3.2 WAVEFRONT CORRECTORS: LIQUID CRYSTAL CORRECTORS

Liquid crystals are materials that have an intermediate phase (called *mesophase*) between liquid and crystalline, maintaining some of the ordered characteristics of the crystalline state, while having the flow properties of a liquid. The *mesophase* state occurs because the liquid crystal molecules are polarized in such a way that the intermolecular forces keep them aligned in one direction (this alignment is lost at high temperatures). Their most interesting property is that the molecular structure in the *mesophase* changes when an electric field is applied, producing a change in the refractive index. When a liquid crystal cell is used as *wavefront corrector*, the correction zones are defined by an array of transparent electrodes placed on the windows of the cell: in this way each electrode can produce a local variation of the refractive index, leading to a piston correction. This is also the main limit of these device, that is, they can't correct wavefront tip-tilt aberrations (if a tip-tilt correction is needed, they may be combined with a tip-tilt mirror). The other limit of liquid crystal devices is that they work only with polarized light. On the other hand they can have many advantages, such as small size, high spatial resolution, low-voltage operation no moving parts and low cost.

3.3 WAVEFRONT CORRECTORS: DEFORMABLE LENSES

In the last few years some deformable lenses (DLs) has been developed to perform wavefront correction. DLs are very interesting, because in many cases they enable to compact the adaptive optical system, and this is useful in several applications (such as microscopy and vision science). There are a lot of different possibilities to build a deformable lens: here we introduce two different deformable lenses that will be used in our experiments.

3.3.1 *Piezoelectrically actuated DL*

The deformable lens used in almost all of the experiments of this thesis is a prototype DL composed of two thin glass windows (borosilicate glass, refractive index $n \simeq 1.474$, 150μm thick), upon each of which is mounted a piezoelectric actuator ring. The space between the windows is filled with a transparent liquid (Vaseline oil, refractive index $n \simeq 1.475$). The piezoelectric actuator ring (*Physics Instruments*) have an external diameter of 25mm and an internal diameter of 10mm with a thickness of 200μm. Two deformable lenses of this type were used, one with 8 independent actuators per ring and one with 9 (i.e., the first deformable lens has 16 piezoelectric actuators, the second one 18). The rings are glued to the windows and act as a bimorph actuator: therefore the application of a voltage generates a bending of the glass window. The actuators can be controlled using an high voltage (+/- 125 V) driver (*Adaptica srl*, IO64).

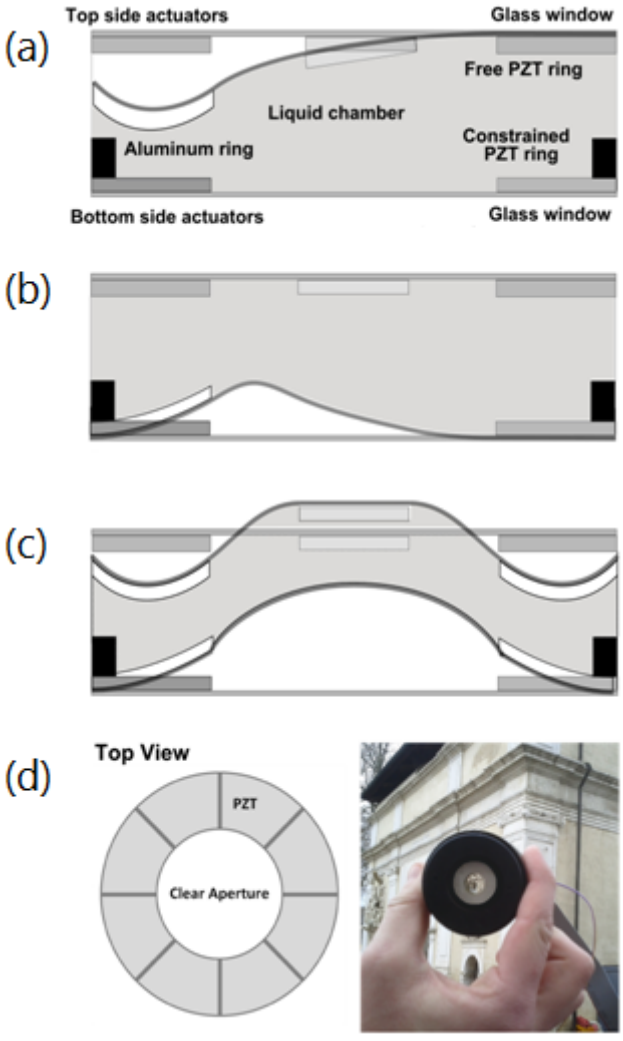

Figure 35: Layout of the deformable lens. The figures shows what happens if we actuate (a) one electrode on the top window, (b) one electrode on the bottom window, or (c) all the actuators with the same voltage value. Panel (d) shows a top view of the PZT actuator ring and a photo of the DL where the lens is mounted in a 2 inches tube mount.

The actuators generate different effects on the top and on the bottom window: this happens because the top window is glued to an

elastomer foam and it is free to move, while the bottom window is blocked at its border by a rigid aluminium ring. This constraint moves the maximum (or the minimum) of the deformation inside the clear aperture (see Figure 35 (b)). Thus the actuator, although placed outside the clear aperture, acts as it was pushing the window from inside. Furthermore, the shape of the top window is restrained in the center by a glass disc with the same refractive index. Figure 35 (c) shows the effect on the wavefront when a positive voltage is applied to all the actuators: both the windows bend upward, so the resultant wavefront is compensated everywhere in the aperture except in the center, where the glass disc stiffens the window. Therefore the resultant wavefront have a peak in the center (this is the so-called *spherical aberration*).

Clearly this DL suffers from hysteresis (due to the piezoelectric actuators): with a simple experimental setup (Figure 36) we can show this effect.

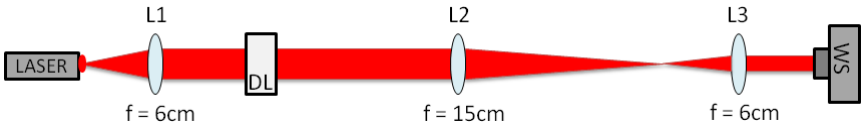

Figure 36: Experimental setup used to evaluate the effects of hysteresis in the piezoelectrically actuated DL described in this paragraph. The light source is a red laser (< 5 mW, $\lambda = 600 \div 700$ nm), and a Shack-Hartmann *wavefront sensor* (described in paragraph 3.4.1) was used to detect the shape of the wavefront. The DL and the *wavefront sensor* are placed in conjugate planes.

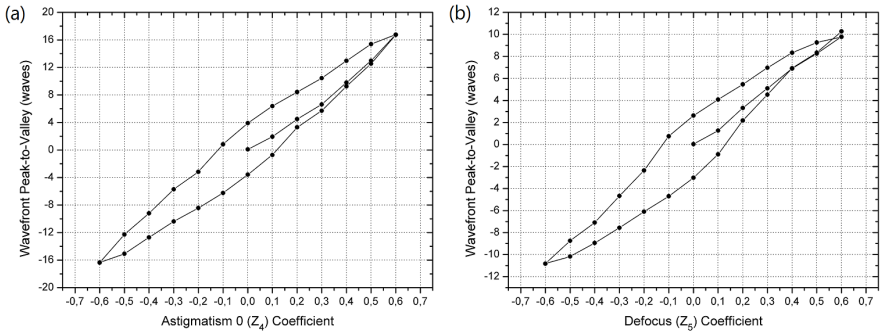

Figure 37: Hysteresis curves for different values of the Zernike coefficients relative to (a) Astigmatism 0 and (b) defocus. The y-axis contains the peak-to-valley measurements of the wavefront in correspondence of the coefficient value sent to the DL. The curves were detected starting from an initial *zero* position with the DL relaxed. Increasing values of the coefficients were sent to the lens (with steps of 0.1) until reaching a coefficient value of 0.6. Then, without relaxing the DL, decreasing values of the coefficients were sent to the lens (with steps of -0.1) until reaching a negative coefficient value of -0.6: this second curve doesn't follow the initial path, and when the *zero* coefficient is sent to the lens, the wavefront isn't flat but has a *positive* peak-to-valley value. Finally, starting from the coefficient value -0.6, increasing values of the coefficients were sent to the lens (with steps of 0.1) until reaching the value 0.6 again: this time, when the *zero* coefficient is sent to the lens, the wavefront has a *negative* peak-to-valley value. The final curves are tipical hystereis curves, as expected.

Astigmatism 0 and *defocus* aberrations (Z_4 and Z_5 Zernike modes respectively) was reproduced with the lens with increasing and then decreasing coefficients. This can be done solving a *linear least squares problem* between the *influence matrix* of the DL and the desired target function (in this case Z_4 or Z_5) in order to find the correct *command vector*. A *linear least squares problem* can be solved with the MATLAB function lsqlin() after selecting the right boundary conditions. The results of these wavefront measurements are shown in Figure 37.

A simple way to relax the DL to the initial deformation after having applied a certain voltage on it, is to perform smaller and smaller hysteresis cycles, until the initial position is finally restored (it's quite simple to implement this relaxation procedure in MATLAB).

Further properties of this DL will be explained in the next chapter.

3.3.2 *Fast electrically tunable DL*

Another useful deformable lens is a DL produced by *Optotune* (model EL-10-30) [58]. It has an external diameter of 30 mm and a clear aperture of 10 mm, and it's 10.75 mm thick. It consists of a container (two thin glass windows with a $400 - 700$ nm broad band), which is filled with a low dispersion transparent liquid (with refractive index $n \simeq 1.300$) and sealed off with an elastic polymer membrane. The deflection of the lens is proportional to the pressure in the fluid.

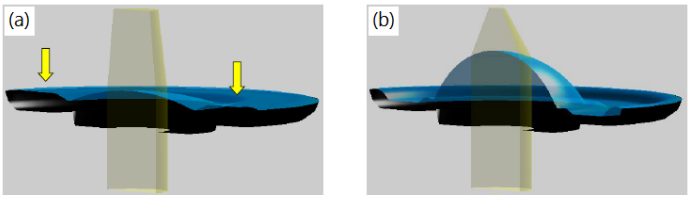

Figure 38: Working principle of the electrically tunable deformable lens. (a) Initially the lens is relaxed, and (b) appliyng a pressure with the electromagnetic actuator it's possible to deform it. The final result is a change of its focal length. This pictures are taken from the manual of the lens, available in the official *Optotune* website [58].

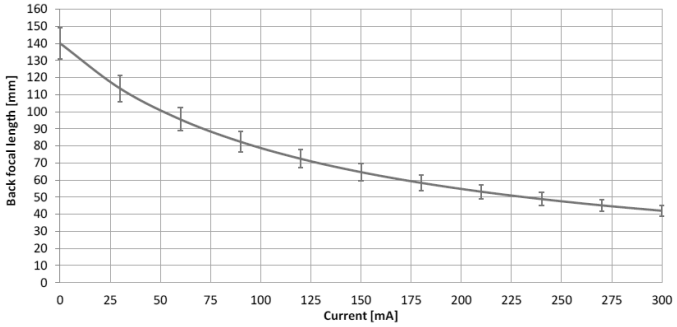

Figure 39: Focal length of the electrically tunable DL against current applied on it (the DC voltage is fixed between 0 and 5 V). The focal length is maximum when the current is zero, and it's equal to $f_{max} \simeq 14$ cm. The minumum focal length $f_{min} \simeq 4.5$ cm is reached when the current is maximum (i.e. 300 mA). Higher values of the current should damage the lens. This graph is taken from the manual of the lens, available in the official *Optotune*'s website.

The DL has a unique electromagnetic actuator that is used to exert pressure on the container: thus, the focal length of the lens is controlled by the current flowing through the coil of the actuator (see Figure 38). The best way to control the electromagnetic actuator is to set a fixed DC voltage between 0 and 5 V and then to control it in current from 0 to ~ 300 mA (in this way we can limit unwanted temperature effects). The focal length changes with the current apply in a way described in Figure 39.

This DL can only change its focal length, that is, it can only correct *defocus* aberrations. Our purpose is to use it in a microscope in order to perform focus and focus stacking without moving the sample.

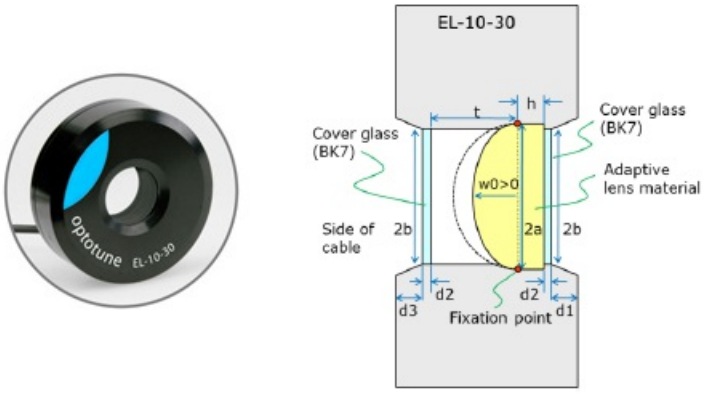

Figure 40: (left) A photo of the EL-10-30 *Optutune* deformable lens and (right) its optical layout. This pictures are taken from the manual of the lens, available in the official *Optotune*'s website.

3.4 WAVEFRONT SENSORS

Anther important device in Adaptive Optics is the *wavefront sensor*. *Wavefront sensors* are very useful not only in closed loop systems, but also in studying and characterising the *wavefront correctors*: we can use a *wavefront sensor* to determine their intrinsic aberrations and their *influence matrix*. There are a lot of different devices in able to do this. We will introduce only three of the most common ones of them [2,5].

3.4.1 *Shack-Hartmann wavefront sensor*

The working principle of the Shack-Hartmann *wavefront sensor* is extremely simple, which may explain its great popularity. An array of identical converging small lenses, called lenslets, is placed in the pupil of the light beam that we want to measure. The original beam is brought to a separate focus by each lenslet, thus producing an array of spots in the focal plane. If the initial wavefront is plane (Figure 41 (top)), each spot will be located on the optical axis of its corresponding lenslet. But if the initial wavefront is distorted (Figure 41 (bottom)), we'll have a local gradient over each lenslet: calling this gradient $\alpha(x, y)$, each spot will be displaced by a distance

$$D(x, y) = \alpha(x, y) \cdot F$$

where F is the focal length of the lenslets. The lenslet array therefore converts wavefront gradients into misurable spot displacements. These displacements are proportional to the wavefront tilts, thus starting from them it's possible to fully reconstruct the wavefront incident on the lenslet array.

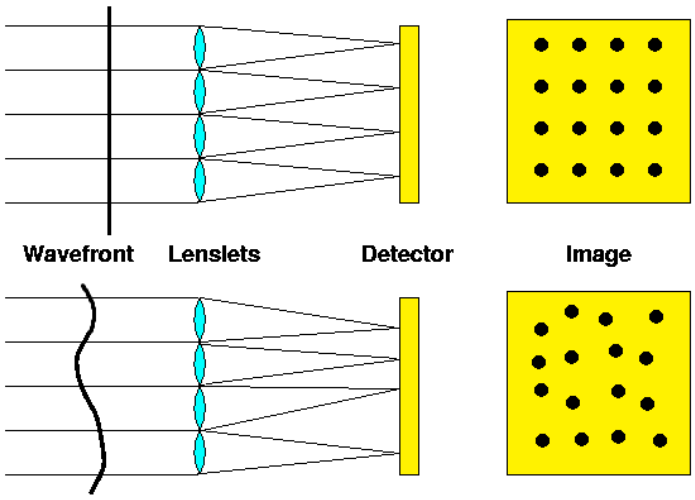

Figure 41: Working principle of a Shack-Hartmann *wavefront sensor*.

The wavefront slope measurement is usually performed with a conventional CCD camera. The simplest arrangement is to use a 2×2 pixel detector for each lenslet (Figure 42). To obtain better linearity and dynamic range, a larger array of 4×4 pixels can be employed.

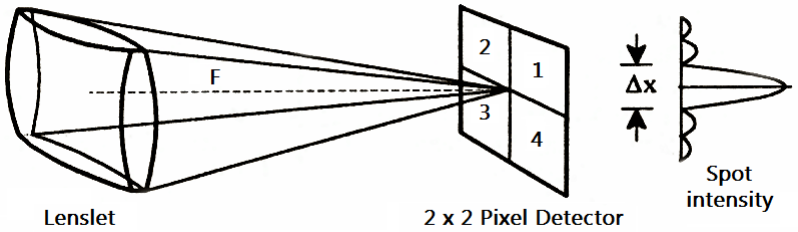

Figure 42: Simple schematic representation of the detection of a light beam passing through a lenslet.

Figure 43: The custom-built Shack-Hartmann *wavefront sensor* used in the experimental part of this thesis.

In the experimental part of this thesi a custom-built Shack-Hartmann *wavefront sensor* was employed (Figure 43). It consists of a monochrome

CMOS camera (*Thorlabs*, DCC1645C) with a 32×32 lenslet array placed in front of it. The lenslet pitch is 300µm and each lenslet has a focal length $F \simeq 14.68$ mm.

3.4.2 *Shearing interferometer wavefront sensor*

Shearing interferometry is a technique for measuring phase differences in a wavefront. The working principle of a shearing interferometer is to combine the wavefront with a laterally shifted (or *sheared*) replica of itself, in order to produce and interference pattern of overlapping copies of the wavefront. In this way, optical phase differences are converted into intensity variations which can be easily detected. This type of interferometers can also work with light sources that are temporally incoherent and of finite size.

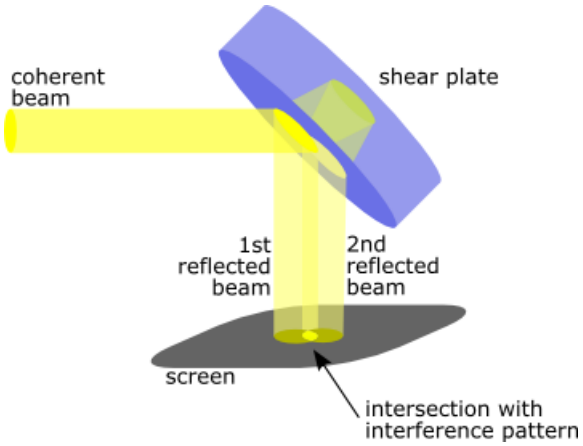

Figure 44: Working principle of a shearing interferometer *wavefront sensor.*

Let's suppose to have a wavefront described by the complex amplitude

$$U(x,y) = A(x,y)e^{ikW(x,y)}$$

where $W(x,y)$ is the wavefront function and $A(x,y)$ its amplitude distribution. If the shear distance s (supposed along the x-axis) is small compared with the scale of the disturbances in the wavefront, we obtain an intensity $I(x,y)$ of the interference pattern described by

$$I(x,y) = 2\left[1 + |A(x,y)|^2 \cos\left(ks\frac{\partial W(x,y)}{\partial x}\right)\right] \tag{25}$$

From Eq.25 we can see that the intensity of the interference pattern is proportional to the cosine of the wavefront slope multiplied by the shear distance. This means that

- changing the shear distance s is possible to adjust the sensitivity of the shearing interferometer;
- measuring the intensity of the interference pattern $I(x,y)$ it's possible to determine the wavefront gradient in the shear direction at any point.

In order to fully reconstruct the wavefront it's clearly necessary to make two lateral shear measurements, one with s along the x-axis and one along the y-axis.

There are several types of shearing interferometers, each one with different specific characteristics. For example, if achromaticity is needed, the shear can be generated with a diffraction grating instead of the plane parallel plates in Figure 44. Furthermore, if we want to measure rotationally simmetric aberrations, such as *defocus* and *spherical aberration*, it might be useful the so-called *radial shear*, where the replica of the wavefront is magnified or demagnified before combining with the original.

Finally, in Figure 45 is shown a shearing interferometer (*Thorlabs*, SI254) [59] used to collimate the laser beams in the experimental setups of Chapters 4,5.

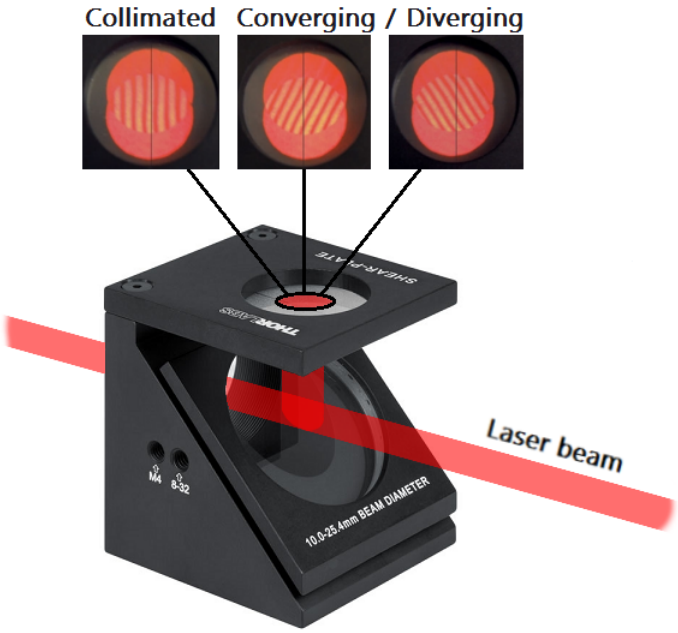

Figure 45: An example of a simple shearing interferometer (*Thorlabs*, SI254) used to collimate laser beams. The three pictures on the top shows how it works for collimated, converging or diverging laser beams. This pictures are taken from the manual of the shearing interferometer, available in the official *Thorlabs* website [59].

3.4.3 *Curvature wavefront sensor*

The curvature *wavefront sensor* was first proposed by F. Roddier in 1988. It consists in an image plane measurement of local wavefront curvature, that is, the second derivative (a.k.a. Laplacian) of the wavefront $\nabla^2 W(\mathbf{r})$, deduced from two specific out-of-focus images (Figure 46). It can be demonstrated that a point by point subtraction of these two images is proportional to the difference between the wavefront curvature term and the partial derivative of the wavefront at the edge and over the direction perpendicular to it:

$$I_1(\mathbf{r}) - I_2(\mathbf{r}) \propto \left[\nabla^2 W(\mathbf{r}) - \left(\frac{\partial W(\mathbf{r})}{\partial \mathbf{n}} \right)_{\mathbf{r}=R} \right] \tag{26}$$

Eq. 25 is based on geometrical optics considerations: to assure its validity, some conditions must be fulfilled. The irradiance distributions I_1 and I_2 are a blurred copy of the pupil, and the blur size

is determined by the diffraction due to the turbulence at the input aperture. If the scalar size of the turbulence is r_0, then the diffraction angle is λ/r_0 and the blur size of I_1 is $\lambda(F-p)/r_0$ (F and p are distances defined in Figure 46). This blur must be smaller than the areas over which we want to measure the curvature, that is, $r_0 p/F$. All these requirements lead to the condition

$$p \geqslant \frac{\lambda F^2}{\lambda F + r_0^2}$$

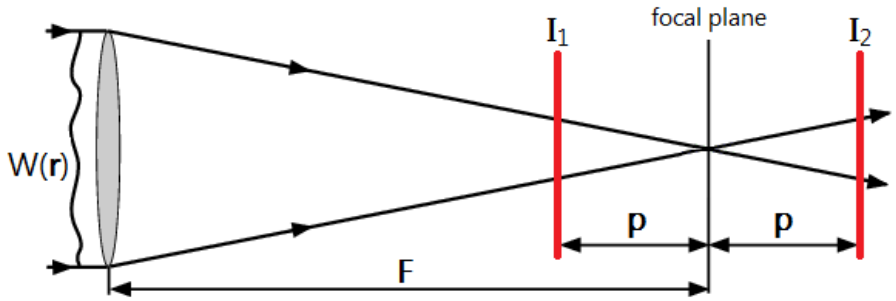

Figure 46: Working principle of a curvature *wavefront sensor*.

A practical implementation of the curvature *wavefront sensor* can be realized using an oscillating membrane mirror that vibrates rapidly (~ 2 kHz) between the two out-of-focus positions. The intensity of the light in each subaperture can then be detected with an *avalanche photodiode* (one per subaperture).
Avalanche photodiodes can detect even individual photons, that is, they have no read noise (so curvature *wavefront sensors* can be used with fainter light sources than other types of *wavefront sensors*), but they are very bulky and expensive, and it's quite hard using a large number of them.

Finally, since curvature *wavefront sensors* directly measure the Laplacian of the wavefront, they are usually coupled with bimorph deformable mirrors in closed loop systems, as they have Laplacian influence functions (and this allows to simplify the aberration correction procedure).

4

EXPERIMENTAL VALIDATIONS

4.1 FIRST EXPERIMENTAL SETUP

All the simulations performed in Chapter 2 of this thesis need to be tested in an experimental setup, with the real Adaptive Optics devices described in Chapter 3. Thus, a simple experimental setup was built on an optical table, which enabled to perform both *closed loop* corrections and *sensorless* corrections. In this way we can directly compare these two approaches. Furthermore the experimental setup is designed also to compare different wavefront correctors, as we will see in the next chapter.

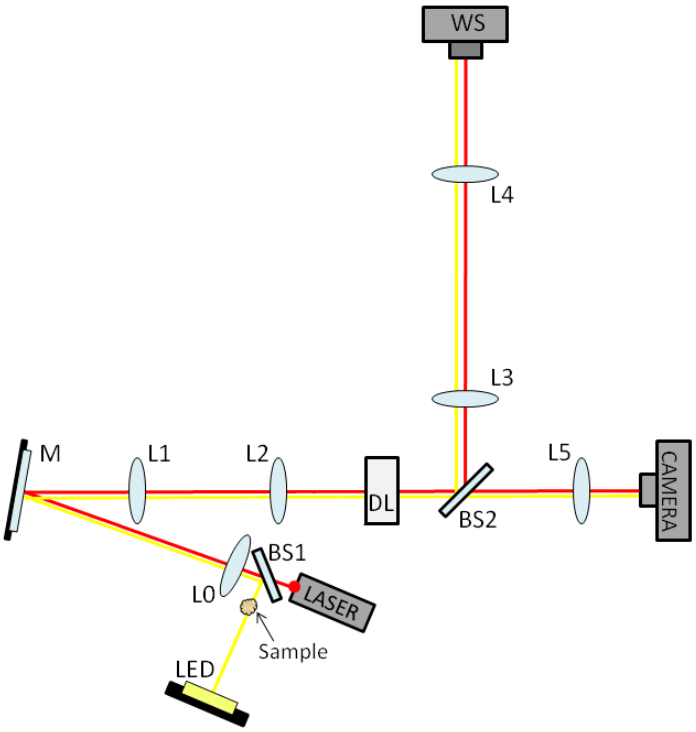

Figure 47: Schematic representation of the experimental setup. There are two sources of illumination: a red laser (< 5 mW, $\lambda = 600 \div 700$ nm, for the measurements with the *wavefront sensor*) and a white LED (for sample illumination). L0 ($f_0 = 6$ cm) collimates the light coming from the sources, L1 and L2 ($f_1 = f_2 = 6$ cm) are two identical achromatic doublets which enable to place the mirror M and the deformable lens DL in conjugate planes (this will be useful especially when we will substitute M with a deformable mirror), BS1 and BS2 are two beamsplitters, L3 ($f_3 = 13$cm) and L4 ($f_4 = 6$ cm) are two achromatic doublets used as beam reducer for the WS (Shack-Hartmann *wavefront sensor*), and finally L5 ($f_5 = 6$ cm) is an achromatic doublet that focalizes the light beams into a colour camera (*Thorlabs*, DCC1645C). The DL and the *wavefront sensor* are in conjugate planes too.

All the lenses used in this setup, which is shown in Figure 47, are *VIS achromatic doublets*, so that aberration corrections of color images can be performed too. The collimation of the beam in each part of the system (where it is required) was verified using the shear interferometer described in paragraph 3.4.2 (see Figure 45) and the alignment of each element with the others was accurately verified using a mobile pinhole. The deformable lens used here is the 16 actuators DL described in paragraph 3.3.1, while the Shack-Hartman *wavefront sensor* is the custom-built one described in paragraph 3.4.1. They are placed in conjugate planes, in order to preserve the diameter of the light beam incident on the *wavefront sensor* while the wavefront is being deformed by the DL.

There are two sources of illumination:

- a red laser (< 5 mW, $\lambda = 600 \div 700$ nm) useful to align the system but especially for the closed loop control (the Shack-Hartmann *wavefront sensor* works only with point-like sources);
- a white LED for sample illumination, useful to perform imaging and sensorless corrections.

4.2 THEORETICAL WAVEFRONTS REPRODUCED BY THE DL

First of all, it has been verified how well the DL can reproduce the various modes (Zernike, Lukosz, O1 and O2).

If we want to reproduce Zernike or Lukosz polynomials without using the *wavefront sensor*, we must find the correct *command vector* for the DL by solving a *linear least squares problem* between the *influence matrix* of the DL and the desired target function (i.e., the polynomial that we want to reproduce). As previously suggested, a *linear least squares problem* can be solved in MATLAB with the function lsqlin().

In the case of O1 and O2 modes, instead, is much easier: the *command vector* is already known by the SVD decomposition. The columns of the matrices $\mathbf{V}$ in Eq.19 and $\mathbf{V}'$ in Eq.22 are none other than the *command vectors* that we are looking for.

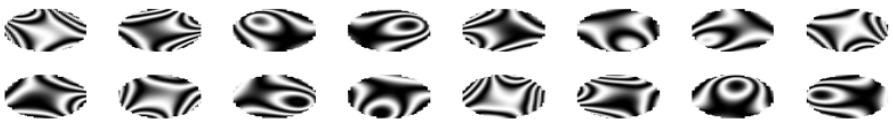

Figure 48: *Influence matrix* of the DL with 16 actuators used in the experimental setup in Figure 47. The deformations produced by each single actuator are shown as *interferograms*.

After implementing some MATLAB programs, all the modes feasible with the deformable lens were reproduced. Each mode was reproduced with increasing peak-to-valley values, until the saturation of one of the actuators (i.e., the maximum value of a certain mode that the DL can reproduce because of its physical limits). The *vector commands* were normalized in such a way that the saturation of one of the actuators, for each mode, occurs in correspondence of a selected coefficient value equal to 1 (or -1 for negative commands). Thus, starting from a coefficient value equal to 0.2 and increasing it with steps of 0.2, and then (after relaxing the DL) starting from -0.2

with steps of -0.2, a total of 10 experimental wavefronts per mode were obtained. The experimental wavefronts were evaluated using the Shack-Hartmann *wavefront sensor*, and then a decomposition of the wavefront was made using modes of the same type of the one reproduced with the DL.

Now, we need a way to quantify the *purity* of the experimental modes, that is, how well they approximate the theoretical modes.

This can be done defining the *Spectral Purity* of the i-th mode as [24]:

$$P_i = \frac{c_i}{\sqrt{\sum_j (c_j)^2}} \tag{27}$$

where c_i is the experimental coefficient of the i-th mode we want to reproduce with the deformable device, while c_j are the values of all the experimental coefficients (including c_i) evaluated from the decomposition of the experimental wavefront.
The *Spectral Purity* P_i can vary from 0 to 1:

- $P_i = 0$ if there isn't any trace of the i-th theoretical mode in the experimental wavefront;
- $P_i = 1$ if the i-th theoretical mode perfectly coincides with the experimental wavefront.

After calculating the *Spectral Purity* of each experimental wavefront, the means of the 10 *Spectral Purities* evaluated for each mode were taken.

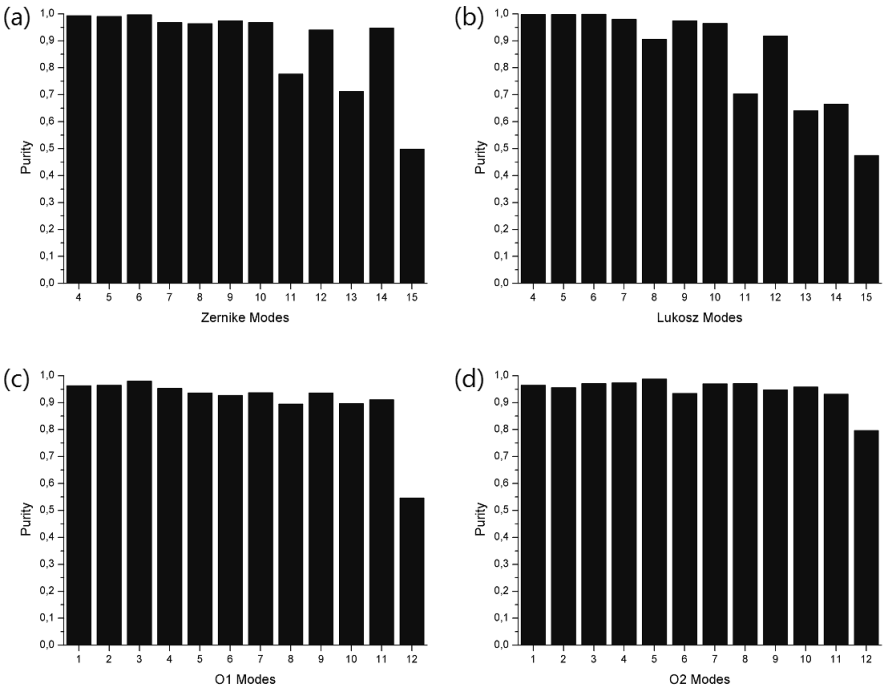

Figure 49: Mean *Spectral Purity* of the experimental wavefronts reproduced by the 16-actuators DL using (a) Zernike modes ($Z_i, i = 1, ..., 15$), (b) Lukosz modes($L_i, i = 1, ..., 15$), (c) O1 modes (from 1 to 12) and (d) O2 modes (from 1 to 12). The modes shown in the histograms are those that the DL can reproduce. Higher modes can't be reproduced by the DL, so it's useless to evaluate their *Spectral Purity*.

The histograms in Figure 49 show the mean *Spectral Purity* for each mode evaluated with the procedure outlined above. From Figure 49 we can notice that

- Zernike and Lukosz modes are well reproduced by the DL, with some difficulties for the *spherical aberration* (mode 13) and the two *quadrafoils* (modes 11 and 15). In particular, mode 15 can't substantially be reproduced (even in closed loop it can't) for both the basis of polynomials.

- O1 and O2 modes are well reproduced by the DL until mode 12, while modes > 12 are not. In the case of O1 modes, also mode 12 can't be reproduced.

4.3 SENSORLESS VS. CLOSED LOOP CORRECTIONS

Once it was known which modes could be reproduced with the deformable lens without using the *wavefront sensor* and which ones couldn't, some sensorless corrections were performed, and then they were compared with the closed loop ones.

To perform closed loop corrections, the laser beam is turned on, and its wavefront is flattened using the feedback from the *wavefront sensor*: then, the laser beam is turned off and we can take the image of the sample corrected.

To perform sensorless corrections, the hysteresis of the DL doesn't allow to take the first image (with the DL relaxed) only one time for the correction of all the modes: each time we find a correction coefficient for a mode, we need to apply the deformation corresponding to that correction immediately, because only in this way we can follow the hysteresis curve. So every time we change the mode we want to correct, we need to take also the image with a zero value of the new mode considered. Using for example 3 image evaluations for every mode, this will take a total of 3N (N = number of modes to be corrected) instead of $2N + 1$ image evaluations, but this is fundamental to avoid problems due to the hysteresis.

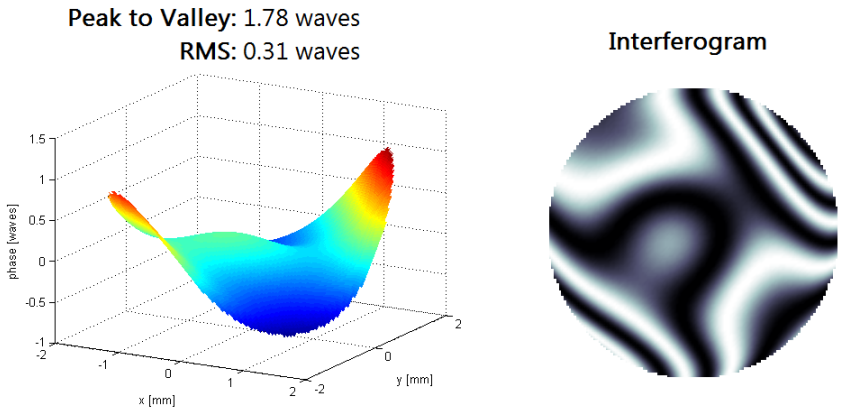

Figure 50: (left) Aberration of the wavefront due to the optical system plus the 16-actuators DL relaxed. The resulting wavefront have a peak-to-valley = 1.78 waves and an rms = 0.31 waves. (right) The interferogram is also shown.

The initial aberration of the wavefront is principally due to misalignments and imperfections of the optical components of the system, plus the initial aberration of the deformable lens: it is shown in Figure 50.

A noticeable result obtained with this experimental setup is that, after a closed loop correction, the corrected wavefront measured by the Shack-Hartmann *wavefront sensor* is flat (according with the *Maréchal criterion*), but after a sensorless correction the corrected wavefront measured by the *wavefront sensor* isn't flat (that is, it isn't under the *Maréchal limit*). Nevertheless, the metric evaluations are in favour of the corrections performed with the sensorless method. This result can be clarified assuming that the system is afflicted by *non common path errors*: the laser beam doesn't follow the same path of the light coming from the sample, so it's possible that the two beams are afflicted by different aberrations because of this difference in the optical path. This is not a problem for the sensorless corrections, which don't work with the laser beam.

The *non common path errors* of this experimental setup will be discussed more in detail in the next chapter, in paragraph 5.6.

4.3.1 *Area of correction*

An important thing that we must take into account while performing an aberration correction is the choice of the *area of correction*, that is, the part of the total image taken by the camera that will be corrected. The camera has a resolution of 1280×1024 pixels, and if we use all this area we will have final images only partially corrected (i.e. we'll have some sharp areas but also some blurred ones).

Thus, some aberration corrections were performed (Figure 51), both sensorless and closed loop, varying the *area of correction* in the camera, and they were compared. The sensorless corrections was performed using the *Modes Correction Algorithm* with O2 modes (from 1 to 12) and the SD metric. For every mode, 5 images were taken to find (with a parabolic fit) the correction coefficient of the corresponding mode.

From Figure 51 we can see that all the initial images are improved by the corrections. Furthermore, sensorless corrections enables us to reach a better image quality (in terms of *imaging sharpness metric* value) than close loop corrections performed in the same conditions.

All the closed loop images were taken after that the close loop procedure flattened the wavefront of the laser beam under the *Maréchal limit* (i.e. when the wavefront rms is < 0.08 waves). So it was interesting to verify with the *wavefront sensor* if the wavefront was flat after a sensorless correction performed with a certain *area of correction*.

From the results of these measurements, which are shown in Figure 52, emerges that:

- in spite of the fact that sensorless corrections lead to better metric values than closed loop ones, the wavefronts measured with the *wavefront sensor* have an rms that in the best case is equal to ~ 0.12 waves: this is clearly a result due to *non common path errors* between the paths of the laser beam and the light from the sample;

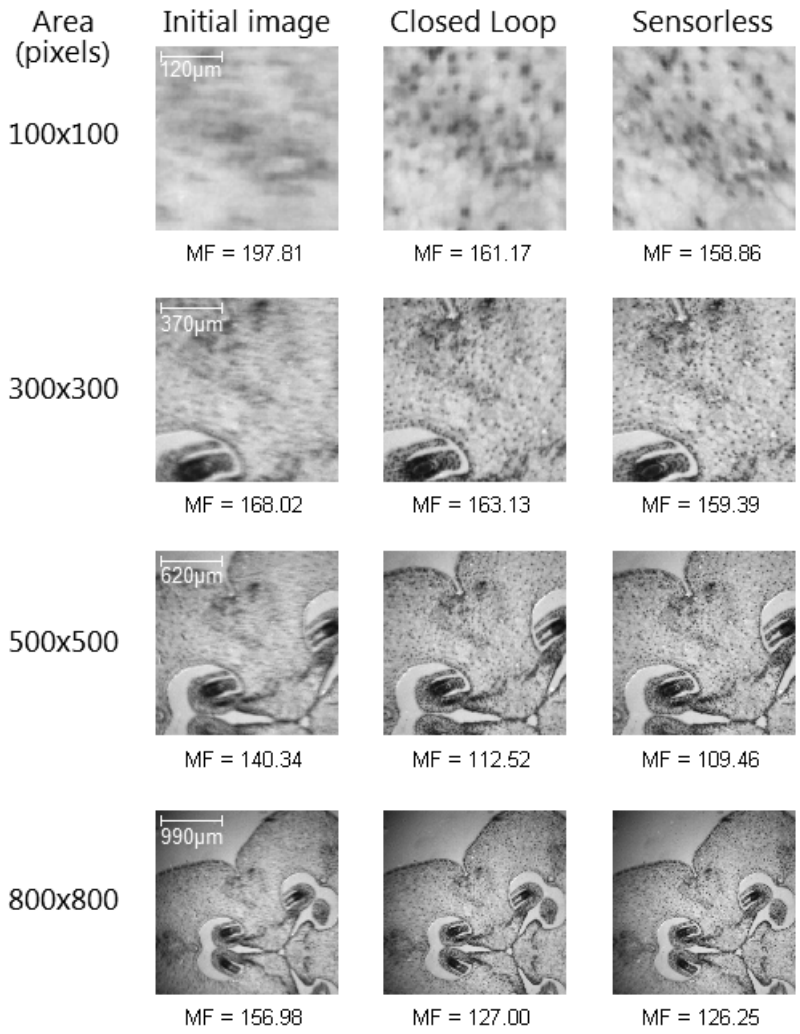

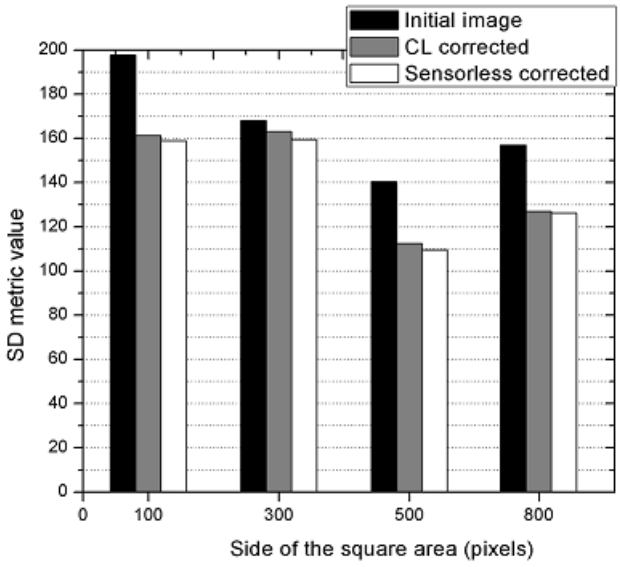

Figure 51: Initial aberrated images (aberration shown in Figure 50), closed loop corrected and sensorless corrected images of the same sample (a lily ovary) for different dimensions of the *area of correction* (that is always taken in the central part of the total image). The values of the SD metric (with $(M_1, M_2) = (0.03, 0.1)$) of each image is provided under it and also reported in an histogram (the lower this value is, the better the quality of the image).

- the flattest wavefronts are those found with an intermediate *area of correction*. This was to be expected, because for small *areas of correction* we have a lack of information that doesn't allow us to perform a good correction, while for big *areas of correction* the difficulties for the deformable device to correct all the area are amplified, and in addition the *wavefront sensor* doesn't work in a correct way because it is thinked to work only with point like sources, but this is not the case if we consider a large area of the sample in the imaging process.

In our system, a good *area of correction* is between 300×300 and 400×400 pixels. This choice allows to perform good aberration corrections and to compare in the best way closed loop and sensorless corrections.

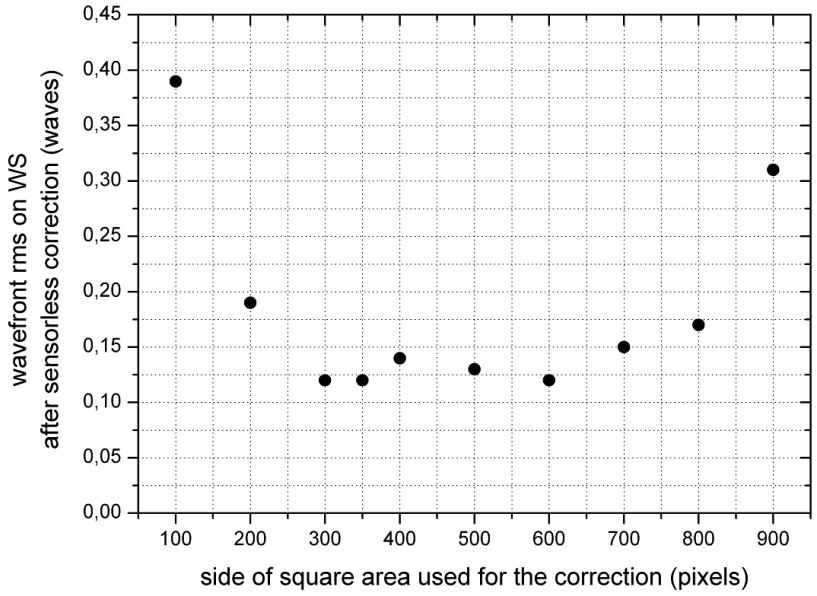

Figure 52: Wavefront rms measured by the *wavefront sensor* after a sensorless correction (described in this paragraph) against the side of the square area used as *area of correction*. These measurements were performed more than a time, in order to verify the sability and reliability of the rms values of the wavefronts, and all the times the sames results were found.

4.3.2 *Comparing metrics and modes in the Modes Correction Algorithm*

Using the results discussed on the previous paragraph, an *area of correction* of 300×300 pixels was setted and then different combinations of modes and metrics were tried with the same sample and the optical system in the same initial conditions.

First of all, some sensorless corrections were performed using the SD metric and the O2 modes, varying the number of points used in the fit for each mode (see Figure 10 in Chapter 1). This is useful to understand if a 3-points fit is sufficient in a real system or if it's better to use more points. In the simulations, using 3 or more points were the same, but there wasn't any kind of noise. After performing several corrections, it can be realized that the number of points that leads to the best metric value is 5.

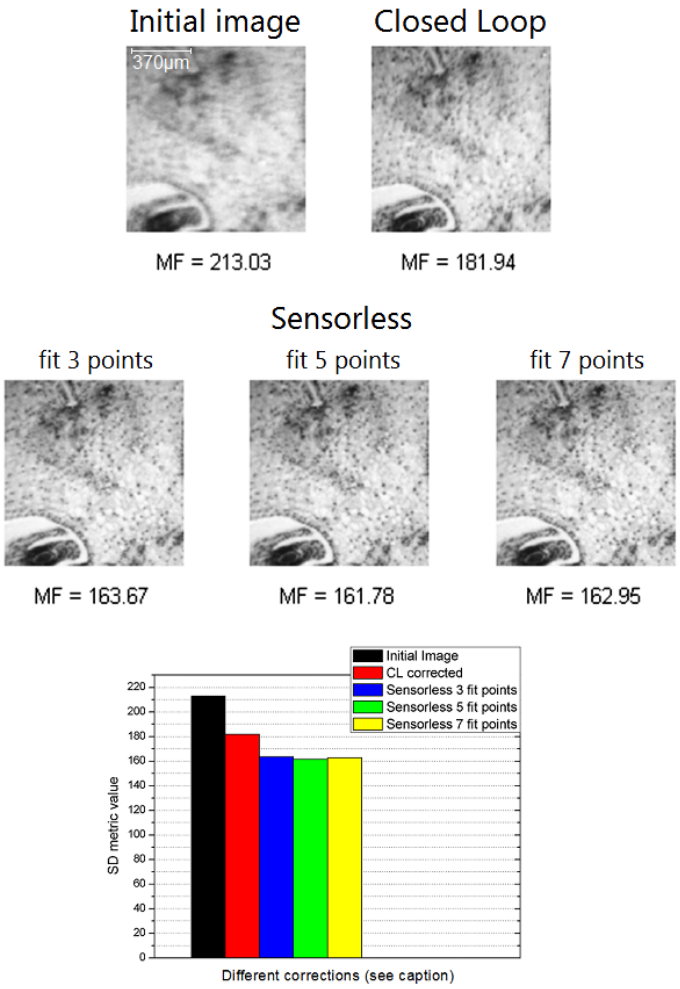

Figure 53: Initial aberrated image (aberration shown in Figure 50), closed loop and sensorless corrected images of the same sample (a lily ovary) with different number of fit points per mode used in the *Modes Correction Algorithm* (first 12 O2 modes, SD metric with $(M_1, M_2) = (0.03, 0.1)$. The value of the SD metric of each image is provided under it and also reported in an histogram (the lower this value is, the better the quality of the image).

An example of these corrections is shown in 53, where the same aberrated image was corrected with a *Mode Correction Algorithm* using 3, 5 and 7 fit points per mode. In all the cases, we also see that the sensorless corrections are better than the closed loop one.

Secondly, several sensorless correction were performed using the *Mode Correction Algorithm* with Zernike, Lukosz, O1 and O2 modes (all those that the lens can reproduce), using both IQ and SD metric. For the IQ metric, a polynomial of degree 4 was used to fit 5 points per mode: in this way the same number of fit points per mode was used with both the metrics. These results are shown in Figure 54

As it can be seen, the lowest metric values are found with the SD metric using Lukosz and O2 modes, according with the simulations. All the corrections are in each case good, and once again all of them are better than the closed loop one. Furthermore, Lukosz and O2 corrections lead to quite the same results (at least in terms of SD metric values).

The experiments are thus consistent with the theory and the simulations.

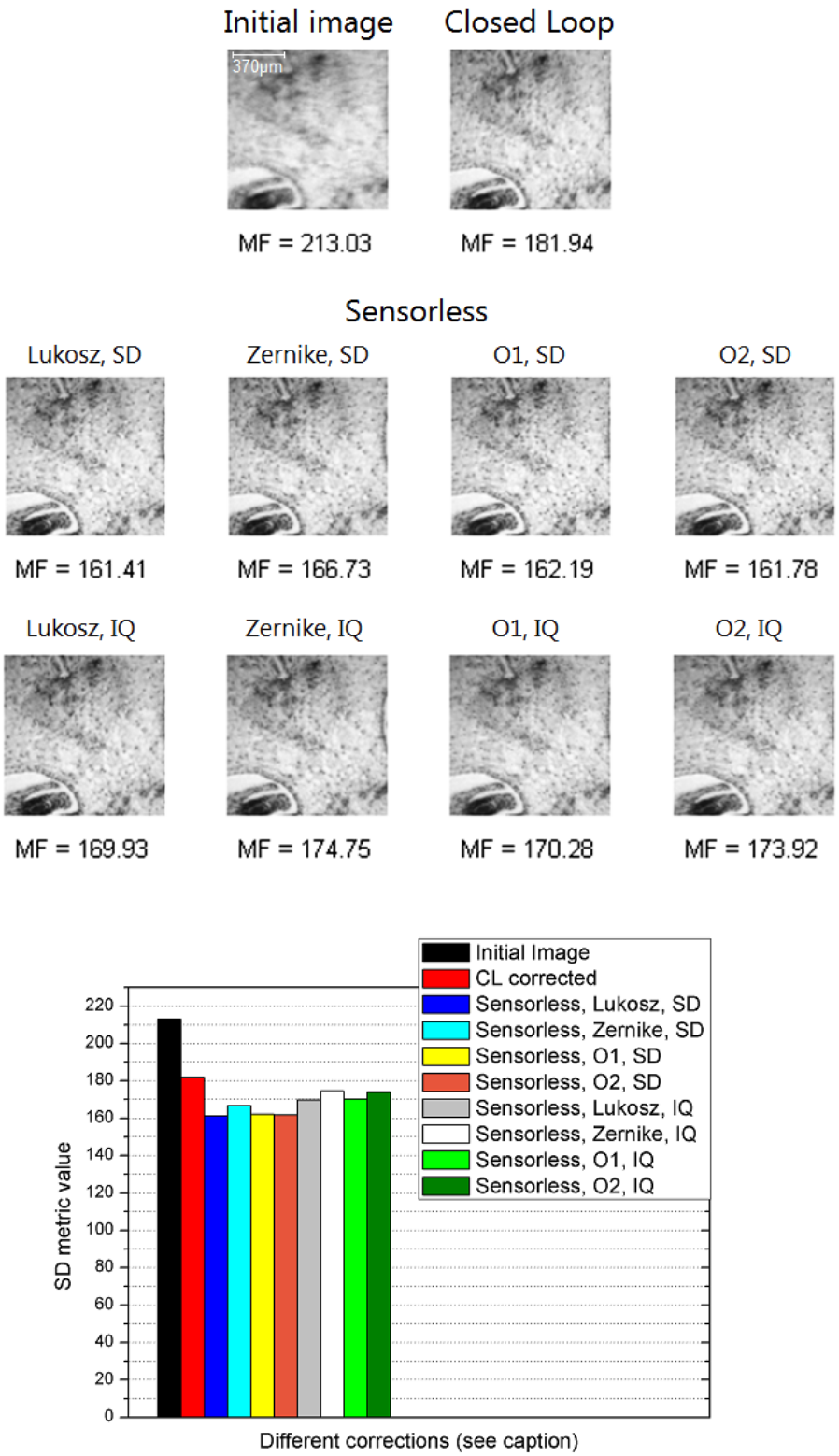

Figure 54: Initial aberrated image (aberration shown in Figure 50), closed loop and sensorless corrected images of the same sample (a lily ovary) with different combinations of metrics and modes (outlined on the top of each image) used in the *Modes Correction Algorithm*. The value of the SD metric (with $(M_1, M_2) = (0.03, 0.1)$) of each image is provided under it, also for the images corrected with the IQ metric (the lower this value is, the better the quality of the image): this enables us to directly compare all the images. All the SD metric values are also reported and also reported in an histogram below the images.

4.3.3 *Coloured sample*

Being the optical system all composed of achromatic doublets, a closed-loop and a sensorless correction were performed also with a different coloured sample (a tilia stem), in order to show that the system can also correct coloured images. For the sensorless correction, the *Modes Correction Algorithm* was used with O2 modes (the first 12) and the SD metric. As we can see from Figure 55, the correction is good.

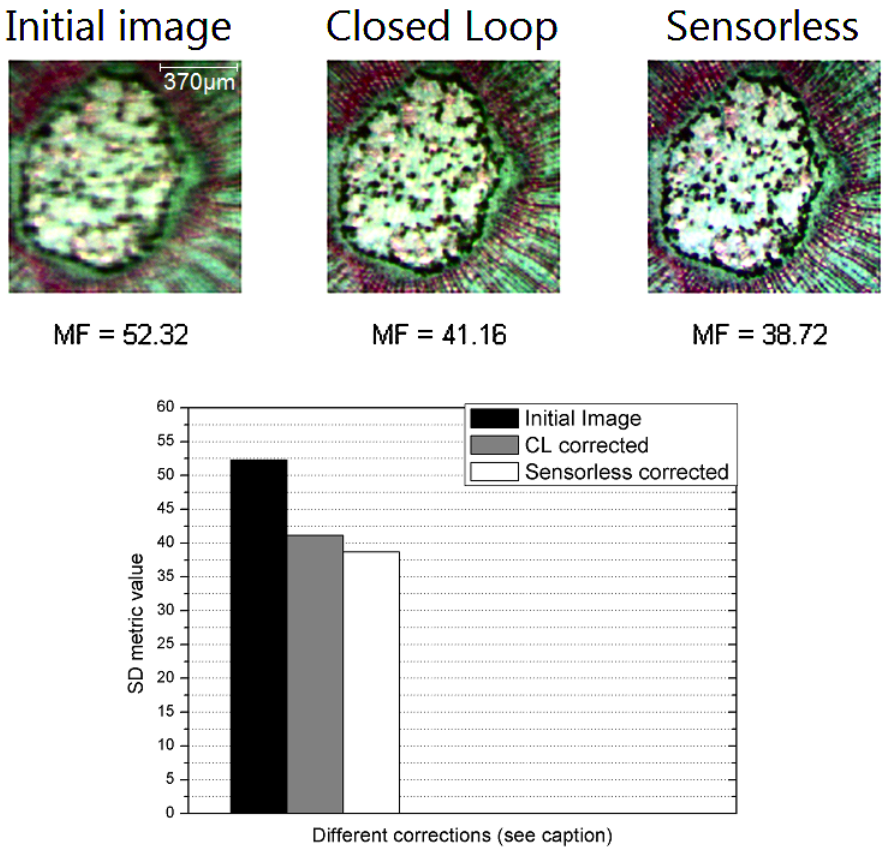

Figure 55: Initial aberrated image (aberration shown in Figure 50), closed loop and sensorless corrected images of a coloured sample (a tilia stem). For the sensorless correction the *Modes Correction Algorithm* was used with O2 modes, SD metric (with $(M_1, M_2) = (0.03, 0.1)$), 5 fit points per mode. The *area of correction*, as for the previous sample, is 300×300 pixels. The value of the SD metric of each image is provided under it and also reported in an histogram (the lower this value is, the better the quality of the image).

5

COMPARISON BETWEEN DIFFERENT DEFORMABLE DEVICES

5.1 SECOND EXPERIMENTAL SETUP

In this chapter two deformable mirrors were compared with a deformable lens with 18 piezoelectric actuators. The DMs have been shown and described in Chapter 2: a piezoelectric DM with 19 actuators (paragraph 3.1.3 and Figure 32) and a membrane DM actuated with 32 electrodes (paragraph 3.1.4 and Figure 33). The new DL lens is perfectly identical to the 16-actuators one, apart from two more actuators: this DL had been developed in parallel with the experiments of this thesis. The additional actuators allows the DL to reproduce also mode 15 (both Zernike and Lukosz one), which the DL couldn't reproduce with only 16 actuators (as it can be seen from Figure 49).

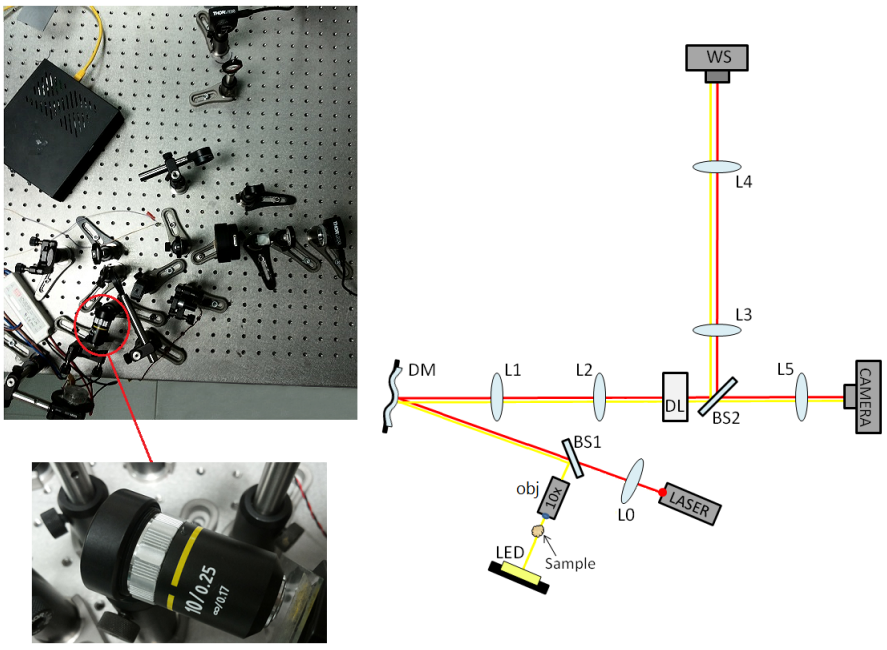

Figure 56: (left) Experimental setup on the optical table and (right) its schematic representation. This setup is similar to that of Figure 47, with two main differences: a 10× objective was used in the imaging path (to improve the quality of the images on the camera), and a DM was used (firstly the DM in Figure 32, and then the DM in Figure 33), replacing the flat mirror of the first experimental setup (Figure 47). The DM, the DL and the Shack-Hartmann *wavefront sensor* are placed in conjugate planes. All the other components are the same of those in Figure 47.

First of all, the *Influence Matrix* (cfr. paragraph 1.6.1) of each deformable device was evaluated using the Shack-Hartmann *wavefront sensor*. These matrices, which are the starting point for the characterisation of our deformable devices, are shown in Figure 57.

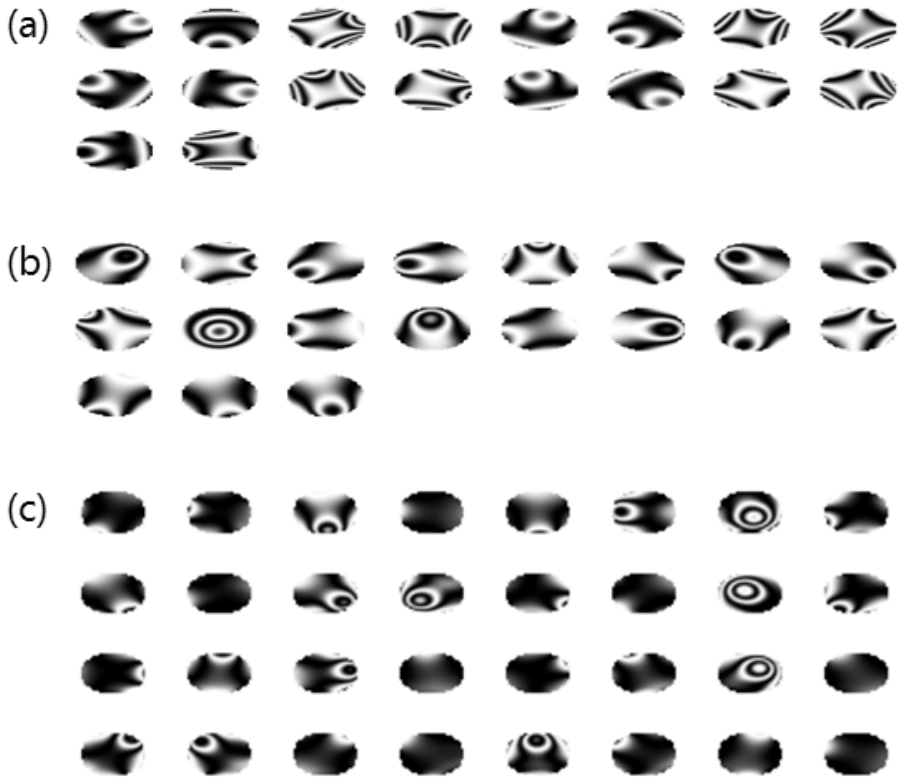

Figure 57: Influence matrices of (a) the 18-actuators DL, (b) the 19-actuators piezoelectric DM and (c) the 32-actuators membrane DM used in the experimental setup in Figure 56. The deformations produced by each sigle actuator are shown as *interferograms*.

5.3 GENERATION OF ZERNIKE POLYNOMIALS

After evaluating the Influence Matrix of the three devices, the closed loop system was used to generate the Zernike polynomials with each one of them. Zernike polynomials were chosen because they are the most commonly used, and thus they are also commonly used to compare deformable devices [48,49].

Setting a desired target (in this case a selected Zernike polynomial) in the closed loop control software, the closed loop system tries to minimize the residual between the selected target and the wavefront generated by the deformable device (detected by the Shack-Hartmann *wavefront sensor*). In this way, we can generate with the deformable devices all the Zernike polynomials that they can reproduce, until the maximum value of wavefront rms (different for each mode) that they can reach.

In order to decide if a certain wavefront can be reproduced or not, the *Maréchal Criterion* was used: according with it, a wavefront can be

reproduced by the device if the residual wavefront between the target wavefront and the measured one has an rms < 0.08 waves.

All the Zernike polynomials that can be generated with the DL and the two DMs are shown in Figure 58, with their maximum rms and peak-to-valley values.

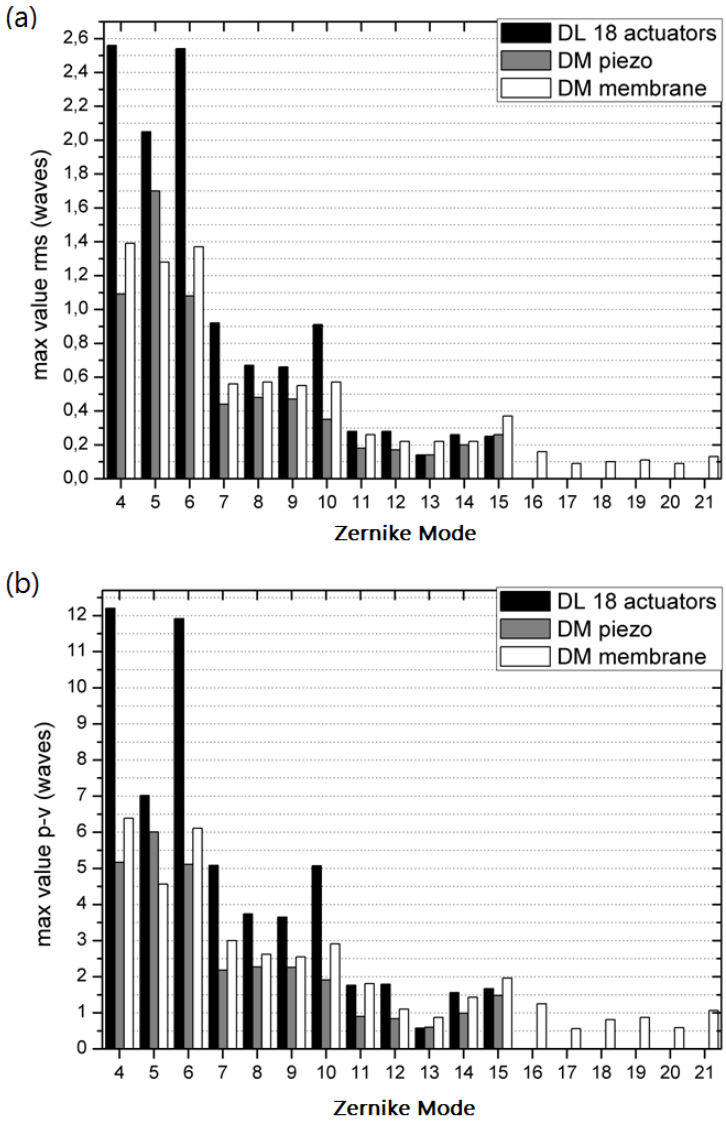

Figure 58: Maximum (a) rms and (b) peak-to-valley values of the Zernike polynomials that can be generated by the 18-actuators DL (black bars), 19-actuators piezoelectric DM (gray bars) and 32-actuators membrane DM (white bars), following the procedure outlined in this paragraph. As it can be noticed, thanks to the two new actuators the DL can now generate also the Zernike mode 15, which couldn't be reproduced with only 16 actuators (see Figure 49).

From the graphs in Figure 58 we can infer that:

- the 18-actuators deformable lens can generate all the Zernike modes between 4 and 15, with a bigger (modes between 4 and 10) or at least equal (modes between 11 and 15) peak-to-valley (and rms) values than those reproducible with the two DMs;
- the 19-actuators piezoelectric DM can generate modes between 4 and 15, all of them with a smaller peak-to-valley (and rms) value than the 32-actuators membrane DM;

- the 32-actuators membrane DM can also generate higher Zernike modes (thanks to its greater number actuators) than the ones reproducible with the other two deformable devices. Indeed, it can generate modes between 4 and 21.

5.4 CLOSED LOOP ABERRATION CORRECTIONS

Once known the ability (and also the limits) of our deformable devices to generate Zernike polynomials, some random aberrations were introduced in the optical system using one of the two DMs, and then the DL was used to correct these aberration in the closed loop system with the laser beam (so this time the target was a flat wavefront). The initial aberration was generated sending to the DM a random *command vector*, with values chosen between the minimum and the maximum value that each actuator can support.

The DL, in addition to the aberrations due to the optical system and to the deformable mirrors, must correct also its own initial aberration. The initial aberration due only to the DL relaxed plus the optical system is shown in Figure 59.

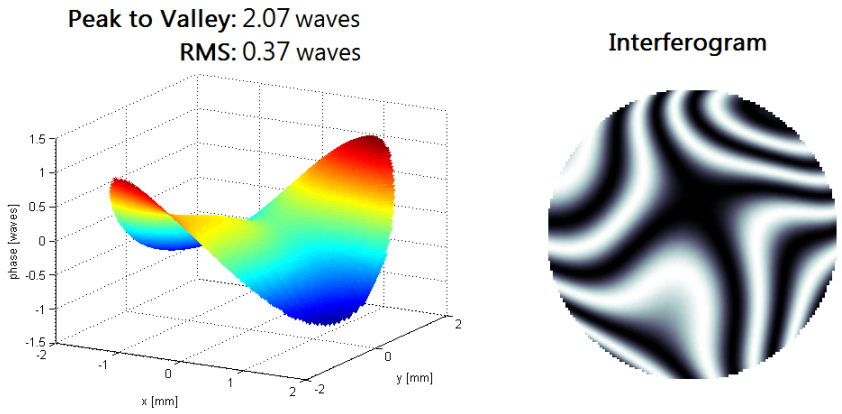

Figure 59: (left) Aberration of the wavefront due to the optical system plus the 18-actuators DL relaxed. The resulting wavefront have a peak-to-valley = 2.07 waves and an rms = 0.37 waves. (right) The interferogram is also shown.

5.4.1 *19-actuators piezoelectric DM vs. 18-actuators DL*

The 19-actuators piezoelectric DM was firstly used to introduce aberrations in the optical system. 20 different initial random aberrations were corrected by the DL using the closed loop system. The results are shown in Figure 60.

As it can be seen, all the 20 initial aberrations are corrected by the DL within the *Maréchal Limit*: this means that the DL is absolutely equivalent to the DM (or even better than it) in correcting aberrations.

Furthermore, all the residual wavefronts of the 20 corrections were decomposed in Zernike polynomials, and then a mean of the residual coefficients related to each mode was performed over all the corrections. From this graph (Figure 61) we can see that the low order (Z_i, $i = 4, ..., 15$) aberrations were corrected, and that the residual aberration is mainly composed of modes higher than mode 15. Those

modes can't be generated by the 19-actuators piezoelectric DM (Figure 58). Nevertheless, all their values are under the *Maréchal Limit*: they might be due to the system itself plus distortions from the DM (or even from the DL, which might generate some high order modes while trying to correct the low order ones).

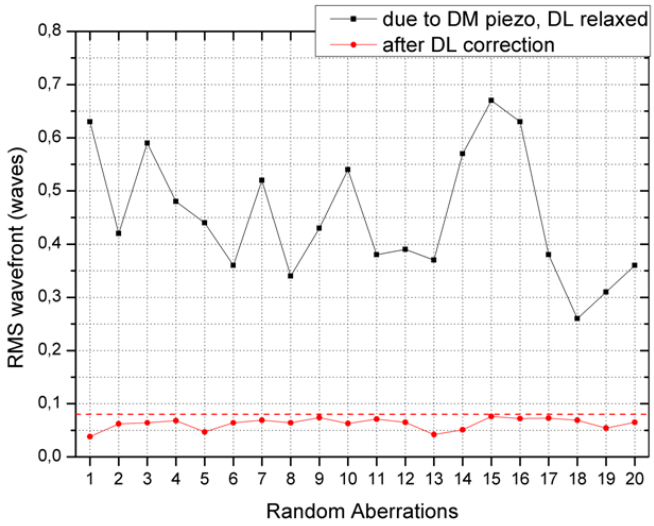

Figure 60: Aberration corrections of 20 random initial aberrations due to the 19-actuators piezoelectric DM and corrected by the 18-actuators DL. The black squares represent the initial aberrations, with a total rms value given in the y-axis, while the red circles are the corresponding final aberrations. The red dashed line represents the *Maréchal Criterion*

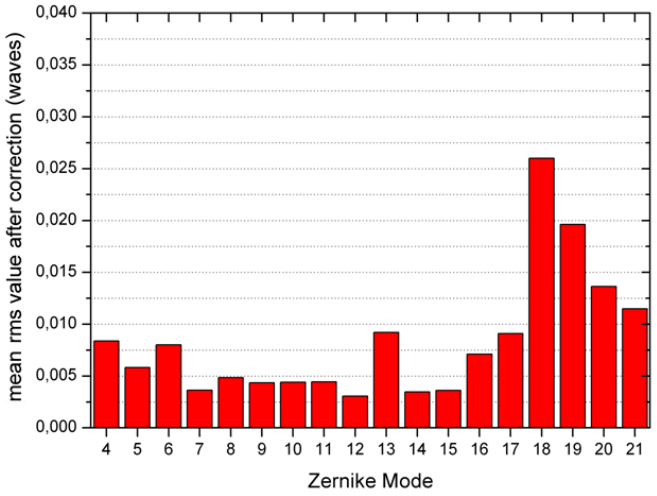

Figure 61: Mean of the coefficients (in waves rms) of the residuals wavefronts after the 20 aberration corrections performed in 60.

5.4.2 *32-actuators membrane DM vs. 18-actuators DL*

The 32-actuators piezoelectric DM was then used (instead of the 19-actuators piezoelectric DM) to introduce aberrations in the optical system. Also with this DM, 20 different initial random aberrations were corrected by the DL using the closed loop system. The results are shown in Figure 62.

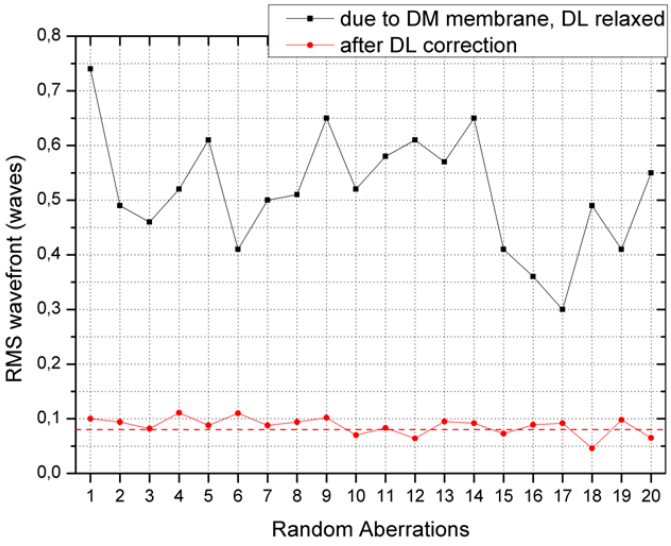

Figure 62: Aberration corrections of 20 random initial aberrations due to the 32-actuators membrane DM and corrected by the 18-actuators DL. The black squares represent the initial aberrations, with a total rms value given in the y-axis, while the red circles are the corresponding final aberrations. The red dashed line represents the *Maréchal Criterion*

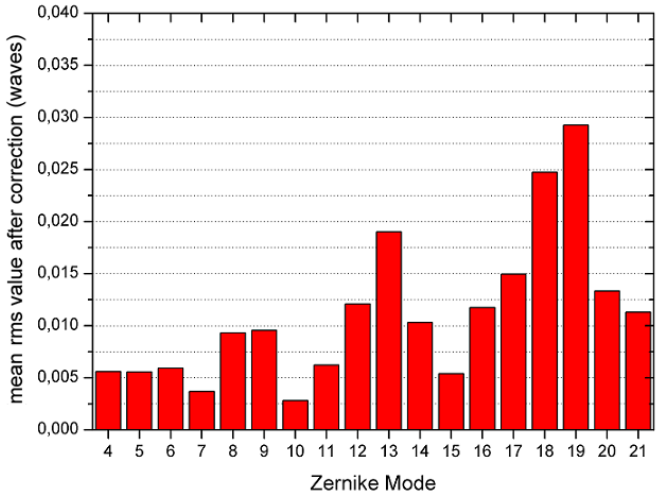

Figure 63: Mean of the coefficients (in waves rms) of the residuals wavefronts after the 20 aberration corrections performed in 62.

This time we can see that the aberrations aren't completely corrected: the majority of them are above, even if quite close, the *Maréchal Limit*. Decomposing the residual wavefront as it has already been done in the analysis in paragraph 5.4.1 (Figure 61) we can see that (Figure 63), also in this case, low order (Z_i, $i = 4, ..., 15$) aberrations were corrected, and that the residual aberration is mainly composed of modes higher than mode 15. In addition, a residual of mode 13 (*spherical aberration*) greater than that found for the 19-actuators piezoelectric DM can be noticed. Nevertheless, this can be understood from the graphs in Figure 58. Finally, the 32-actuators membrane DM can actually generate modes from 16 to 21, so it's obvious that the residual coefficients of these modes must be greater than the same coefficients in the system with the 19-actuators piezoelectric DM.

The *Modes Correction Algorithm* was tested in the experimental setup of Figure 56, and compared with the closed loop correction.

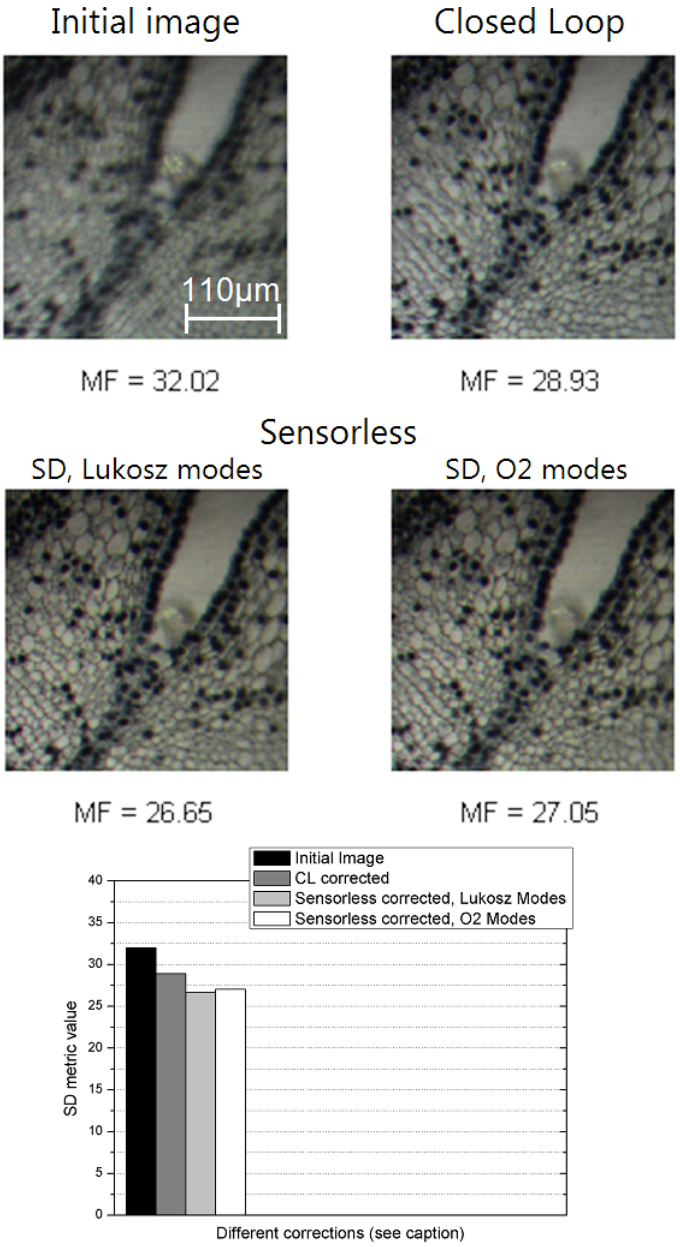

Figure 64: (top left) Initial image: aberration (= 0.56 waves rms) due to the system, the DL relaxed (Figure 59) and the randomly actuated piezoelectric DM. (top right) Closed loop corrected image. (bottom) Sensorless corrected images: *Modes Correction Algorithm*, SD metric with (M_1, M_2) = $(0.03, 0.1)$, using 12 (bottom left) Lukosz modes $(L_i, i = 4, ..., 15)$ or (bottom right) the first 12 O2 modes, 5 fit points per mode. The value of the SD metric of each image is provided under it and also reported in an histogram (the lower this value is, the better the quality of the image).

The sample is the same lily ovary used in Chapter 4. The 19-actuators piezoelectric DM has firstly been used to generate the initial random aberration (= 0.56 waves rms). The corrections are then performed with the 18-actuators DL. The closed loop correction was performed using the laser beam and the Shack Hartman *wavefront sensor* to flatten the wavefront with the DL. The laser was then turned

off and an image of the sample was taken. The sensorless corrections were performed using the *Modes Correction Algorithm* and the SD metric, a correction using 12 Lukosz polynomials ($L_i, i = 4, ..., 15$) and the other with the first 12 O2 modes, in both cases with 5 fit points per mode. All this is shown in Figure 64.

In Figure 65 the values of the SD metric in the 12 steps of each sensorless correction are also shown. We can see that, at each step, the SD metric value decrease, until it reaches the lowest value in the last mode correction.

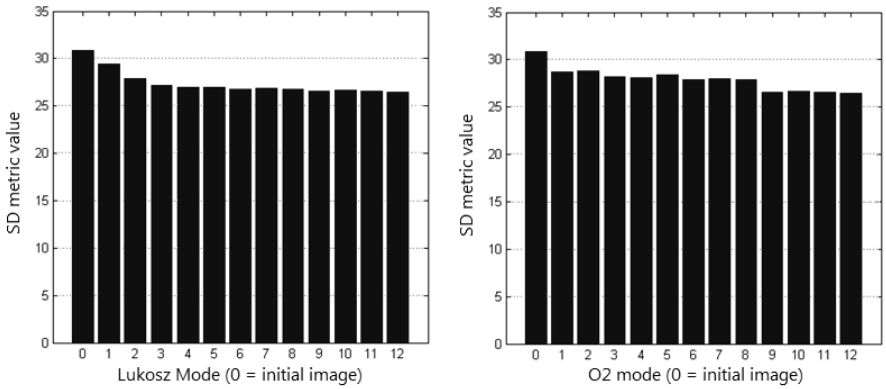

Figure 65: Steps of the sensorless corrections in Figure 64, using (left) Lukosz or (right) O2 modes. The mode 0 on the x-axis in both the graps corresponds to the initial aberration. The y-axis contains the SD metric values, evaluated in the frequencies spatial range $(M_1, M_2) = (0.03, 0.1)$.

The same corrections with a different portion of the same sample were performed using the 32-actuators membrane DM instead of the 19-actuator piezoelectric DM.

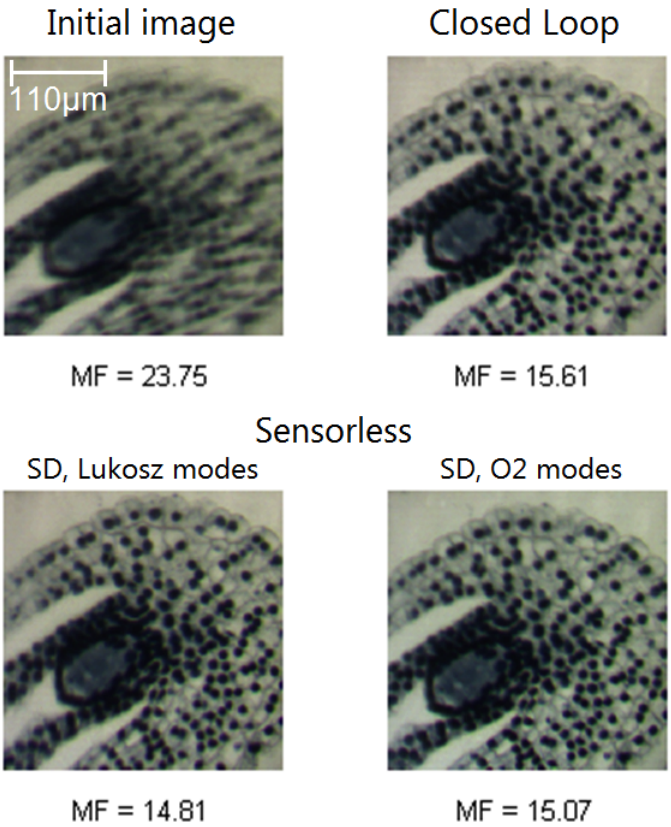

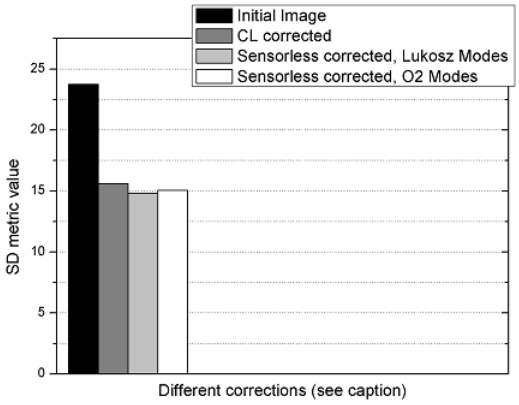

Figure 66: (top left) Initial image: aberration (= 0.94 waves rms) due to the system, the DL relaxed (Figure 59) and the randomly actuated membrane DM. (top right) Closed loop corrected image. (bottom) Sensorless corrected images: *Modes Correction Algorithm*, SD metric with (M_1, M_2) = $(0.03, 0.1)$, using 12 (bottom left) Lukosz modes $(L_i, i = 4, ..., 15)$ or (bottom right) the first 12 O2 modes, 5 fit points per mode. The value of the SD metric of each image is provided under it and also reported in an histogram (the lower this value is, the better the quality of the image).

The initial aberration (= 0.94 waves rms) is larger than the previous one, because the membrane DM can produce broader distortions than the piezoelectric DM (see Figure 58). The initial image and the corrected ones are shown in Figure 66, while the values of the metric in the 12 steps of each sensorless correction can be seen in Figure 67.

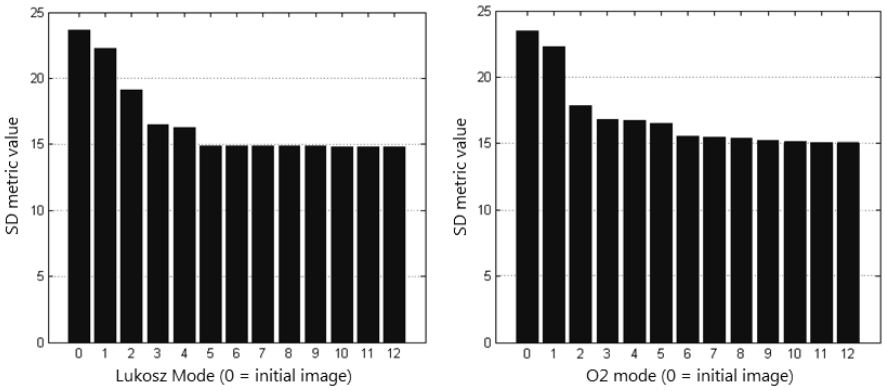

Figure 67: Steps of the sensorless corrections in Figure 66, using (left) Lukosz or (right) O2 modes. The mode 0 on the x-axis in both the graps corresponds to the initial aberration. The y-axis contains the SD metric values, evaluated in the frequencies spatial range (M_1, M_2) = $(0.03, 0.1)$.

In both the cases (Figures 64 and 66), all the corrections are good and the final images are clearly sharper than the initial one. Furthermore, all the sensorless corrections are better than the closed loop ones in terms of SD metric.

5.6 NON COMMON PATH ERRORS

In this last paragraph the effects of the *non common path errors* that affect the closed loop corrections in the experimental setup of Figure 56 are discussed. This phenomenon has already been explained in paragraph 4.3, where it was used to justify the better quality of the

sensorless corrected images compared to the closed loop corrected ones. In this new experimental setup we obtained the same result.

Thus, using the new experimental setup, a random aberration was generated using the 19-actuators piezoelectric mirror, and then the closed loop correction was studied step by step.
After each iteration of the closed loop correction

- an image of the sample was taken, and its SD metric with $(M_1, M_2) = (0.03, 0.1)$ evaluated (Figure 68);
- the rms of the wavefront detected by the Shack-Hartmann *wavefront sensor* was recorded (Figure 69).

If our system wasn't affected by *non common path error*, a decrease in the rms of the wavefront detected by the *wavefront sensor* would also cause a decrease in the SD metric value (i.e. an enhancement in the image quality).

Nevertheless, from Figures 68 and 69 it can be seen that this is not the case. Indeed, while the rms of the wavefront decreases, the quality of the image is increased in the first 3 steps, but then decrease another time. The presence of *non common path errors* is then demonstrated, because it is the only possible explanation for this malfunction in the closed loop system.

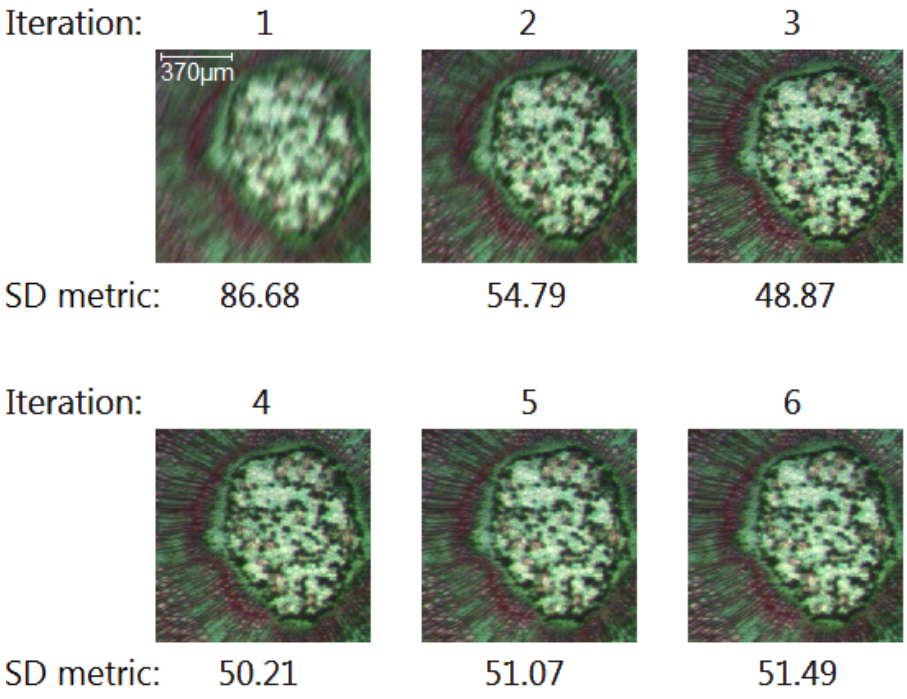

Figure 68: Images of the sample (a tilia stem) shown after each iteration (the first 6) of a closed loop correction obtained with the optical system in Figure 56, with a random aberration generated by the 19-actuators piezoelectric DM (total initial aberration $\simeq 0.66$ waves rms) and the 18-actuators DL used as *wavefront corrector*. The value of the SD metric of each image is provided under it (the lower this value is, the better the quality of the image).

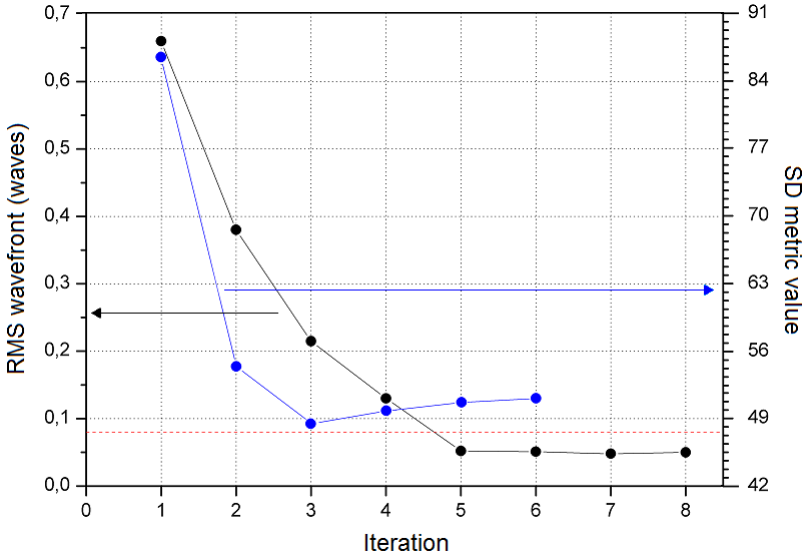

Figure 69: The black dots represent the values of the wavefront rms of the laser beam (left y-axis) detected by the *wavefront sensor* after each iteration (on x-axis) of the closed loop correction. The blue dots represent instead the SD metric values (right y-axis) of the first 6 iterations, which correspond to the 6 images in Figure 68. The red line in the graph represents the *Maréchal Criterion*.

6

SENSORLESS ADAPTIVE OPTICS APPLIED TO CONFOCAL MICROSCOPY

Sensorless Adaptive Optics, and in particular the *Modal Correction Algorithm*, have been already applied successfully in different types of microscopy, including widefield [30], two-photons [14] and confocal [28,56] microscopy. In this chapter all the results reached previously in this thesis has been employed in a confocal microscope.

6.1 DESCRIPTION OF THE MICROSCOPE

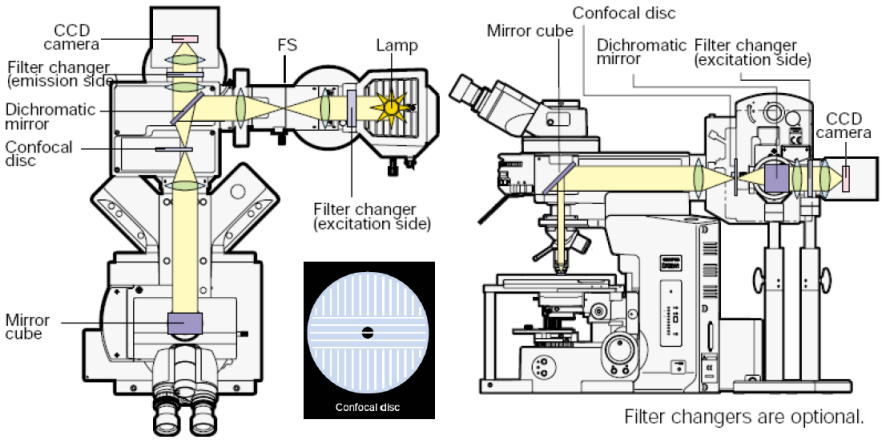

Figure 70: Schematic representations of the Olympus confocal microscope described in this paragraph, also available at `http://www.olympusamerica.com/files/seg_confocal_dsu_bro.pdf`

The confocal microscope used to test the developed algorithms and the 18-actuators piezoelectric deformable lens is schematized in Figure 70.

The light emitted from a LED reflects at a dichroic mirror and passes through a rotary disk placed in the light path. The rotary disk (which is located in a plane conjugate to the focal plane of the objective lens) has a pattern of linear lines that provides the effect equivalent to pin holes by high speed rotation. The light that passes through the disk further passes through the objective lens and goes to the specimen. The fluorescence emitted from the specimen passes through the objective lens again and forms an intermediate image on the rotary disk: a portion of light that is in focus will pass through the disk, so the CCD camera (*Edmund Optics*, EO-3112C) captures the image and a specimen image will be displayed on the monitor of the computer.

The LED which illuminates the sample is a blue high-power led (*Thorlabs*, M470L2) that emits light with nominal wavelength $\lambda = 470$ nm and a bandwidth (FWHM) $\Delta\lambda = 29$ nm. The filter kit is suitable for the FITC Fluorescein, and comprises: an excitation filter (*Edmund Optics*, $67-028$) with a bandpass $\lambda_{ex} = 467 \div 498$ nm, an emission filter (*Edmund Optics*, $67-031$) with a bandpass $\lambda_{em} = 513 \div 556$ nm, and a dichroic mirror (*Edmund Optics*, $67-080$) with a cut-on wavelength $\lambda_{cut} = 506$ nm, a reflection wavelength range $\lambda_R = 440 \div 500$ nm and a transmission wavelength range $\lambda_T = 513 \div 730$.

The disk which enables to obtain the confocal effect is shown in Figure 71. It is about the size of a CD, and has defined slits in it. Approximately half the slits are vertical and half horizontal so that when the disk rotates ($\simeq 2000 \div 6000$ rpm) the lateral resolution is matched in both x-axis and y-axis.

The optimal slit width and the spacing between the slits are related to the objective lenses used and to the thickness of the sample. Typical values of these quantities are listed in the table in Figure 71.

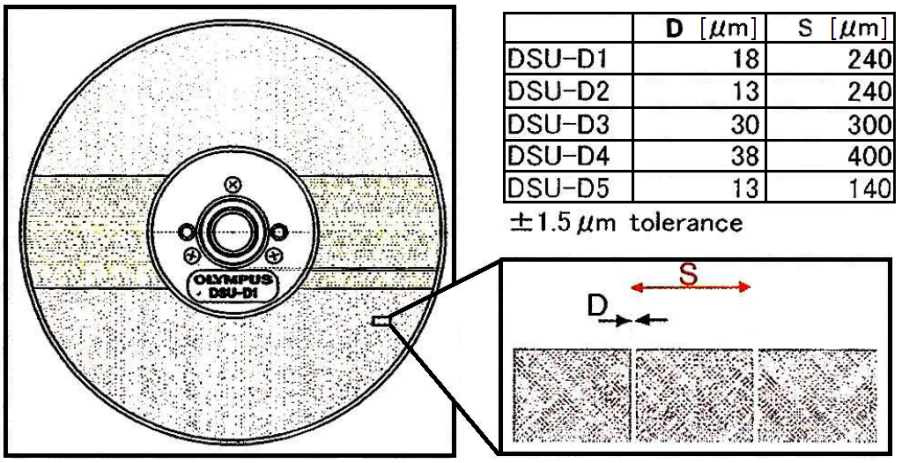

	D [μm]	S [μm]
DSU-D1	18	240
DSU-D2	13	240
DSU-D3	30	300
DSU-D4	38	400
DSU-D5	13	140

±1.5 μm tolerance

Figure 71: Schematic representation of the Olympus slit-based confocal used in the microscope in Figure 70. In the table are described five different disks available: S is the slit width, while D is the spacing between the slits.

6.2 PRACTICAL IMPLEMENTATION OF SENSORLESS AO

The implementation of the 18-actuators piezoelectric DL in the microscope described in the previous paragraph is very simple: the DL can be placed immediately after the objective.

In Figure 72 three photos of the microscope are shown, and in one of them this type of implementation is clearly visible. The mount in which the 18-actuators DL is embedded can also contain further DLs, such as the Optotune's electrically tunable lens described in paragraph 3.3.2. This DL is ideated to change its focal lenght: placing it between the 18-actuators DL and the objective, it's possible to perform focusing and even z-stack into the sample without moving the sample itself.

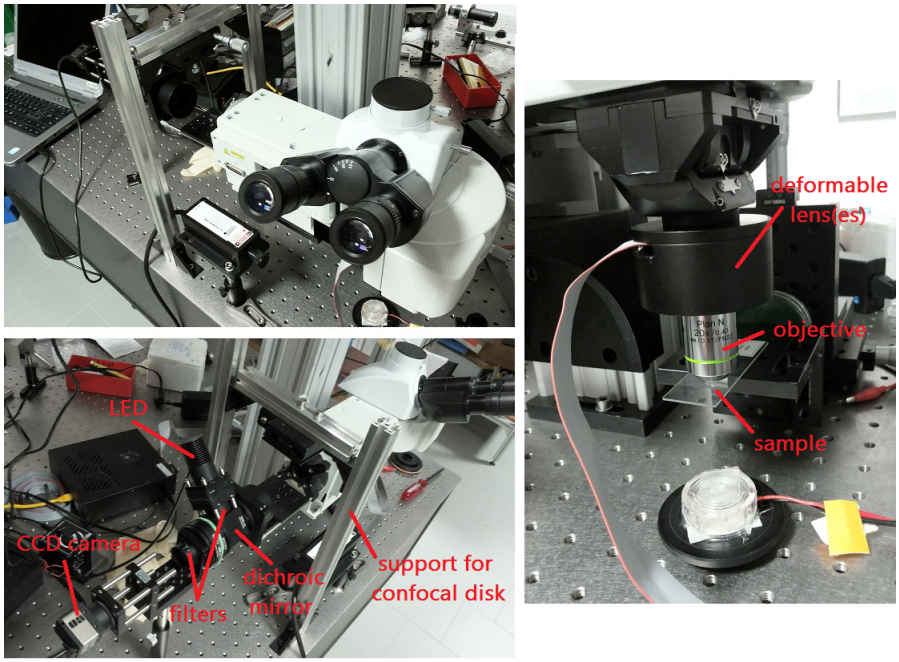

Figure 72: The microscope schematized in Figure 70. Two photos (left) of the microscope from different point of views are shown, and a third (right) showing in detail the implementation of one or more deformable lenses in the light path.

6.3 SENSORLESS ABERRATION CORRECTION OF FLUORESCENT SAMPLES

The microscope was firstly used without the confocal disk, in a simple epi-fluorescence setup, with the 18-actuators DL placed after the objective as shown in Figure 72. In this way we can test the *modes correction algorithm* with some fluorescent samples, that in our case are:

- a *tilia stem* (already used in the previous experimental setups on the optical table) which embodies some fluorescent structures that are ideal for our purposes;
- some fluorescent beads (diameter = 15μm) with excitation and emission wavelengths compatible with the characteristics of our microscope (i.e., those outlined in paragraph 6.1).

Having the microscope almost no aberrations at all, most of the initial aberration is in fact due to the DL itself. In order to add some further aberrations, a thin slice of poor quality glass was placed just above the coverslip of the *tilia stem*, with a drop of water between them: in this way some low order aberrations were introduced in the system. The beads, instead, already manifest some aberrations caused by the matrix in which they are embedded.

The *Modes Correction Algorithm* was thus employed in both the sensorless corrections, using the SD metric in the spatial frequencies range $(M_1, M_2) = (0.03, 0.1)$, 12 Lukosz modes $(L_i, i = 4, ..., 15)$ and 5 fit points per mode. The aberrated images and the corrected ones are shown in Figure 73: from the values of the SD metric before and after the correction and from the profiles in Figure 74 it's clear that the sensorless corrections led to an improvement of the initial images.

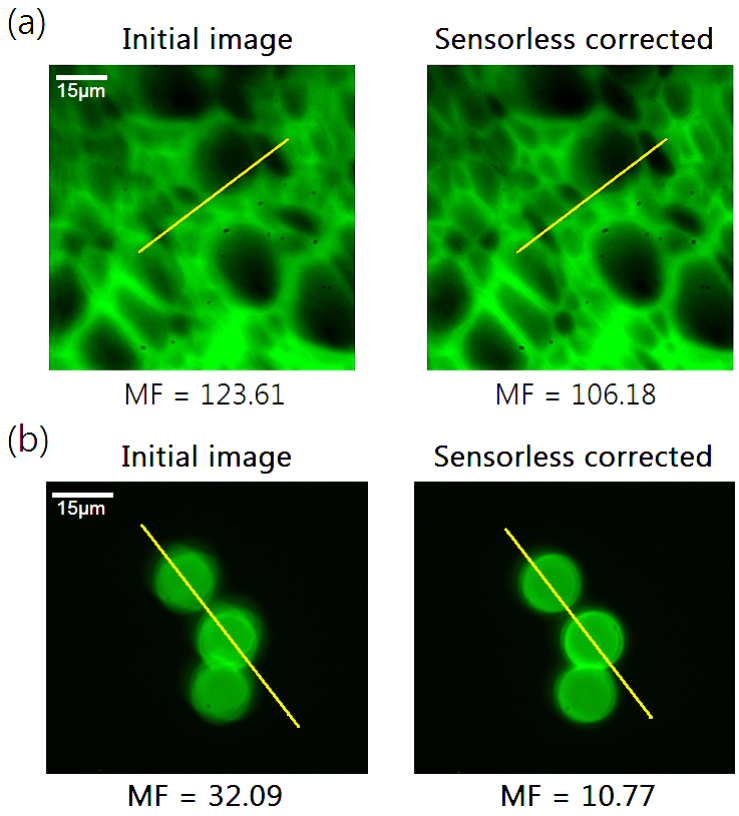

Figure 73: Aberration corrections of fluorescent samples, (a) a tilia stem and (b) three 15-nm fluorescent beads, using the epi-fluorescence setup outlined in this paragraph, with the 18-actuators DL and an Olympus 20x objective visible in Figure 72. (left) The initial aberrated images and (right) the sensorless corrected ones are shown, and the value of the SD metric (with $(M_1, M_2) = (0.03, 0.1)$) of the images is provided under them (the lower this value is, the better the quality of the image). The yellow lines in the images shows the location of the sections plotted in Figures 74 (tilia stem) and 75 (fluorescent beads).

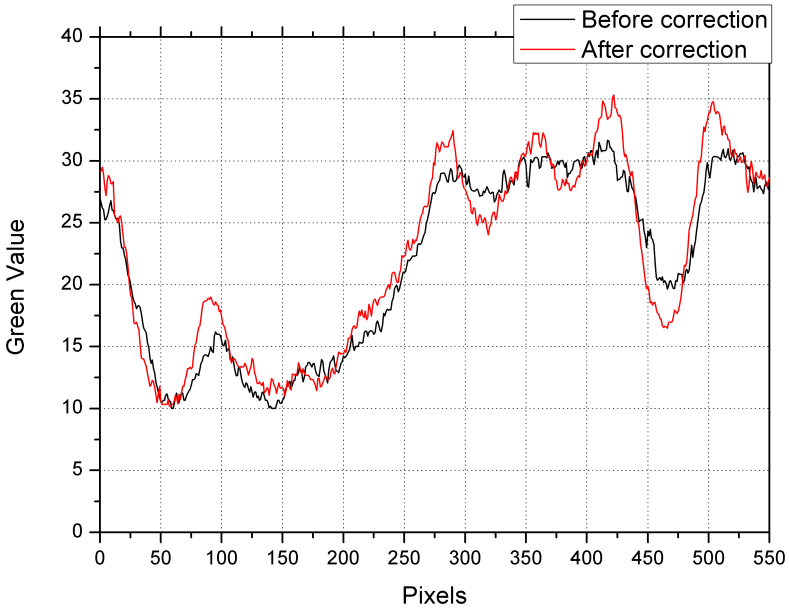

Figure 74: Profile of the sample *tilia stem* before (black line) and after (red line) the sensorless correction. The location of the profile is shown in Figure 73 (a) by the yellow lines. On the y-axis is reported the value of green corresponding to each pixel, being it the unique colour that constitutes the images.

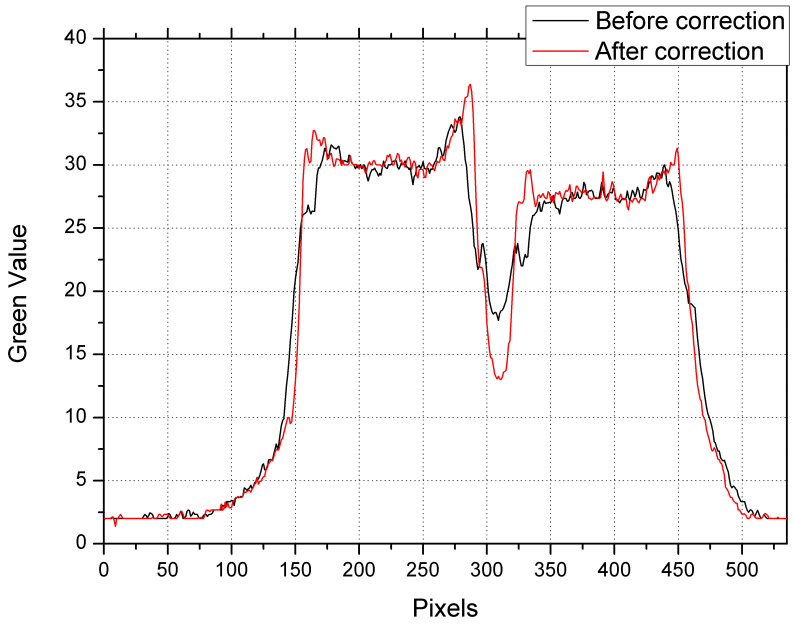

Figure 75: Profile of the sample *fluorescent beads* before (black line) and after (red line) the sensorless correction. The location of the profile is shown in Figure 73 (b) by the yellow lines. On the y-axis is reported the value of green corresponding to each pixel, being it the unique colour that constitutes the images.

6.4 SENSORLESS ABERRATION CORRECTION IN CONFOCAL SETUP

Finally, we want to obtain a sensorless aberration correction with the confocal disk mounted on our microscope, as shown in Figure 76.

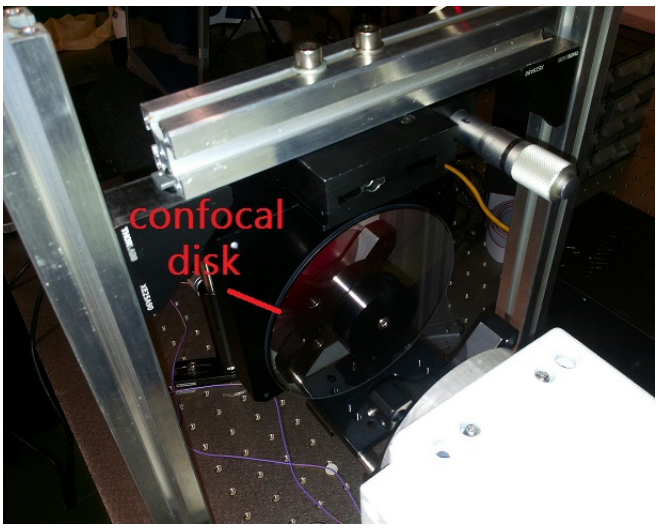

Figure 76: Confocal disk mounted on the microscope in Figures 70, 72. The confocal disk used here has a slit width S = 140µm and a gap between the slits D = 13µm (see Figure 71).

The confocal disk must be placed in a plane conjugate to the focal plane of the objective. This can be checked by removing the emission filter from the microscope (see Figure 70) and watching the blue light reflected from the disk to the camera: we must move the disk back and forth until its slits are in the sharpest focus. The focused slits are shown in Figure 77, and this is the position which enables confocal imaging.

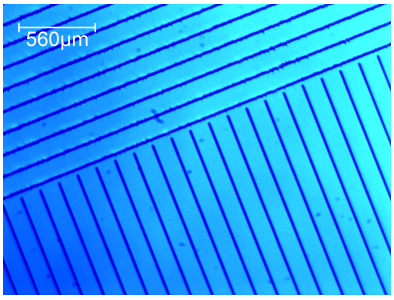

Figure 77: Slits of the confocal disk imaged on the CCD camera by reflection of the blue excitation light incident on it.

It must be taken into account that the total amount of fluorescence light from the sample is now dramatically reduced, because the confocal disk has a transmission of only ~ 10%: this means that, since the light from the blue LED must pass through the disk to reach the sample, and then the fluorescence light emitted by the sample passes another time through the disk, the light incident on the camera is only 1% of the light that would reach the camera in an simple epi-fluorescence setup (i.e. without confocal disk). This fact, in addition to the poor sensibility of our CCD camera, restricts our analysis to strongly fluorescent samples, that is, the *fluorescent beads* used in the previous paragraph (the *tilia stem* doesn't emit enough fluorescence photons to be detected with our CCD camera).

Nevertheless, also with the *fluorescent beads* the confocal images didn't have enough contrast to perform aberration correction with the *Modes Correction Algorithm*, because the images contained too much noise to measure the *imaging sharpness metric* correctly. Thus, an aberration correction was performed with the confocal disk temporarily removed, and then, leaving the DL deformed by the estimated *command vector*, the disk was restored in order to take the corrected confocal image. This procedure, similar to that used in [56], leads to an improvement of the confocal image with respect to the aberrated initial one.

All the *Modes Correction Algorithm* parameters and the initial conditions are the same of those outlined in paragraph 6.3: the only exception was the confocal disk mounted on the microscope when the confocal images were taken.

In Figure 78 (a) the sensorless aberration correction without the confocal disk is shown, while Figure 78 (b) displays the images taken with the confocal disk before and after the sensorless correction.

We can notice that:

- the epi-fluorescent image results improved after the sensorless aberration correction;
- the confocal images are not affected by the out-of-focus light, and this can be seen by the fact that the halo around the beads, visible in the epi-fluorescent setup, now disappears.
- the sensorless aberration correction leads to an improvement also in the confocal image: from the line profiles on Figure 79 we can deduce that the edges of the beads after the correction result sharper than before.

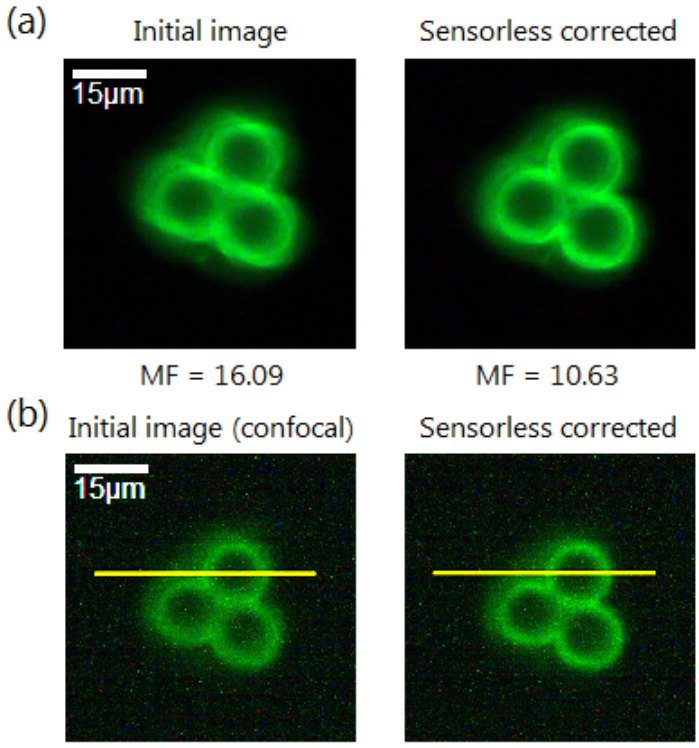

Figure 78: (a) Aberration corrections of three 15-nm fluorescent beads, using the epi-fluorescence setup without the confocal disk, with an Olympus 20x objective. (left) The initial aberrated images and (right) the sensorless corrected ones are shown, and the value of the SD metric (with $(M_1, M_2) = (0.03, 0.1)$) of the images is provided under them (the lower this value is, the better the quality of the image). (b) The same initial and final images were taken with the confocal disk mounted on the microscope. The yellow lines in the confocal images shows the location of the sections plotted in Figure 79.

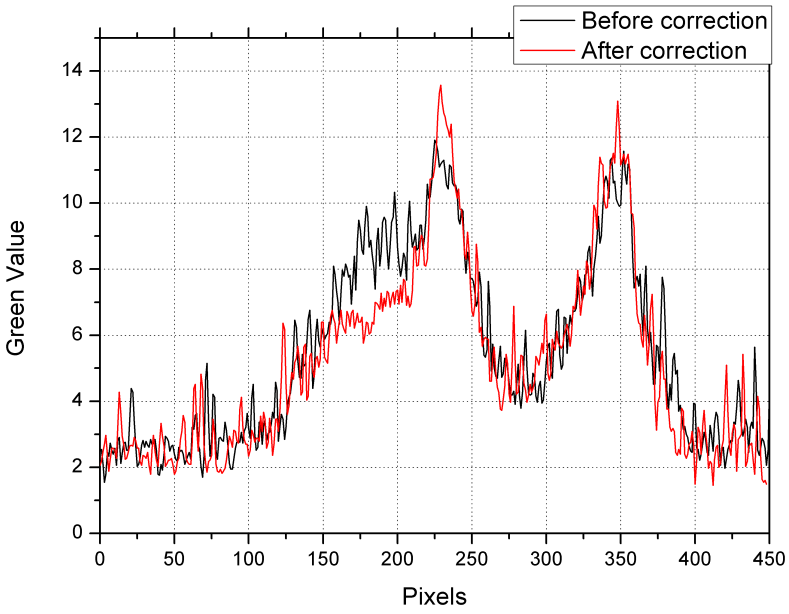

Figure 79: Profile of the confocal images *fluorescent beads* before (black line) and after (red line) the sensorless correction. The location of the profile is shown in Figure 78 (b) by the yellow lines. On the y-axis is reported the value of green corresponding to each pixel, being it the unique colour that constitutes the images.

7

CONCLUSIONS

7.1 RESULTS ACHIEVED

The key results achieved in this thesis can be listed as follows.

- A complete *wavefront sensorless* algorithm has been developed and optimized, comparing different possible choices that can be found in literature.

- In Chapters 1,2 two different metrics based on the irradiance in the image plane, called IQ (Irradiance Squared metric) and SD (Spectral Density metric), have been found to be good *imaging sharpness metrics*, using both Zernike or Lukosz modes to describe the aberration. In particular, the reciprocal of the SD metric (when integrated over the range of low spatial frequencies) is a parabola, which global extremum can be calculated with only 3 metric evaluations per mode.

- The *Modes Correction Algorithm* has been employed in the aberration correction procedure, first in simulations (Chapter 2) and then in real experimental setups (Chapter 4), trying several different combinations of *imaging sharpness metrics* and modes, and it has been shown that the best performances are obtained with the reciprocal of the SD metric minimized using Lukosz modes. This is in line with the theoretical considerations outlined in Chapter 1, because the reciprocal of the SD metric can be approximated with a linear combination of squared Lukosz coefficients, that is, each Lukosz mode can be corrected independently from the others (this property comes directly from the orthonormality law of Lukosz polynomials, which is different from the Zernike polynomials one). Being the *Modes Correction Algorithm* based on the independence between the modes in the evaluation of the global extremum of the metric, the lower the crosstalk between the modes is, the better the performance of the algorithm and the larger the aberrations it can correct.

- In Chapter 2 it has also been shown the possibility to
  1) optimize the order in which the modes are corrected; this optimization depends on the sample (as a general rule, the correction should be applied first to the modes which mainly affect the system and are less affected by crosstalk with other modes);
  2) take multiple iterations of the *Modes Correction Algorithm* in order to correct larger aberrations, up to ~ 3 waves rms

($\lambda = 633$ nm). This value has been demonstrated only in the simulations and is clearly sample-dependent.

- At the end of Chapter 2 it has been demonstrated that the *Modes Correction Algorithm* requires much less metric evaluations (and than much less time) to converge than search algorithms such as the *Nelder-Mead Simplex Algorithm*: for an initial aberration of ~ 0.5 waves rms ($\lambda = 633$ nm), the *Modes Correction Algorithm* needs from 17 (best simulated case, 2N+1) to 40 (our experimetal case, 5N) metric evaluations to correct N=8 modes, while the *Nelder-Mead Simplex Algorithm* needs *several hundreds* of metric evaluations to correct the same modes.

- In Chapters 2,4 the *optimum modes* of a prototype of deformable lens piezoelectrically actuated (described in Chapter 3) have been employed instead of Zernike and Lukosz modes in the *Modes Correction Algorithm*. It has been found that *optimum modes* satisfying a Lukosz-like orthonormality law (called O2 modes) lead to better aberration corrections than *optimum modes* satisfying a Zernike-like orthonormality law (called O1 modes), once a time according with theory.

- In Chapter 4, comparing different combinations of modes and metrics in a simple experimental setup, it has been demonstrated that for our deformable lens, in order to obtain the best sensorless aberration correction with the *Modes Correction Algorithm*, the aberration must be corrected using Lukosz or O2 modes (which leads to quite the same results) and the SD metric integrated over a range of low spatial frequencies (in our case from 0.03 to 0.1, being the total range from 0 to 1). This means that, even if the DLs we used have only 16 and 18 actuators, they can reproduce Lukosz mode as well as they can reproduce their *optimum modes*. This has been demonstrated experimentally for aberrations of amplitude $\leqslant 1$ waves rms ($\lambda = 633$ nm).

- In Chapter 5 our prototype of deformable lens with 18 piezoelectric actuators has been compared with

  1) a bimorph deformable mirror with 19 piezoelectric actuators: the DL is perfectly equivalent to – or even better than – this DM in the close loop corrections, and they can reproduce the same Zernike modes – the DL with equal or higher peak-to-valley values than the DM;

  2) a membrane deformable mirror with 32 electrodes: the DL can reproduce less Zernike modes than this DM, thus the closed loop corrections of random aberrations generated with the DM and corrected with the DL can't lead all the times to a flat wavefront (at least under the *Maréchal Limit*). Nevertheless, the residual aberration after the correction was mainly composed of those modes that the DL can't generate, so the two *wavefront correctors* are equivalent at least for low order Zernike modes ($Z_i, i \leqslant 15$).

- At the end of Chapter 5, after comparing the *wavefront correctors*, the DMs have been used to generate random aberrations

in the experimental setup, and closed loop and sensorless corrections of an extended sample have been performed: in all the cases the corrections led to an improvement of the image quality (measured by the *imaging sharpness metric*) and the sensorless corrections resulted all the times better than the closed loop ones. This result has been also obtained in all the aberration corrections performed in Chapter 4 and is principally due to *non common path errors*, which effects have been shown and discussed in Chapter 5.

- In Chapter 6, finally, the deformable lens has been implemented in a Confocal Microscope, and the *Modes Correction Algorithm* has been used with the optimized modalities explained and developed in the previous chapters. The implementation of the DL in the light path of the microscope is very simple, there are no beam splitters or beam expanders/reducers needed, nor any *wavefront sensor*. Wavefront sensorless aberration correction has been demonstrated in an epi-fluorescence setup and also in a confocal setup, using some 15μm fluorescent beads commonly used in the calibration of these systems.

7.2 FURTHER IMPROVEMENTS AND APPLICATIONS

In the previous paragraph the main results of this thesis have been summarized. Now we discuss some possible improvements that could be made in this work, and other applications that could be realized starting from it.

7.2.1 *Improvements in the Modes Correction Algorithm*

The sensorless aberration correction process using the *Modes Correction Algorithm* could be improved by removing crosstalk effects between tip-tilt modes and the modes we want to correct. This crosstalk causes the image of the sample to shift laterally (i.e. along the x- and y-axis) in the image plane, and this leads the algorithm to fail, especially if the shift is comparable with the portion of the image plane selected for sensorless correction. The same problem could emerge, when imaging thick samples, for the crosstalk between defocus and other modes, which could cause undesired shifts in the z-axis direction. Two possible solutions to this problem have been provided by the authors of the *Modes Correction Algorithm* in [14] and [34], so we could try to implement these methods in our sensorless correction code.

7.2.2 *Improvements in the Confocal Microscope*

Several improvements are needed also in our Confocal Microscope.

- First of all, a CCD camera more sensible than the one used in Chapter 6 (*Edmund Optics*, EO-3112C) is needed, in order to work also with weakly fluorescent samples. Furthermore, with a better camera we could also try to perform sensorless aberration corrections without removing the confocal disk during the

optimization, and then compare the images obtained with those taken with the confocal disk removed during the sensorless optimization.

- Different types of confocal disks should be tried in the microscope, in order to find the quantities S and D (see Figure 71) which optimize the disk performance to different objective numerical apertures and specimen thickness.

- Our prototype of deformable lens removes only the low order modes which constitute the aberration, in such a way that the residual aberration is mainly composed by Zernike modes $Z_i, i > 15$. Modes higher than Z_{15} could be removed using a deformable mirror with more than 18 actuators which can reproduce them: the DL could be used to remove low order aberrations while simultaneously the DM removes the high order ones, using a so-called *woofer-tweeter* control).

7.2.3 *Other applications*

Finally, we want to outline further applications that could be realized starting from the work described in this thesis.

Z-Stack. Optotune's fast electrically tunable DL described in Chapter 3 could be implemented with (or without) the 18-actuators DL in the microscope. The focal length of this lens can be changed electrically, so it enables to perform focusing and z-stack into the sample without moving it. Furthermore, it releases the 18-actuators DL from correcting defocus aberration. Unfortunately, trying it with different objectives and samples, we have realized that our Optotune's DL probably doesn't suit with our microscope, because the focal lengths it can reach are too short for a 20x objective or more. Thus, further investigations are needed, with this or other similar focus tunable DLs.

Endoscopy. The objective of the microscope can be substituted by a GRIN (graded index) optical probe, like the one described in [26]. The GRIN rod lenses guide light using internal variations in the refractive index rather than the curved refractive surfaces employed by conventional lenses, and their small size (0.5 mm diameter) enables *in-vivo* micro-endoscopy. The resolution values of these systems are generally not limited by diffraction, but rather by optical aberrations within the GRIN probe: the longer the probe is, the larger the aberrations which affect the light passing through it. These aberrations consist mainly in low order modes, thus our 18-actuators DL is a good candidate to remove them, using the same sensorless aberration correction procedures outlined in this thesis.

OCT. Our prototype of deformable lens has been already employed successfully in optical coherence tomography (OCT) for *in-vivo* mouse retinal imaging, with an approach similar to that described in [37]. In those experiments, sensorless corrections were performed using the *Modes Correction Algorithm* with the Irradiance Squared metric (IQ).

Thus, some improvements could be done using the *Modes Correction Algorithm* with the optimized modalities described in this thesis.

BIBLIOGRAPHY

[1] Babcock, H. W. (1953), "The possibility of compensating astronomical seeing", Publ. Astro. Soc. Pac., 65, 229-236

[2] Hardy, J. W. (1998), *Adaptive Optics for Astronomical Telescopes*, Oxford Series in Optical and Imaging Scienxes. Oxford University Press, New York

[3] Tyson, R. K. (2000), *Introduction to Adaptive Optics*, SPIE Press, Bellingham, Washington USA

[4] Tyson, R. K. (2005), *Adaptive Optics Engineering Handbook*, CRC Press, New York

[5] Tyson, R. K. & Frazier, B. W. (2004), *Field Guide to Adaptive Optics*, SPIE Press, Bellingham, Washington USA

[6] Vdovin, G. et al. (2013), *OKO Guide to Adaptive Optics*, OKO technologies, Rijswijk ZH, The Netherlands

[7] Kubby, J. A. (2013), *Adaptive Optics for Biological Imaging*, CRC Press, New York

[8] Schmidt, J. D. (2010), *Numerical simulation of optical wave propagation with examples in MATLAB*, SPIE Press, Bellingham, Washington USA

[9] Zernike, F. (1934), "Beugungstheorie des Schneidenverfahrens und Seiner Verbesserten Form, der Phasenkontrastmethode", Physica, 1, 689704

[10] Noll, R. J. (1976), "Zernike polynomials and atmospheric turbulence", J. Opt. Soc. Am. 66 (3), 207

[11] Lukosz, W. (1963), "Der Einfluss der Aberrationen auf die optische Ubertragungsfunktion bei kleinen Orts-Frequenzen", Opt. Acta 10, 1-19

[12] Braat, J. (1987), "Polynomial expansion of severely aberrated wave fronts" J. Opt. Soc. Am. A, 4 (4), 643-650

[13] Muller, R. A. & Buffington, A. (1974), "Real-time correction of atmospherically degraded telescope images through image sharpening", J. Opt. Soc. Am., 64 (9), 1200-1210

[14] Facomprez, A. et al. (2012), "Accuracy of correction in modal sensorless adaptive optics", Opt. Express, 20 (3), 2598-2612

[15] Débarre, D. et al. (2008), "Adaptive optics for structured illumination microscopy", Opt. Express, 16 (13), 9290-9305

[16] Wang, B. & Booth, M. J. (2009), "Optimum deformable mirror modes for sensorless adaptive optics", Opt. Communications, 282, 4467-4474

[17] Lagarias, J. C. et al. (1998), "Convergence properties of the Nelder-Mead Simplex Method in low dimensions", SIAM J. Optim. 9, 112-147

[18] Grewe, B. F. et al. (2011), "Fast two-layer two-photon imaging of neuronal cell populations using an electrically tunable lens", Biomed. Opt. Express, 2 (7), 2035-2046

[19] Fienup, J. R. & Miller, J.J. (2003), "Aberration correction by maximizing generalized sharpness metrics", J. Opt. Soc. Am., 20 (4), 609-620

[20] Antonello, J. et al. (2012), "Semidefinite programming for model-based sensorless adaptive optics", J. Opt. Soc. Am. A, 29 (11), 2428-2438

[21] Burgenot, C. J. T. (2013), "Light sheet adaptive optics microscope for 3D live imaging", Durham theses, Durham University. Available at Durham E-Theses Online: `http://etheses.dur.ac.uk/7713/`

[22] Murray, L. P. (2006), "Smart optics: Wavefront sensor-less adaptive optics - Image correction through sharpness maximisation", thesis submitted to the National University of Ireland, Galway. Available at: `http://optics.nuigalway.ie/people/larry/LarryThesis18052008.pdf`

[23] Izeddin, I. et al. (2012), "PSF shaping using adaptive optics for threedimensional single-molecule super-resolution imaging and tracking", Opt. Express, 20 (5), 4957-4967

[24] Bonora, S. (2011), "Distributed actuators deformable mirror for adaptive optics", Opt. Communications, 284, 2467-3473

[25] Vorontsov, M. A. et al. (1996), "Image quality criteria for an adaptive imaging system based on statistical analysis of the speckle field", J. Opt. Soc. Am. A, 13 (7), 1456-1466

[26] Bortoletto, F., Bonoli, C., Panizzolo, P., Ciubotaru, C. D. & Mammano, F. (2011), "Multiphoton Fluorescence Microscopy with GRIN Objective Aberration Correction by Low Order Adaptive Optics", PLoS ONE 6(7): e22321.doi:10.1371/journal.pone.0022321

[27] Booth, M. J. et al. (1998), "Aberration correction for confocal imaging in refractive-index-mismatched media", J. Microsc., 192 (2), 90-98

[28] Booth, M. J. et al. (2002),"Adaptive aberration correction in a confocal microscope", PNAS, 99 (9), 5788-5792

[29] Booth, M. J. (2006), "Wave front sensor-less adaptive optics: a model-based approach using sphere packings", Opt. Express, 14 (4), 1339-1352

[30] Débarre D., Booth M. J. & Wilson T. (2007), "Image based adaptive optics through optimisation of low spatial frequencies", Opt. Express, 15 (13), 8176-8190

[31] Booth, M.J. (2007), "Wavefront sensorless adaptive optics for large aberrations", Opt. Letters, 32 (1), 5-7

[32] Wang, B. & Booth, M. J. (2009), "Optimum deformable mirror modes for sensorless adaptive optics", Opt. Communications, 282, 4467-4474

[33] Simmonds, R.D. et al. (2011), "Effects of aberrations and specimen structure in conventional, confocal and two-photon fluorescence microscopy", J. Microsc., 245 (1), 63-71

[34] Thayil, A. & Booth, M.J. (2011), "Self calibration of sensorless adaptive optical microscopes", J. Eur. Opt. Soc, Rapid Publ. A, 11045

[35] Bonora, S. et al. (2011), "Optimization of low-order harmonic generation by exploitation of a resistive deformable mirror", Appl. Phys. B, 106 (4), 905-909

[36] Débarre, D. et al. (2009),"Image-based adaptive optics for two-photon microscopy", Opt. Letters, 34 (16), 2495-2497

[37] Jian, Y. et al. (2014), "Wavefront sensorless adaptive optics optical coherence tomography for *in vivo* retinal imaging in mice", Biomed. Opt. Express, 5 (2), 547-559

[38] Wright, A. J. et al. (2005), "Exploration of the optimisation algorithms used in the implementation of adaptive optics in confocal and multiphoton microscopy", Microsc. Res. Technol., 67, 3644

[39] Sherman, L. (2002), "Adaptive correction of depth-induced aberrations in multiphoton scanning microscopy using a deformable mirror", J. Microsc., 206, 6571

[40] Marsh, P. N. et al. (2003), "Practical implementation of adaptive optics in multiphoton microscopy", Opt. Express, 11, 11231130

[41] Albert, O. et al. (2000), "Smart microscope: an adaptive optics learning system for aberration correction in multiphoton confocal microscopy", Opt. Lett., 25, 5254

[42] Lubeigt, W. et al. (2002), "Active transverse mode control and optimization of an all-solid-state laser using an intracavity adaptive-optic mirror", Opt. Express, 10, 550-555

[43] Theofanidou, E. et al. (2004), "Spherical aberration correction for optical tweezers" Opt. Commun., 236, 145150

[44] Gonte, A. C. F. & Dandliker, R. (2002), "Optimization of single-mode fiber coupling efficiency with an adaptive membrane mirror", Opt. Eng., 41, 10731076

[45] Perreault, J. A. et al. (2002), "Adaptive optic correction using microelectromechanical deformable mirrors", Opt. Eng., 41 (3), 561-566

[46] Vdovin, G. & Sarro, P. M. (1995), "Flexible mirror micromachined in silicon", Appl. Opt., 34 (16), 2968-2972

[47] Bifano, T. G. et al. (1999), "Microelectromechanical Deformable Mirrors", IEEE J. Sel. Top. Quant. Electron., 5 (1), 83-89

[48] Dalimier, E. & Dainty, C. (2005), "Comparative analysis of deformable mirrors for ocular adaptive optics", Opt. Express, 13 (11), 4275-4285

[49] Loktev, M. et al. (2001), "Comparison study of the performance of piston, thin plate and membrane mirrors for correction of turbulence-induced phase distorsions, Opt. Communications, 192, 91-99

[50] Devaney, N. et al. (2008), "Correction of ocular and atmospheric wavefronts: a comparison of the performance of various deformable mirrors", Appl. Opt., 47 (35), 6550-6562

[51] Vdovin, G. & Loktev, M. (2001), "Deformable mirror with thermal actuators", Opt. Letters, 27 (9), 677-679

[52] Long, C. S. et al. (2008), "Development of a Piezoelectric Adaptive Mirror for Laser Beam Control", In ACTUATOR 2008, *11th International Conference on New Actuators, Bremen, Germany, 9 11 June 2008*, paper no. 17, 584-587

[53] Dainty, J. C. et al. (1998) , "Low-order adaptive deformable mirror", Appl. Opt., 37 (21), 4663-4668

[54] Born, M. & Wolf, E. (1983), *Principle of Optics*, 6th ed., Pergamon Press

[55] Loomis, J. S. (1992), "Evaluation of optical aberrations in point images", Appl. Opt., 31 (13), 2211-2222

[56] Sulai, Y. N. & Dubra, A. (2014), "Non-common path aberration correction in an adaptive optics scanning ophthalmoscope", Biomed. Opt. Express, 5 (9), 3059-3073

[57] Myers, R. M. et al. (2002), "The NAOMI Adaptive Optics System for the 4.2m William Herschel Telescope", available at `http://www.ing.iac.es/Astronomy/instruments/naomi/naomispie2002.pdf`

[58] `http://www.optotune.com/images/products/Optotune%20EL-10-30.pdf`

[59] `http://www.thorlabs.de/newgrouppage9.cfm?objectgroup_id=2970`